Pulsed magnetic resonance on single defect centers in diamond

Von der Fakultät Mathematik und Physik der Universität Stuttgart
zur Erlangung der Würde eines
Doktors der Naturwissenschaften (Dr. rer. nat.)
genehmigte Abhandlung

Vorgelegt von:

Iulian Popa
aus Brăila (Rumänien)

Hauptberichter:	Prof. Dr. Jörg Wrachtrup
Mitberichter:	Prof. Dr. Gert Denninger
Tag der mündlichen Prüfung:	22 Februar 2006

3. Physikalisches Institut der Universität Stuttgart

2006

Contents

Abstract

In the present work, the spin properties of single Nitrogen-Vacancy (NV) defect centers in diamond are investigated, in perspective to their application to quantum computing. One of the actual approaches to quantum computing is based on spins, and, therefore, their behavior and properties related to manipulation and readout are very important. Using conventional NMR, an ensemble of spins can be used as a qubit implementation. However, the method has limitations in regards to the number of qubits that can be achieved. Conventional magnetic resonance methods cannot be applied to a single spin because of their low sensitivity. Instead, an alternative method for detection of magnetic resonance, Optical Detection of Magnetic Resonance (ODMR) was proved to be suitable for detection of single spins.

The method of choice for studying single NV defects combines single molecule detection techniques with magnetic resonance. The NV center in diamond is paramagnetic (S = 1). The energy level scheme consists of a triplet ground state and a triplet excited state as well as a singlet metastable state. The center can be optically detected due to the fluorescent transition between the excited and ground triplets. In zero magnetic field, the ground state splits into three components, (X and Y, $m_S = \pm 1$) and Z ($m_S = 0$), separated by 2.88 GHz. The ground state can be used as a spin qubit implementation. In order to determine the properties associated with the NV

triplet ground state, continuous wave (cw) and pulsed ODMR methods have been applied. The coherent evolution in time of the electron spin in a microwave field is probed by observing transient nutations. The decoherence time of the single electron spin is measured by the Hahn echo method. ESEEM experiments prove the hyperfine structure of the neighboring nuclei, i.e., for this case, ^{14}N nucleus. Simulations of the energy level scheme and spin dynamics of a single electron spin confirm the experimental findings. Furthermore, the influence of the optical readout on the evolution of the system is studied, and the possibility of observing quantum Zeno effect in a single electron spin is addressed.

The hyperfine coupling of the single electron spin to a single neighboring ^{13}C gives the possibility of scaling up the number of spin qubits. The ^{13}C nucleus has a spin 1/2. The nuclear spin states can be readout via the electron spin states. The hyperfine energy level scheme was probed experimentally by cw ODMR. Calculations confirmed the hyperfine structure. A Hahn echo sequence, adapted to nuclear spins was employed for determining the decoherence time for the single nuclear spin. The state of the setup at that time did not allow the determination of the hyperfine tensor. All calculation assume an isotropic value for the hyperfine constant.

The issue of dipolar coupling between two NV centers is addressed, in the context of its eventual use towards increasing the degree of qubit scalability. The magnetic dipolar coupling depends upon the distance between the centers, according to the known rule of dipolar coupling interaction energy. The resulting energy level scheme of two coupled NVs was probed via cw ODMR. Two theoretical models for the coupling between centers result in a good agreement with experimental data.

Chapter 1

Introduction

1.1 Single molecule detection and manipulation

Over the last decades, important progress has been made in developing methods for detection and manipulation of single quantum systems. Due to the removal of normal ensemble averaging over a sample characteristics, as it is the case in bulk measurements, the single molecule regime is expected to unravel new physical and chemical behaviour. Previous to single molecule detection, experiments on single ions or electrons confined in electromagnetic traps revealed interesting aspects of quantum mechanics, e.g., quantum jumps, photon antibunching [IBW87]. However, the experimental environment used for these cases, i.e., vacuum and electromagnetic fields for the traps, cannot be applied for single molecules in solids. Similarly, Scanning Tunneling Microscopy (STM) [BR87] and Atomic Force Microscopy (AFM) [BQG86] made significant advances in increasing the spatial resolution to the limit of detection of single systems. Even though these techniques are well-known

and commercially available, they can only be used for surface investigations. Optical detection of single molecules can overcome these problems: it has a less restrictive experimental environment and allows for detection of single quantum objects embedded into a crystal lattice.

The first optical detection of single molecules was achieved by Moerner and Kador in 1989 [MK89]. The detection method was based on the absorption of the laser light in a small volume sample of pentacene-doped p-terphenyl crystal, at liquid He temperature. Spectral selection was applied in order to identify single molecules by tuning the laser frequency within the inhomogeneously broadened line of the electronic transition. In the following year, single molecule detection based on fluorescence was performed by the Orrit group [OB90]. An advantage of using fluorescence emission rather than absorption is the improved signal-to-noise ratio, at both room and low temperatures. In both cases, the detection of single molecules delivers expected results for as long as the concentration of the impurities in the host is low enough so that they can be isolated in the spectrum and the detection efficiency sufficiently high in order to overcome the dark count rate in the detector.

Fluorescence detection of single molecules has been applied to several fields: molecular and solid state physics, quantum optics, biophysics [Orr02]. One of the spectacular outcomes was performing magnetic resonance on single spins [ea93a, ea93b]. It is well known that Nuclear Magnetic Resonance (NMR) and Electron Spin Resonance (ESR) are important tools in investigations at molecular or submolecular levels. In both conventional NMR and ESR, a large number of spins is required to provide a detectable signal, e.g., $10^{16} - 10^{18}$ spins for NMR and $10^{10} - 10^{12}$ spins for ESR. Both methods use inductive readout methods. For decreasing the number of observable spins,

the external meagnetic field has to be increased. However, in the limit of a single spins, the amplitude of the external magnetic field would be too high for any technologically aproachable method.

1.2 Single molecule detection and quantum computing

The new physics in the single molecule domain becomes highly important in the context of the recent developments in nanophysics and nanotechnologies. Among these, the emerging field of quantum information holds much promises related to the improvement of the computing capabilities and communications security. Besides the practical use of quantum information, questions of fundamental physics can be addressed. Topics like experimental realization of entangled states, theory of quantum measurement, spin transport in solids, can be studied within the large framework of quantum information.

The quantum analog of a bit in classical computing is a quantum bit (qubits), i.e., a quantum system with two available states corresponding to the classical 0 and 1. The advantage over the classical counterpart resides in the fact that a quantum system state is a linear superposition of the two eigenfunctions attached to the system. Thus, the power of a quantum processor is given by the dimension of the Hilbert space associated with the physical implementations of qubits. The logic gates within the new computer architecture would be a combination of unitary operations. The field got more momentum with the advent of Shor's algorithms for factorizing large numbers [Sho94] and Grover's algorithm for searching large databases [Gro95].

The requirements for hardware implementations of qubits have been summarized in the so-called DiVincenzo list [DiV95]:

1. Initialization of the qubits in a simple state - insures that the quantum operations have a known initial state of quantum registers.

2. Long decoherence time - the time interval within the quantum gates can be applied; succesful completion of operations is given by the 'quality factor', i.e., the ratio between the decoherence time and the time needed to apply a gate. Long decoherence times are needed for error correction codes.

3. Universal set of quantum operations - the operations consist of combinations of logic gates, which in turn are sequences of unitary transformations, related to the Hamiltonian describing the qubits

4. Qubit specific measurement capability - the ability to read out the state of the qubits after applying the set of unitary transformations

5. Qubit scalability - to perform calculations, more than one qubit will be needed. Scaling up the number of qubits would result in a higher dimension of the associated Hilbert space, and implicitly, a higher computing power

Up to date, there are several proposals for implementations of qubits: ion traps [CZ95], superconducting qubits [NPT99, MOL$^+$99], quantum dots [LL01], NMR spin-based qubits [GC97, GC98], linear optics qubits [EKM01]. The later is, up to date, the most succesful in terms of the number of qubits implemented, even though the nature of the entanglement achieved is still under debate. For the spin-based approach, a spin 1/2 provides a natural basis for implementation of qubits, due to its two spin projections, 1/2 and -1/2, to which states 0 and 1 can be associated, respectively. Subsequently,

the state of the system is given by the linear combination of the two spin eigenstates

$$\begin{aligned} \psi &= a\,|0\rangle + b\,|1\rangle \\ |a|^2 &+ |b|^2 = 1. \end{aligned} \tag{1.1}$$

Logic operations consist of sequences of rf pulses in the case of nuclear spins. Using the spin states of nuclei, 7 qubits have been implemented using NMR [VSB+01]. However, the liquid state NMR approach is limited in the number of qubits. The qubit implementation is not a single quantum system, but an ensemble of nuclei. The measurement on a spin ensemble would prevent the initialization of a pure state, and a measurement on it would not result in a wave function collapse, as it would be the case of a single system. The measurement result would be an average value over an ensemble. Due to the fact that the thermal energy is much larger than the energy difference between two spin sublevels, the scalability of the system is limited [WC97].

A solution for a spin-based quantum computing approach would be given by single spins. The ensemble averaging would be eliminated in this way, and pure states would be available. Thus, a good spin implementation would require a single spin which can be easily manipulated and readout. The Nitrogen-Vacancy (NV) center in diamond presents all these features. The NV center is an impurity center in diamond that can be read out optically in the single molecule domain. It is photostable upon optical excitation. Due to its paramagnetic nature, it is suitable for ESR. Thus the logic gates would consist of ESR pulses. However, for constructing a qubit out of an NV center, its properties and dynamic behaviour have to be fully understood.

1.3 Nitrogen-Vacancy (NV) defect center in diamond

A large array of impurities is present in diamond, influencing many of its optical properties. The most abundant impurity in diamond is nitrogen. The nitrogen impurities in diamond can be found in forms of single atomic nitrogen or nitrogen clusters. Based on the type and quantity of the impurities, diamonds can be classified into four distinct categories [Dav84]:

- Type Ia - high amount of nitrogen, up to 0.3%; the most common type of natural diamond
- Type Ib - comprises mostly of synthetic diamonds. It may contain up to 500 ppm in atomic nitrogen
- Type IIa - very rare, with extremely low nitrogen content
- Type IIb - p-type semiconductor

Beside nitrogen atoms, boron, silicon and hydrogen are the most abundant impurities in diamond. However, their presence is detectable only when the density of nitrogen is very low. Synthetic diamonds can be produced by either High Pressure High Temperature (HPHT) Synthesis or by Chemical Vapor Deposition (CVD). In the HPHT synthesis procedure, graphite and a metallic catalyst are placed in a hydraulic press under high temperatures and pressures. Over periods of two hours, the graphite converts into diamond. The CVD procedure is used for fabricating thin films of diamond.

The NV defect center consists of a single nitrogen atom next to an adjacent vacancy in the lattice. In addition to that, an electron from the diamond

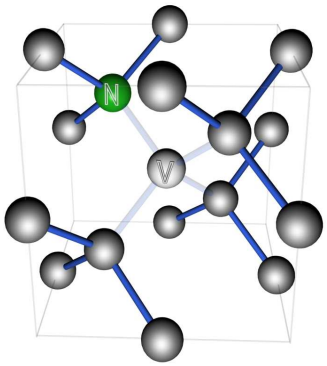

Figure 1.1: Schematic representation of NV defect in diamond

lattice is captured by the center. Subsequently, the electron spin of the defect is going to be given by the coupling between the captured electron and the unpaired electron from the nitrogen atom, resulting in a spin S = 1. Thus, the NV center is a paramagnetic impurity. Fig. 1.1 shows a geometrical view of the NV defect center in diamond. It can occur naturally in diamond with nitrogen impurities, having a particularly high concentration in type Ia diamond. In the case of type Ib diamonds, NV defects can be obtained by irradiation and subsequent annealing at temperatures above 800 K. By electron irradiation, vacancies are produced in the diamond lattice. The annealing treatment induces the migration of the vacancies through the diamond lattice, and implicitely to nitrogen atoms, enhancing the chances of producing a higher concentration of NV defects. The NV defect can be also produced in type IIa diamonds, by N^+ implantation. Based on neutron irradiation experiments, the NV defect has been identified as a negatively charged center [Mit96].

The NV center presents a fluorescence excitation spectrum with a zero-phonon line at 637 nm (1.945 eV) [DH76, Dav94]. In ^{13}C diamonds the ZPL is shifted by 2.1 meV [CDKW88]. The oscillator strength of the zero-phonon line is comparable to the one corresponding to GR1 center $f_{NV}/f_{GR1} = 1.15$ [DLC^{+}92] [Zai01]. The phonon wings in the excitation spectrum is given mostly by electron-phonon coupling with 65 meV vibration modes, with a strength $\lambda = 3.65$. The fluorescence lifetime of the NV center is 11.6 ns at low temperature (70 K) or 13.3 ns, at ambient conditions [Zai01, CTJ83].

The fluorescence transition occurs between the triplet excited state and triplet ground state. The center has C_{3v} symmetry. The ground state is split into three sublevels, X,Y (corresponding to $m_S = 1$, $m_S = -1$, respectively) and Z ($m_S = 0$), separated by 2.88 GHz [vO90, RMK87]. The excited state is also split into three levels, mainly due to the spin-orbit interactions and lattice strain [Mar99]. Details on the internal structure of the NV center will be given in Chapter 4.

1.4 Outline of the dissertation

The present work focuses on the properties of single NV centers in diamond, from the point of view of its eventual use in quantum computing. Chapter 2 outlines the experimental methods used to detect and manipulate single NVs. Technical details about the optical readout setup, magnetic resonance hardware and data acquisition software are presented. Chapter 3 present the theoretical approach to ODMR on single NV centers. This introduces the methods for calculating the energy level scheme of NV, the hyperfine interactions with neighboring nuclei, and the spin dynamics of the NV centers. The internal photophysics related to the NV and the optical readout are presented in Chapter 4. Chapter 5 is concerned with magnetic resonance on single NV defects: cw and pulsed ODMR, analysis of the results, influence of the optical readout on the decoherence time of a single spin. The hyperfine coupling to ^{13}C is studied in Chapter 6. Chapter 7 presents some preliminary results and theoretical intepretations of ODMR on two coupled NVs.

Chapter 2

Experimental

2.1 Experimental setup

2.1.1 Optical setup

Single molecule detection is achieved by fluorescence excitation spectroscopy using a confocal microscope. A typical experimental setup for single molecule fluorescence spectroscopy is presented in Fig. 2.1. The laser light is directed through fiber optics and reflected by the dichroic beamsplitter into the high NA microscope objective, resulting in a diffraction-limitted focal spot on the sample glass plane. The diameter of the laser spot, defined by the Sparrow criterion is $d_S = 0.51\lambda/NA$ [BW99], where λ is the excitation laser wavelength. Thus, the necessity of a high NA objective is obvious, since the collected background light will scale with the area of the spot.

The fluorescence light from the sample is collected via the same pathway as the incident light. The excitation light is filtered out by an emission filter, so that only the fluorescence light will proceed further through the detection chain. The pinhole blocks the fluorescence originating from outside the focal

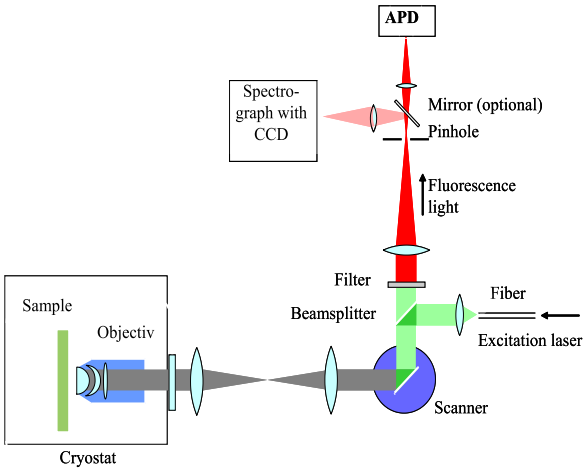

Figure 2.1: Schematic representation of the optical setup

plane of interest. The diameter of the pinhole determines the depth of the confocal image, thus giving the axial resolution. For a low diameter of the pinhole, a high axial resolution is achieved, increasing the probability of detecting a single defect. However, the transmission through the pinhole decreases with the diameter of the pinhole, so in order to have a good signal-to-noise ratio (SNR), a trade-off between transmission and axial resolution has to be made. Typically, the diameter of the pinhole is in the order of tens of μm, which gives an axial resolution smaller than 200 nm, with a transmission higher than 90 %. Emerging from the pinhole the fluorescence photons are detected by an avalanche photodiode (APD). Optionally, the fluorescence light can be redirected to a spectrograph, in order to record the optical spectrum. The APD is an advanced semiconductor detector, with a single-photon detection resolution. Upon detection of a photon, the APD generates a transistor-transistor logic (TTL) signal, which can be further on processes

digitally. For the spectrograph, a charge-coupled device (CCD) detector is used. The CCD camera consists of a 2-dimensional array of coupled photon counting devices, cooled down at liquid nitrogen temperature. The quantum efficiency of the CCD camera is around 80 % (Ropper Scientific, former Princeton Instruments).

2.1.2 Magnetic resonance hardware

The magnetic resonance hardware had to be adapted in order to meet the requirements of the present experimental approach. First, opposite to the conventional ESR/NMR there is no magnetic resonance hardware involved in the readout scheme. This is completely optical. Thus the magnetic resonance is used for pulse generation in order to manipulate the spins states of the NV center. For ESR experiments, microwaves are transmitted to the sample through a microresonator (provided by D. Suter, University Dortmund). The small size of the diameter of the resonator allows to achieve Rabi frequencies of up to 50 MHz in the center of the loop. As a microwave generator a Hewlett-Packard Digital Signal Generator was used. The microwaves are amplified by a TWT amplifier.

For the radiofrequency, an rf Wavetek generator was employed (.2-1100 MHz). A solid state amplifier (P = 20 W) was used for rf. Both generators are functioning in a triggered mode, i.e., the pulse sequence is generated based on a trigger signal comming from a digital signal generator. HP 8175A Digital Signal Generator and Tektronix AWG 2041 Arbitrary Waveform Generator have been used for this purpose. In the advanced pulse sequences, the signal generators are used for triggering the laser as well.

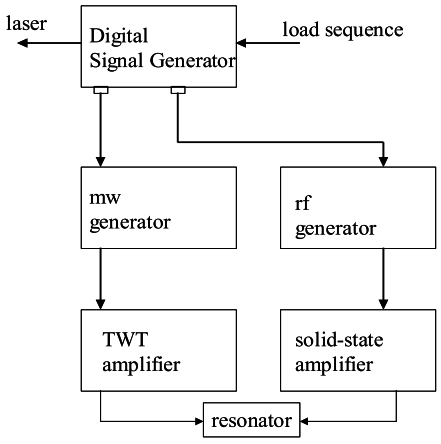

Figure 2.2: Magnetic resonance hardware scheme. The mw/rf generators are triggered by a digital signal generator interfaced with a computer, and their outputs are amplified through TWT and solid-state amplifiers, respectively. The digital signal generator is used also for laser triggering.

2.2 Data acquisition software

The main data acquisition (DAQ) system is designed to meet the criteria of pulsed and cw ODMR experiments. The DAQ software was implemented on a Windows 2000 [1] operating system using a Borland C++ Builder IDE platform [2]. The software design choice combined with the given hardware result a in maximum efficiency within a low range of overall costs for the entire system. All codes feature a multithreaded, event-driven design, cross-compatible with most versions of Windows operating system. Most of DAQ software involve a real-time data sampling with direct visual access to the acquired data.

[1] Windows is a trademark of Microsoft Corp.

[2] Borland C++ Builder is a trademark of Inprise Corp.

The DAQ software consists mainly of two main synchronized threads: pulse preparation/control and detection. The hardware for the former was presented in the previous section. For the detection chain a multifunction National Instruments NI-6601 counter/timer card was used. The TTL signal from the APD is read by the counter card. The control of operation is performed via the PCI bus. The maximum timebase for the counter is 20 MHz, which provides a good time binning for most of the experimental trials in cw ODMR. The control of DAQ was in circular buffered mode with external triggering. This insures that no data are lost during the process of acquisition. For the simple cw ODMR spectra, the pulse sequence design code is implemented within the main acquisition program. The pulses are transferred via GPIB to the microwave generator and the acqusition is triggered upon completion of pulse sequence loading into the generator. For more complicated pulse sequences, the Tektronix generator was used. A general wave designer code was written for this purpose. The program has a graphical interface and allows to configure any pulse sequence on the eight output channels of the generator. The drawback is that for the specific hardware, an external support, i.e., a floppy disk has to be used in order to transfer the encoded pulse sequences to the device. The GPIB bus is too slow for this purpose, and no other transfer protocol was available.

Chapter 3

Theoretical model for description of ODMR experiments

This chapter introduces the mathematical methods used in the analysis of the NV center structure and spin dynamics. The first section shows the spin Hamiltonian adopted for describing the energy structure. The main parts of the Hamiltonian are shortly discussed. The energies and eigenstates have been determined using the direct product expansion procedure, which is described in one of the subsections. The second part deals with the spin dynamics of the NV center. The Liouville equations are set in order to determine the time evolution of the density matrix elements. The pulsed experiments result in fluorescence output that can be described by the differences in level populations.

3.1 The spin Hamiltonian of the NV center

The general spin Hamiltonian of a system consisting of an electron spin coupled to N nuclear spins is given by [SJ01]

$$\begin{aligned} H &= H_{ZF} + H_{eZeeman} + H_{hf} + H_Q + H_{nZeeman} \\ &= \hat{S}\bar{D}\hat{S} + \beta_e \vec{B}_0 \bar{g} \hat{S} + \sum_{k=1}^{N} \hat{S}\bar{A}_k\hat{I}_k + \sum_{I_k>1} \hat{I}_k\bar{P}_k\hat{I}_k - \beta_N \sum_{k=1}^{N} g_{n,k}\vec{B}_0\hat{I}_k \end{aligned} \tag{3.1}$$

where g_e, g_n are the g factors for the electron and nuclei respectively, β_e, the Bohr magneton, β_n, the nuclear magneton, $\bar{A}$, the hyperfine coupling tensor, $\bar{P}$ quadrupole coupling tensor, and $\vec{B}_0$, the external magnetic field applied to the system. The Hamiltonian in Eq. 7.26 contains only electron and nuclear spin coordinates, hence the name. The terms in the Hamiltonian describe the following interactions: H_{ZF}, the zero field splitting, $H_{eZeeman}$, the electron Zeeman interaction, H_{hf}, the hyperfine interactions, H_Q, the quadrupolar interactions for nuclei with $I > 1/2$, and $H_{nZeeman}$, the nuclear Zeeman interactions. The spin state functions associated with H form the reduced (spin-based only) Hilbert space of the electron-nuclear system, with the dimension

$$d = \prod_{k=1}^{n} (2S_k + 1) \prod_{k=1}^{m} (2I_k + 1) \tag{3.2}$$

where n is the number of electrons and m the number of nuclei in the system. In the case of a single NV center, the electron spin $S = 1$, coming from the unpaired electron in nitrogen coupled to an electron captured from the diamond lattice, is treated as a single spin. Thus, according to Eq.3.2, the dimension of the Hilbert space for the case of a single center is 3, while for the case of a single NV coupled to one ^{13}C nucleus, the Hilbert space will be spanned by six eigenfunctions.

The energy levels structure can be obtained by diagonalizing the Hamiltonian corresponding to a specified system. For this purpose the Hamiltonian must first be setup within the appropriate coordinates for the system and then eigenvalues and eigenfunctions can be extracted nummerically, using any linear algebra package (Matlab [3], NAG [4]).

3.1.1 Zero field splitting

The zero-field splitting (zfs) is present in a system with a spin $S \geq 1$, due to the dipole-dipole coupling between the electron spins. The zero-field Hamiltonian is

$$H_{ZF} = \hat{S}\bar{D}\hat{S} \tag{3.3}$$

where $\bar{D}$ is zero-field interaction tensor. In its pricipal axes coordinate systems, the zfs Hamiltonian can be written as [WBW94]

$$\begin{aligned} H_{ZF} &= D_x S_x^2 + D_y S_y^2 + D_z S_z^2 \\ &= D\left[S_z^2 - \tfrac{1}{3}S\left(S+1\right)\right] + E\left(S_x^2 - S_y^2\right) \end{aligned} \tag{3.4}$$

where $D = 3D_z/2$ and E $= (D_x - D_y)/2$. Due to the axial symmetry of the NV center, $E = 0$.

The spin eigenfunctions of the zero-field Hamiltonian in terms of spin projection quantum numbers are

$$\begin{aligned} \psi_0 &= |0\rangle \\ \\ \psi_{\pm 1} &= \tfrac{1}{\sqrt{2}}\left[|1\rangle \mp |-1\rangle\right] \end{aligned} \tag{3.5}$$

[3] Matlab is a registered trademark of The Mathworks Inc.

[4] Nummerical Algorithm Group - NAG is a not-for-profit company limited by guarantee

In order to diagonalize nummerically the zfs Hamiltonian, the spin matrices for $S = 1$ are needed:

$$S_x = \begin{bmatrix} 0 & 0.707 & 0 \\ 0.707 & 0 & 0.707 \\ 0 & 0.707 & 0 \end{bmatrix}$$

$$S_y = \begin{bmatrix} 0 & -0.707i & 0 \\ 0.707i & 0 & -0.707i \\ 0 & 0.707i & 0 \end{bmatrix} \tag{3.6}$$

$$S_z = \begin{bmatrix} 1 & 0 & 0 \\ 0 & 0 & 0 \\ 0 & 0 & -1 \end{bmatrix}$$

3.1.2 Hyperfine and quadrupole interactions

The hyperfine interaction between the electron and nuclear spins is described by the Hamiltonian

$$H_{hf} = \hat{S}\bar{A}\hat{I} \tag{3.7}$$

where $\bar{A}$ is the hyperfine coupling tensor. Within the hyperfine interaction, two terms are present: the isotropic Fermi contact term and the electron-nuclear dipole-dipole coupling. The isotropic hyperfine interaction represents the electron spin density at the nucleus, while the anisotropic part is given by the dipolar interaction between the electron and the nucleus. In its principal axis frame, the hyperfine coupling tensor for a center with axial

symmetry is reduced to

$$\bar{A} = \begin{bmatrix} A_{\perp} & & \\ & A_{\perp} & \\ & & A_{||} \end{bmatrix} \tag{3.8}$$

The electron spin of the NV center is hyperfine coupled to the ^{14}N nucleus (I = 1), and to a ^{13}C nucleus (I = 1/2) in an adjacent lattice site. The hyperfine coupling to ^{14}N is characterized by a hyperfine tensor values $A_{||} =$ 2.4 MHz and $A_{\perp} = 2.1$ MHz.

For the interaction of the electron spin with nuclei having spin $I \geq 1$, the quadrupole interaction has to be taken into account. The general form of the quadrupolar interaction Hamiltonian is

$$H_Q = \hat{I}\bar{Q}\hat{I} \tag{3.9}$$

where $\bar{Q}$ is the quadrupole tensor. In the case of NV centers, the quadrupole interaction have to be considered due to the coupling to the ^{14}N nucleus. In the principal axes system the quadrupole interaction tensor is

$$\bar{Q} = \begin{bmatrix} Q_{xx} & & \\ & Q_{yy} & \\ & & Q_{zz} \end{bmatrix} \tag{3.10}$$

and the Hamiltonian takes the expression

$$H_Q = \frac{1}{2}P\left[3I_z^2 - I\left(I+1\right) + \eta\left(I_x^2 - I_y^2\right)\right] \tag{3.11}$$

where P is proportional to the quadrupole coupling constant and η is the asymmetry parameter. For ^{14}N, $P = -5.04$ MHz and $\eta = 0$.

3.1.3 Zeeman interactions

The Zeeman interaction will develop for both electron and nuclear spins upon application of an external magnetic field. The terms $\beta_e \vec{B}_0 \bar{g} \hat{S}$ and $\beta_N \sum_{k=1}^{N} g_{n,k} \vec{B}_0 \hat{I}_k$ in Eq. 7.26 describe the electron and nuclear Zeeman interactions, respectively. However, the Zeeman effect on the nuclear spins is much smaller than that corresponding to the electron, due to the ratio between the Bohr magneton and nuclear magneton ($\beta_e/\beta_N \approx 1000$). The Lande' factor g, for atoms, is given by the

$$g = 1 + \frac{J(J+1) + S(S+1) - L(L+1)}{2J(J+1)} \tag{3.12}$$

The spin orbit interaction contributes to the anisotropy of the g-factor, resulting in a slight deviation from the free electron value. Similarly to the anisotropic hyperfine interaction, the g-tensor has to be used for this case:

$$\bar{g} = \begin{bmatrix} g_{\perp} & & \\ & g_{\perp} & \\ & & g_{||} \end{bmatrix} \tag{3.13}$$

The g-tensor in this form was considered in the principal axes system, and collinear with the hyperfine tensor for nitrogen.

For the case of the NV center in the diamond, the deviations from the free electron g-factor are rather negligible. Under the influence of the crystal field of the surrounding lattice, the orbital angular momentum is quenched and only the spin S is left interacting with the crystal field. Thus, the orbital angular momentum is quenched, and therefore its contribution to the anisotropy will be zero. Very small contributions to the g-factor may come through overlaping effects between the wavefunction of the electron in the NV and the wavefunctions of the electronic shells in the neighboring atoms

in the lattice. Thus, in a good approximation the g-factor for the electron in the NV can be considered isotropic and its value is equal to that of a free electron.

3.1.4 Direct product expansion method

When dealing with a system formed of two or more coupled spins, the total spin of the system is given by vectorial sum over all spins:

$$\vec{S} = \sum_i \vec{S}_i, \tag{3.14}$$

or for the most common case of two spins

$$\vec{S} = \vec{S}_1 + \vec{S}_2. \tag{3.15}$$

The possible representations for the eigenfunctions of the system are $|Sm\rangle$, where S is the total spin and m is its projection, and $|m_{S_1} m_{S_2}\rangle$, where m_{S_1} and m_{S_2} are the spin projections of each of the two spins. Here, the later representation will be used for all the calculations. Therefore in this representation the total spin of the system may be written as

$$\vec{S}' = \vec{S}_1 \otimes \vec{I}_1 + \vec{I}_2 \otimes \vec{S}_2 \tag{3.16}$$

where I_1 and I_2 are the unity matrices in the S_1 and S_2 subspaces.

This is termed as direct product method [JF72, Fre88] and in order to exemplify it, the coupling between a electron spin 1 and a nuclear spin 1/2 is considered. The simplified Hamiltonian for this case reads

$$H = B_0 \left(g_e \beta S_z - g_N \beta_N I_z\right) + \bar{A}\vec{S}\vec{I} \tag{3.17}$$

where the external magnetic field is along the z axis, and the g-factor and hyperfine coupling are isotropic. The resulting reduced Hilbert space is spanned by six eigenfunctions, in the representation mentioned above. The hyperfine interaction can be expressed as a direct product between the two spin matrices. In the Zeeman term, a 3x3 identity matrix will be inserted in the case of a electron spin, and a 2x2 matrix will be inserted in the case of the nuclear spin

$$H = B_0 \left[g_e \frac{\beta}{2} \begin{pmatrix} 1 & 0 \\ 0 & 1 \end{pmatrix} \otimes \begin{pmatrix} 1 & 0 & 0 \\ 0 & 1 & 0 \\ 0 & 0 & -1 \end{pmatrix} - g_N \beta_N \begin{pmatrix} 1 & 0 & 0 \\ 0 & 1 & 0 \\ 0 & 0 & 1 \end{pmatrix} \otimes \begin{pmatrix} 1 & 0 \\ 0 & -1 \end{pmatrix} \right] +$$

$$+ \frac{A}{2} \begin{pmatrix} 1 & 0 & 0 \\ 0 & 0 & 0 \\ 0 & 0 & -1 \end{pmatrix} \otimes \begin{pmatrix} 1 & 0 \\ 0 & -1 \end{pmatrix} \tag{3.18}$$

Afterwards, the Hamiltonian can be brought by simple algebra to a form from where it can be numerically diagonalized. The problem will be one of finding the eigenvectors and eigenvalues of a matrix. The resulting energy levels for the system are given by linear combinations of $|m_S m_I\rangle$, with $m_S = 1, 0, -1$ and $m_I = 1/2, -1/2$, in this order.

3.1.5 Transition probabilities

Upon application of an oscillating field (microwaves in the case of ESR, radiofrequency in the case of NMR),$\vec{B}_1 \cos(\omega t)$, transitions between spin levels can be induced. The transition probability between an initial state E_i and a final state E_f is given by the expression [AB70]

$$P_{if} = \frac{2\pi}{\hbar^2} \left|\langle f \left| V\left(t\right) \right| i \rangle\right|^2 \delta\left(\omega_{if} - \omega\right) \tag{3.19}$$

where $V(t)$ is the Hamiltonian corresponding to the oscillating field

$$V\left(t\right) = -\beta \vec{M} \cdot \vec{B}_1 \cos(\omega t) \tag{3.20}$$

and for the case of an electron spin coupled to a nuclear spin

$$V\left(t\right) = \beta_e g_e \vec{S} \cdot \vec{B}_1 \cos(\omega t) - \beta_N g_N \vec{I} \cdot \vec{B}_1 \cos(\omega t) \tag{3.21}$$

The transition probability between two states will be then given by the matrix elements of the magnetic moment operator $\vec{M}$. In a Cartesian reference frame, the magnetic moment can be written in terms of spin matrices of the electron and nucleus:

$$\vec{M} = g_e \left(S_x \vec{i} + S_y \vec{j} + S_z \vec{k}\right) - g_N \left(I_x \vec{i} + I_y \vec{j} + I_z \vec{k}\right) \tag{3.22}$$

Thus the transition probabilities will be given by the elements of the matrix $\langle f \left| M \right| i \rangle$, [JF72] transformed into the representation which diagonalizes the main Hamiltonian of the system:

$$M^* = V^{-1} M V \tag{3.23}$$

Here, V is the set of eigenfunctions obtained upon diagonalizing the static Hamiltonian of the electron-nuclear system.

3.2 Spin dynamics of the NV center

The information about the state of a system in an ODMR experiment is given by its optical response. For the case of NV centers, the information regarding the spin behaviour is encoded in the fluorescence photons corresponding to the transition ^{3}E-^{3}A. In ODMR the measurement is always connected to differences in the populations between the two levels from where the fluorescence originates. As a result, the amplitude of the fluorescence signal will be given by level populations. The problem of calculating the response of the system reduces to determining the time evolution of the density matrix elements.

Based on the ergodic hypothesis, the Liouville equation for an ensemble can be applied to a single spin to describe its kinematics

$$i\hbar\frac{d\rho}{dt} = [H, \rho] \tag{3.24}$$

where ρ is the density matrix and H is the Hamiltonian of the NV coupled to the applied optical and microwaves fields. Expanding the commutator on the right side, the equation can be rewritten as

$$i\hbar\dot{\rho} = H\rho - \rho H. \tag{3.25}$$

The following will show a generic algorithm for calculations involving a 5-level system for the NV center, with axial symmetry at room temperature. The model can describe the time evolution of the density matrix elements, thus providing a tool to simulate pulsed magnetic resonance experiments. Fig. 3.1 shows the NV level scheme addressed by the calculations. The excitation laser couples the $m_s = 0$ sublevel of the ground state to one of the vibrational levels of the excited state ^3E. The non-radiative relaxation

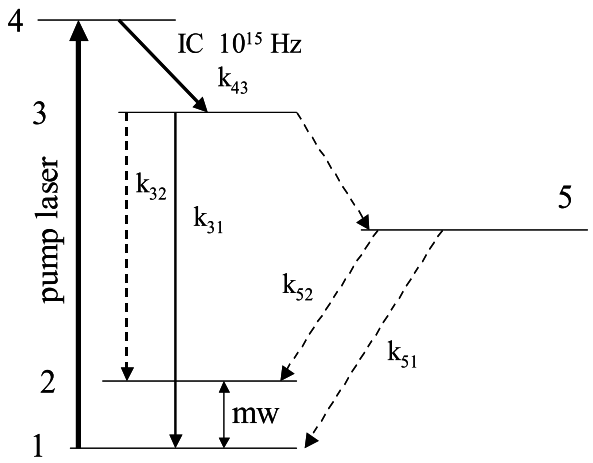

Figure 3.1: 5-level scheme of NV center used for spin dynamics calculations

of the vibrational levels is of the order of 10^{15} Hz. The microwaves are applied between the sublevels of the ground state, separated by the zero-field splitting.

The density and the Hamiltonian can be written in a 5x5 matrix form as using the level indexing presented in Fig. 3.1

$$\rho = \begin{bmatrix} \rho_{11} & \rho_{12} & \rho_{13} & \rho_{14} & \rho_{15} \\ \rho_{21} & \rho_{22} & \rho_{23} & \rho_{24} & \rho_{25} \\ \rho_{31} & \rho_{32} & \rho_{33} & \rho_{34} & \rho_{35} \\ \rho_{41} & \rho_{42} & \rho_{43} & \rho_{44} & \rho_{45} \\ \rho_{51} & \rho_{52} & \rho_{53} & \rho_{54} & \rho_{55} \end{bmatrix} \tag{3.26}$$

and

$$H = \begin{bmatrix} H_{11} & H_{12} & H_{13} & H_{14} & H_{15} \\ H_{21} & H_{22} & H_{23} & H_{24} & H_{25} \\ H_{31} & H_{32} & H_{33} & H_{34} & H_{35} \\ H_{41} & H_{42} & H_{43} & H_{44} & H_{45} \\ H_{51} & H_{52} & H_{53} & H_{54} & H_{55} \end{bmatrix} \tag{3.27}$$

The Hamiltonian of the NV center subjected to optical and microwaves fields can be expressed as

$$\begin{aligned} H = \sum_i \hbar\omega_i \left|i\right\rangle \left\langle i\right| - \hbar\Omega \cos\left(\omega_M t\right) \left(\left|1\right\rangle \left\langle 2\right| + \left|2\right\rangle \left\langle 1\right|\right) - \\ \hbar\Lambda \cos\left(\omega_L t\right) \left(\left|1\right\rangle \left\langle 4\right| + \left|4\right\rangle \left\langle 1\right|\right) \end{aligned} \tag{3.28}$$

with

- ω_i - energy of the state i
- ω_L - laser frequency in Hz
- ω_M - mw frequency in Hz
- Ω - laser Rabi frequency,$\Omega = \frac{\left(\vec{E}\cdot\vec{d}_{ij}\right)}{\hbar}$
- $\vec{d}_{ij}$ - transition dipole moment between states i and j
- $\vec{E}$ - amplitude of the laser electric field corresponding to frequency ω_L

- Λ - mw Rabi frequency, $\Lambda = \gamma \vec{B}_y$

- γ - gyromagnetic ratio of the electron

- $\vec{B}_{1y}$ - the y-component of the mw magnetic field

The matrix elements of the Hamiltonian $\langle i \,|H|\, j \rangle$ result in the matrix form

$$H = \hbar \begin{bmatrix} \omega_{11} & -\Lambda & 0 & -\Omega & 0 \\ -\Lambda & \omega_{22} & 0 & 0 & 0 \\ 0 & 0 & \omega_{33} & 0 & 0 \\ -\Omega & 0 & 0 & \omega_{44} & 0 \\ 0 & 0 & 0 & 0 & \omega_{55} \end{bmatrix} \tag{3.29}$$

The Rabi frequency of the optical and microwaves fields are time dependent, oscillating with their field frequencies and can be written as

$$\begin{aligned} \Lambda &= \Lambda_0 \cos(\omega_M t) \\ \Omega &= \Omega_0 \cos(\omega_L t) \end{aligned} \tag{3.30}$$

The Liouville equations become

$$
\begin{aligned}
\dot{\rho}_{11} &= i\Lambda_0 \cos(\omega_M t)(\rho_{21} - \rho_{12}) + i\Omega_0 \cos(\omega_L t)(\rho_{41} - \rho_{14}) \\
\dot{\rho}_{22} &= -i\Lambda_0 \cos(\omega_M t)(\rho_{21} - \rho_{12}) \\
\dot{\rho}_{33} &= 0 \\
\dot{\rho}_{44} &= -i\Omega_0 \cos(\omega_L t)(\rho_{41} - \rho_{14}) \\
\dot{\rho}_{55} &= 0 \\
\dot{\rho}_{12} &= -i\Lambda_0 \cos(\omega_M t)(\rho_{11} - \rho_{22}) + i\rho_{12}\omega_{21} + i\Omega_0 \cos(\omega_L t)\rho_{42} \\
\dot{\rho}_{21} &= i\Lambda_0 \cos(\omega_M t)(\rho_{11} - \rho_{22}) - i\rho_{12}\omega_{21} - i\Omega_0 \cos(\omega_L t)\rho_{24} \\
\dot{\rho}_{14} &= -i\Omega_0 \cos(\omega_L t)(\rho_{11} - \rho_{44}) + i\rho_{14}\omega_{41} + i\Lambda_0 \cos(\omega_M t)\rho_{24} \\
\dot{\rho}_{41} &= i\Omega_0 \cos(\omega_L t)(\rho_{11} - \rho_{44}) - i\rho_{14}\omega_{41} - i\Lambda_0 \cos(\omega_M t)\rho_{42}
\end{aligned}
\tag{3.31}
$$

with

$$
\begin{aligned}
\omega_{21} &= \omega_{22} - \omega_{11} \\
\omega_{41} &= \omega_{44} - \omega_{11}
\end{aligned}
\tag{3.32}
$$

The equations above are corresponding to a system isolated from the environment. The relaxation and dephasing processes can be included phenomenologically; thus, the relaxation processes can be introduced in the expressions of diagonal elements (populations) and the dephasing processes can be attached to the non-diagonal elements (coherences). The relaxation rates

used are indicated in Fig. 3.1 and the general notation is k_{ij}, where i and j are the levels in between where the relaxation occurs. The dephasing is represented by Γ_{ij}, where $\Gamma_{ij} = \frac{k_{ij}}{2} + \Gamma^*_{ij}$, with Γ^*_{ij} being given by the homogeneous linewidth of the transition, $\Gamma^*_{ij} = \pi\nu_{hom}$. With the relaxation and dephasing processes included, the Liouville equations for diagonal elements of the density matrix read

$$\begin{aligned}
\dot{\rho}_{11} &= i\Lambda_0 \cos(\omega_M t)(\rho_{21} - \rho_{12}) + i\Omega_0 \cos(\omega_L t))(\rho_{41} - \rho_{14}) + k_{21}\rho_{22} + k_{31}\rho_{33} + k_{51}\rho_{55} \\
\dot{\rho}_{22} &= -i\Lambda_0 \cos(\omega_M t)(\rho_{21} - \rho_{12}) - k_{21}\rho_{22} + k_{32}\rho_{33} + k_{52}\rho_{55} \\
\dot{\rho}_{33} &= k_{43}\rho_{44} - (k_{35} + k_{31} + k_{32})\rho_{33} \\
\dot{\rho}_{44} &= -i\Omega_0 \cos(\omega_L t))(\rho_{31} - \rho_{13}) - k_{43}\rho_{44} \\
\dot{\rho}_{55} &= k_{35}\rho_{33} - (k_{51} + k_{52})\rho_{55}
\end{aligned} \tag{3.33}$$

and for the coherences

$$\begin{aligned}
\dot{\rho}_{12} &= -i\Lambda_0 \cos(\omega_M t)(\rho_{11} - \rho_{22}) + i\rho_{12}\omega_{21} + i\Omega_0 \cos(\omega_L t)\rho_{42} - \Gamma_{12}\rho_{12} \\
\dot{\rho}_{21} &= i\Lambda_0 \cos(\omega_M t)(\rho_{11} - \rho_{22}) - i\rho_{12}\omega_{21} - i\Omega_0 \cos(\omega_L t)\rho_{24} - \Gamma_{12}\rho_{12} \\
\dot{\rho}_{14} &= -i\Omega_0 \cos(\omega_L t)(\rho_{11} - \rho_{44}) + i\rho_{14}\omega_{41} + i\Lambda_0 \cos(\omega_M t)\rho_{24} - \Gamma_{14}\rho_{14} \\
\dot{\rho}_{41} &= i\Omega_0 \cos(\omega_L t)(\rho_{11} - \rho_{44}) - i\rho_{14}\omega_{41} - i\Lambda_0 \cos(\omega_M t)\rho_{42} - \Gamma_{14}\rho_{41}
\end{aligned} \tag{3.34}$$

The obtained set of linear differential equations can be solved nummerically, but this involves a rather slow processing algorithm, even when a fast linear algebra package is used. Thus, it is recommended to eliminate the time-dependent terms related to the explicit form of the Rabi frequencies. The time dependency can be eliminated by transforming the equations in the rotating reference frame of variable fields; for this case the rotating frame of the optical and microwave fields are going to be used. As a result, the coherences of the system will be converted and the diagonal elements will have the same value (level populations remain constant within a reference frame change)

$$\begin{aligned} \rho_{ii} &= \sigma_{ii} \\ \rho_{14} &= \sigma_{14} e^{i\omega_L t} \\ \rho_{12} &= \sigma_{12} e^{i\omega_M t}. \end{aligned} \tag{3.35}$$

Here, σ represents populations or coherences in the rotating frame. The relations above have been written considering the laser coupling levels 1 and 4, and the microwaves between levels 1 and 2. Note that in this way level 1 is coupled to both microwave and laser fields. Equation terms proportional to $e^{2i\omega_L t}$ or $e^{2i\omega_M t}$ are out of resonance and are subsequently neglected (rotary wave approximation). Therefore, the equations can be rewritten in the new reference frame as

$$\dot{\sigma}_{11} = -\frac{i\Lambda_0}{2}(\sigma_{12} - \sigma_{21}) - \frac{i\Omega_0}{2}(\sigma_{14} - \sigma_{41}) + k_{21}\sigma_{22} + k_{31}\sigma_{33} + k_{51}\sigma_{55}$$

$$\dot{\sigma}_{22} = \frac{i\Lambda_0}{2}(\sigma_{12} - \sigma_{21}) - k_{21}\sigma_{22} + k_{32}\sigma_{33} + k_{52}\sigma_{55}$$

$$\dot{\sigma}_{33} = k_{43}\sigma_{44} - (k_{35} + k_{32} + k_{31})\sigma_{33}$$

$$\dot{\sigma}_{44} = \frac{i\Omega_0}{2}(\sigma_{14} - \sigma_{41}) - k_{43}\sigma_{44}$$

$$\dot{\sigma}_{55} = k_{35}\sigma_{33} - (k_{52} + k_{51})\sigma_{55} \tag{3.36}$$

$$\dot{\sigma}_{12} = i\sigma_{12}(\omega_{21} - \omega_M) - \frac{i\Lambda_0}{2}(\sigma_{11} - \sigma_{22}) - \Gamma_{12}\sigma_{12}$$

$$\dot{\sigma}_{21} = -i\sigma_{21}(\omega_{21} - \omega_M) + \frac{i\Lambda_0}{2}(\sigma_{11} - \sigma_{22}) - \Gamma_{12}\sigma_{21}$$

$$\dot{\sigma}_{14} = i\sigma_{14}(\omega_{41} - \omega_L) - \frac{i\Omega_0}{2}(\sigma_{11} - \sigma_{44}) - \Gamma_{14}\sigma_{14}$$

$$\dot{\sigma}_{14} = -i\sigma_{41}(\omega_{41} - \omega_L) + \frac{i\Omega_0}{2}(\sigma_{11} - \sigma_{44}) - \Gamma_{14}\sigma_{41}$$

The Liouville equations resulted in a system of homogeneous differential equations, of the form $\dot{X} = RX$, with

$$X = \begin{bmatrix} \sigma_{11} \\ \sigma_{22} \\ \sigma_{33} \\ \sigma_{44} \\ \sigma_{55} \\ \sigma_{12} \\ \sigma_{21} \\ \sigma_{14} \\ \sigma_{41} \end{bmatrix} \tag{3.37}$$

and the relaxation matrix

$$R = \begin{bmatrix} 0 & k_{21} & k_{31} & 0 & k_{51} & \frac{-i\Lambda_0}{2} & \frac{i\Lambda_0}{2} & \frac{-i\Omega_0}{2} & \frac{i\Omega_0}{2} \\ 0 & -k_{21} & k_{32} & 0 & k_{52} & \frac{i\Lambda_0}{2} & \frac{-i\Lambda_0}{2} & 0 & 0 \\ 0 & 0 & -K_1 & k_{43} & 0 & 0 & 0 & 0 & 0 \\ 0 & 0 & 0 & -k_{43} & 0 & \frac{i\Omega_0}{2} & -\frac{i\Omega_0}{2} & 0 & 0 \\ 0 & 0 & k_{35} & 0 & -K_2 & 0 & 0 & 0 & 0 \\ -\frac{i\Lambda_0}{2} & \frac{i\Lambda_0}{2} & 0 & 0 & 0 & \Delta_1 & 0 & 0 & 0 \\ \frac{i\Lambda_0}{2} & -\frac{i\Lambda_0}{2} & 0 & 0 & 0 & 0 & -\Delta_1 & 0 & 0 \\ \frac{-i\Omega_0}{2} & 0 & 0 & \frac{i\Omega_0}{2} & 0 & 0 & 0 & \Delta_2 & 0 \\ \frac{i\Omega_0}{2} & 0 & 0 & \frac{-i\Omega_0}{2} & 0 & 0 & 0 & 0 & \Delta_2 \end{bmatrix}. \tag{3.38}$$

Chapter 4

Optical readout of the NV defect center

The NV defect center is one of the impurities in diamond that can be read out optically on a single defect basis. For further investigations, it is essential to have a good understanding of the photophysics associated with the defect. Here, the second order autocorrelation function is introduced as a method of proof for identifying single defects. The outcomes of optical spectroscopy performed on the NV at low and room temperatures are discussed, in the context of determining the photophysical parameters governing the fluorescence spectrum behaviour.

4.1 Single center readout. Fluorescence intensity autocorrelation function

The time distribution of photons emitted by a single NV center allows to determine some of its internal photophysical processes. In order to characterize the time distribution of the emitted photons, it is useful to introduce

the second order fluorescence autocorrelation function, defined as [Lou83]

$$g^{(2)}(\tau) = \frac{\langle I(t)I(t+\tau)\rangle}{\langle I(t)\rangle^2} \tag{4.1}$$

where $I(t)$ is the fluorescence intensity measured at the moment t. The numerator in the expresion of the autocorrelation function can be calculated by integrating over the total time of measurement T:

$$\langle I(t)I(t+\tau)\rangle = \lim_{T\to\infty} \frac{1}{T} \int_0^T I(t)I(t+\tau)dt \tag{4.2}$$

The autocorrelation function can be obtained from measurements on photon pairs, separated by a given time delay τ [BWO+94]. For further analysis, it is useful to normalize the autocorrelation function, according to [BBG+01]. $g^{(2)}(\tau)$ can be re-written as

$$g_c^{(2)} = \frac{[C_N(\tau) - (1-\rho^2)]}{\rho^2} \tag{4.3}$$

with

$$\rho = \frac{S}{S+B} \tag{4.4}$$

Here S represents the signal and is given by the sum of the fluorescence intensities in the two detectors, and B is the background. $C_N(\tau)$ is the background correction to the recorded coincidences, and is given by

$$C_N(\tau) = \frac{c(\tau)}{N_1 N_2 w T} \tag{4.5}$$

where $c(\tau)$ is the raw coincidence rate in the measurement time T with the time resolution w and N_1 and N_2 are the number of counts in the two detectors. The probability of having a pair of photons in the time interval $[t; t+\tau]$ is given by the probability that the center will be in its excited state at both times t and $t+\tau$. Thus, a null value for $g^{(2)}(\tau)$ for $\tau = 0$ would indicate the detection of a single photon, originating from a single center.

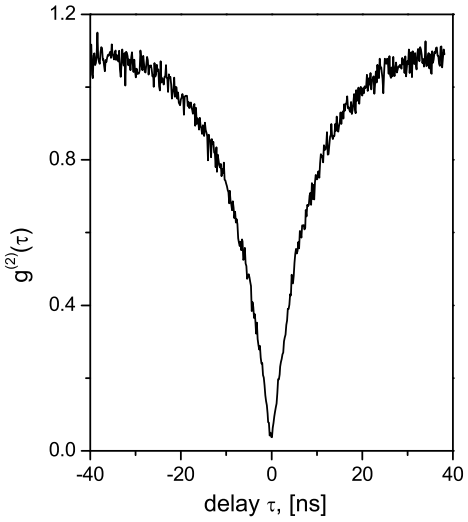

Figure 4.1: Measured fluorescence intensity autocorrelation function

Fig. 4.1 shows the result of a fluorescence intensity autocorrelation function. For zero-delay value, the autocorrelation function goes to zero, exhibiting an antibunching effect, associated with the non-classical nature of the fluorescence emitted by a single NV. The antibunching effect can be explained intuitively in relation with projection-type measurements on single quantum systems. Immediately after emitting a photon, the system will be in its ground state. Thus, upon measurement on the state of the system, represented here by the detection of the fluorescence photon, the system is projected into the ground state, from where it cannot emit another photon, unless pumped back to its excited state. For a time delay $\tau = 0$, the system cannot emit and therefore, $g^{(2)}(\tau)$ will exhibit a subunitary value. For a single center, $g^{(2)}(\tau = 0) = 0$. The contrast of the autocorrelation function will decrease as the number of centers increases.

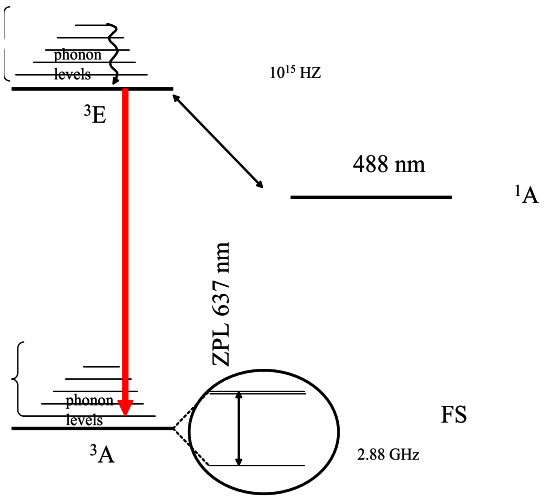

Figure 4.2: Schematic representation of NV energy levels at room temperature. The fine structure corresponding to the ground state ^3A is also shown.

4.2 Optical readout of NVs

Single NV defects have been first detected optically at room temperature using a scanning confocal microscope [GDT+97]. The system showed no bleaching under laser illumination, even for excitation intensities close to saturation. Fig. 4.2 shows the energy levels scheme of the NV at room temperature. The vibronic levels result from lattice vibrations as well as from intermolecular vibrations. The spectrum for a single NV center at room temperature is shown in Fig. 4.3.

The zero-phonon line associated with the $^3A - ^3E$ is at 637 nm (1.945 eV) and shows an inhomogeneous broadening of 30 cm^{-1}. The high amplitude of the inhomogeneous broadening can be attributed to a large strain variation in the excited ^{3}E state.

Due to the strong inhomogeneous broadening of the zero-phonon line

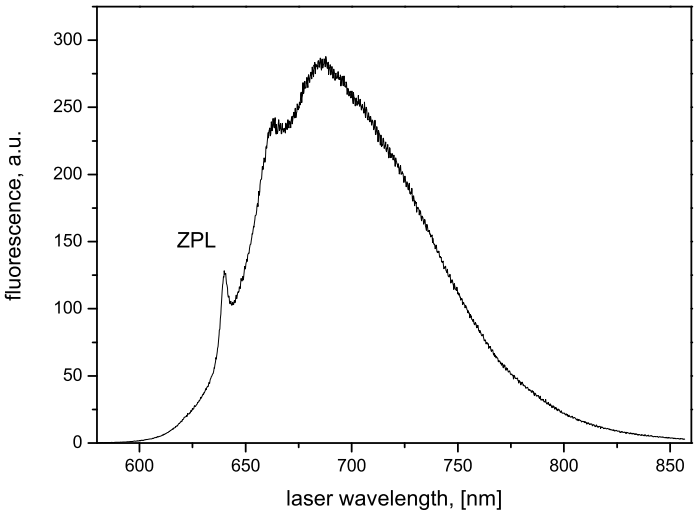

Figure 4.3: Fluorescence spectrum of a single NV center. The zero-phonon line (ZPL) is indicated at 637 nm.

recorded at room temperatures, the fine structure of the ^3A ground state cannot be optically accessed. One possible way to overcome this problem is to perform experiments at low temperatures. Initial experiments at low temperature performed on large diamond crystals [DFT$^+$99] showed certain unexpected limitations in reading out optically the fine structure of NV center ground state. Thus, for temperatures below 90 K, it was observed that the fluorescence intensity decreases significantly mainly due to the metastable singlet state ^1A. Also, the low fluorescence output may be due to the high refractive index of diamond ($n = 2.4$). The use of diamond nanocrystals instead of bulk diamonds can overcome both of these problems [BBG$^+$01].

The sample material consisted of nanocrystals with sizes smaller than 250 nm, lower than the laser wavelength. This insures that the surface reflections do not have a significant effect on the extracted fluorescence .

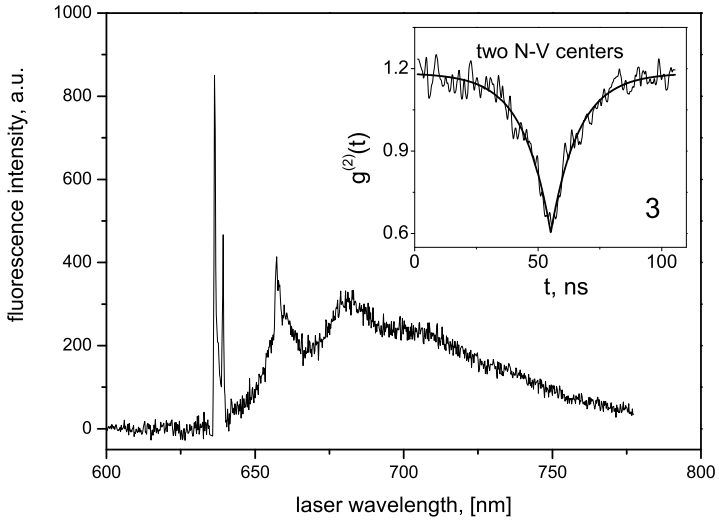

Figure 4.4: Low-temperature (T = 2 K) spectrum of NV centers in nanocrystals. The excitation was at 514 nm. The zero-phonon lines around 637 nm correspond to two NV centers. The inset to the figure shows the autocorrelation function; the contrast (0.5) proves the presence of two NV centers.

Fig. 4.4 shows the fluorescence emission spectrum of single NVs at $T = 2$ K. Two zero-phonon lines are visible around 637 nm, corresponding to two NV centers. The number of NVs was determined by performing fluorescence antibunching experiments. The outcomes of these experiments is shown in the inset of the figure: the fluorescence intensity autocorrelation function has a contrast of 0.5, indicating the presence of two NV centers. Compared with the fluorescence spectra from bulk diamonds, the lines in Fig. 4.4 are a few times wider, most probably due to the enhanced strain in the nanocrystals lattice. Similarly, the phonon sidebands observed in the spectrum of nanocrystals are different from the sidebands recorded in bulk diamonds. This can be related to the quantization of acoustic phonon states

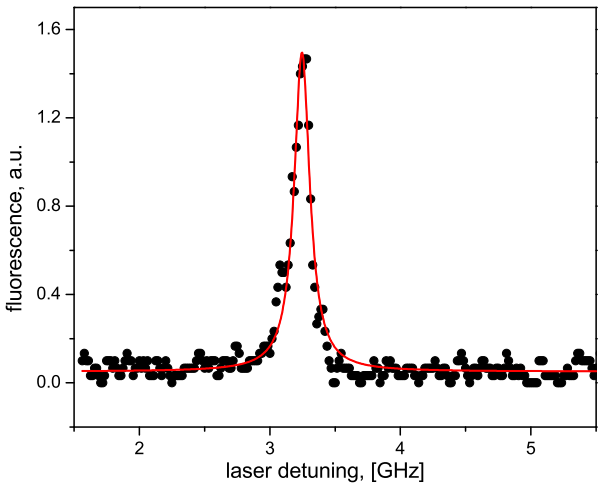

Figure 4.5: Absorption line at 637 nm.

in nanocrystals. Previous studies on CdSe/ZnS nanocrystals at low temperatures [PW01] showed a non-linear temperature dependence of the homogeneous linewidth.

In order to perform optical spectroscopy on single NV centers, the electronic transitions have been scanned using a single mode ring dye laser, with a resolution of 1 MHz. Fig 4.5 shows the fluorescence excitation spectrum of a single NV center at $T = 2K$. The laser had been swept across the 637 nm transition. The absorption line at 637 nm in Fig. 4.5 has a width of 150 MHz and presents a Lorentzian lineshape. Due to the triplet structure of the ground and excited states, several allowed transitions are expected in the spectrum, instead of a single line. A detailed account on the possible reasons is given in the next section.

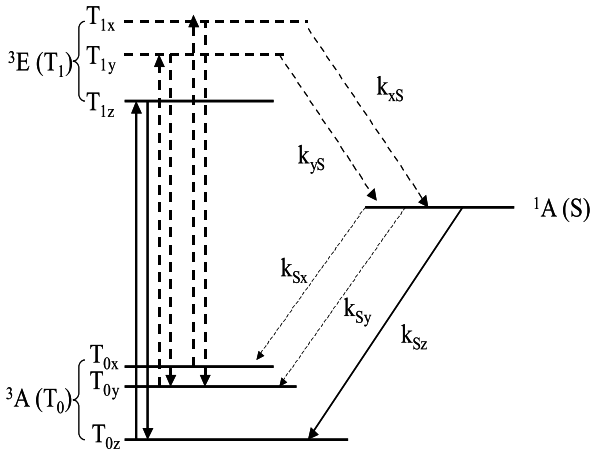

Figure 4.6: Energy levels scheme for the NV center at low temperatures.

4.3 Theoretical model for NV structure

The assumed basic levels scheme is presented in Fig. 4.6. Each triplet consists of three sublevels, T_{0x}, T_{0y}, and T_{0z}, corresponding to $m_S = 1, -1, 0$ for the ground state and T_{1x}, T_{1y}, and T_{1z} for the excited state. The metastable state, S is a singlet. The optical transition occurs between the triplets T_0 and T_1. The center is considered under continuous illumination by a narrow-band laser in near-resonance with the 637 nm transition ($T_0 - T_1$). The linewidth of the laser is thus smaller than the zero-field splitting in the ground state of the NV center. Furthermore, it is assumed that the NV center maintains its $C_{3\nu}$ symmetry. This has important consequences for the number of allowed transitions within the two spin triplets. Due to different electron distribution for the electron pair in the two triplet states, the principal axes of the tensor describing the ground state will be different from those describing the excited state and thus, it is expected that transitions will occur between each of the two triplet sublevels. In the presence of the symmetry, the direc-

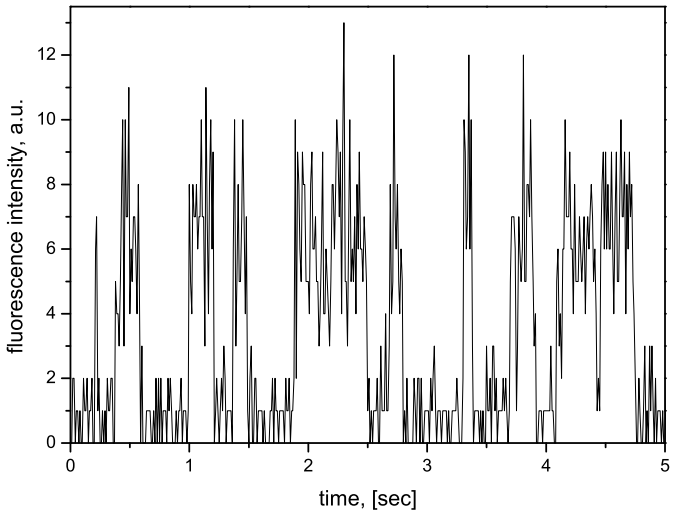

Figure 4.7: Time trace of single N-V center fluorescence intensity

tion of the principal axes is invariant. Hole burning experiments performed on 2,2-Dinaphthylcarbene in n-Heptane and n-Hexane at 1.7 K [KAO$^+$00] have shown that under enforced $C_{2\nu}$ symmetry of the molecule, the number of possible transitions between sublevels of the triplet states decreases. Consequently, for the NV case, there will be three possible transitions between triplet sublevels with similar quantum numbers. The transitions are expected to appear at different positions in the spectrum, due to different zero-field splittings in the ground and excited states. This should result in three spectral lines, upon laser sweeping over the $T_0 - T_1$ transition. However, the experimental spectrum shows a single excitation line. The absence of satellite lines given by the other possible transitions can be explained by intersystem crossing.

Furthermore, the fluorescence output of a single center kept under continuous illumination of the excitation laser shows a so-called telegraph behav-

iour. The time trace of the fluorescence intensity of a single NV center in Fig. 4.7 shows dark intervals (low fluorescence intensity) alternating with higher fluorescence intensity intervals (bright). This can also be explained by the photo-processes involving the presence of the metastable state. Thus, a high fluorescence intensity is obtained for as long as the system maintains one of the triplet-triplet channels, i.e., transitions between corresponding sublevels within the two triplets, $T_{1i} - T_{0i}$.The transition rates for this case are in the order of $10^6 s^{-1}$. However, from the excited triplet state T_1, the system can be subjected to a transition to the singlet state. This will drive the center out of resonance with the excitation laser, resulting in a low fluorescence intensity. Three possible transition paths are possible from the metastable singlet state to the triplet ground state; these will correspond to each of the sublevels of the triplet. Each of these transitions are much slower than the radiative transition $T_{1i} - T_{0i}$. Since the excitation of the center is selective, i.e., only one sublevel of each triplet is addressed by the excitation laser, only one of the three transitions from the metastable state to the ground state will restore the high fluorescence output of the center. By following this channel, the spin projection is preserved, e.g., if the driving laser couples the $m_S = 0$ sublevels of each triplet, a transition from the singlet state to $m_S = 1$ of the ground state will not conserve the spin projection. The remaining two transitions, resulting in a change in spin projections will drive the system out of resonance with the laser (the linewidth of the laser is smaller than the zero-field splitting in the ground state). For this case, the fluorescence will be restored through a relaxation process between the sublevels of the ground triplet state. T_1 of the system at low temperatures is in the order seconds, due to low thermal energy. A concurent process will be a spin-spin interaction between the ground states of two close-by centers; the cross-relaxation

process will result in a redistribution of the populations of the triplet state sublevels. However, the cross-relaxation mechanism involves a rather high density of centers, just opposite to the requirements of low temperature single center detection.

In order to describe the fluorescence spectrum, a theoretical model has been proposed by Nizovtsev et al. [NKJ+03]. The average fluorescence intensity of the center, obtained from the optical Bloch equations is given by

$$\langle I_{fl} \rangle = \frac{AB}{3\left(A + B + k_S\right) + B\left(1 + \frac{k_S}{R}\frac{k_D + R}{k_T}\right)} \tag{4.6}$$

with

$$\begin{aligned} k_D &= k_x + k_y \\ k_T &= k_D + k_z \end{aligned} \tag{4.7}$$

where A is the rate of spontaneous transition $T_{1z} - T_{0z}$, B is the rate of absorption, R is the spin-lattice relaxation rate, k_S is the population rate of the singlet level from the triplet level, and k_x, k_z, and k_y are the single depopulation rates to the ground levels. The expression for the average fluorescence intensity is valid for time intervals larger than the optical dephasing; as a consequence, the optical Bloch equations will result only in diagonal elements, optical coherences being eliminated. For low temperatures and low density of defects, the spin-lattice relaxation is much lower than the depopulation rates of the singlet level to the ground sublevels. With these conditions, the average fluorescence intensity will be given by

$$\langle I_{fl} \rangle \approx \frac{RA}{k_S} \tag{4.8}$$

The typical values for the parameters used in the equation above are $R =$ 1 Hz, $A = 10^8$ Hz. The detection efficiency for the low-temperature setup is approximately 1%. Thus, a good agreement of the calculated fluorescence intensity with the experimental data was obtained for an intersystem crossing rate $k_S = 1$ kHz. Faster shelving rates have been observed in correlation measurements on single NV centers [KMZW00]. The intersystem crossing rate is essential for the possibility of detection of resonance lines for single defects. spectral hole burning experiments showed a transition rate of $k_S =$ 12.4 kHz, which can be attributed to shelving from the Z sublevel [Ran94]. Therefore, the resonant lines expected in the spectrum, corresponding to transitions other than T_{1z} - T_{0z} are not observable due to the low fluorescence intensity.

Chapter 5

ODMR on single NV centers

As described in the introduction, a physical system has to meet certain criteria in order to function as a qubit. In the present chapter, it will be proved that single NV centers in diamond meet all of the criteria. In the previous chapter, it was shown the a single NV center can be optically readout via fluorescence detection. This provides also the role of initialization of the qubit, as upon emitting a fluorescence photon, the system will be found in its lowest state. The aspects related to the rest of DiVincenzo's criteria will be approached here. First, the NV defect ground level energy structure is investigated and spin levels identified via cw ODMR. The experimental findings are confirmed by calculations. The hyperfine coupling to ^{14}N nucleus is studied. The NV defect is shown to provide two levels separated by 2.9 GHz in its ground state. The spin behaviour of single spins is investigated in order to obtain the decoherence-related properties of the system. Transient nutations on single defects are performed in order to prove the coherent behaviour upon application of microwave pulses. For the case of single NV spins, the unitary transformations are given by microwave pulses. The decoherence time is measured via spin echo. Furthermore, the influence of the

optical readout scheme on the decoherence time will be described according to the model presented in Chapter 3, and the possibility of observing the quantum Zeno effect is discussed.

5.1 cw ODMR of single NV centers

5.1.1 cw ODMR spectra

Continuous wave ODMR experiments have been performed by sweeping the microwaves along a frequency range centered on the separation between levels Z and X or Y. As mentioned in the previous chapter, the system is polarized mainly in level Z. The optical readout will couple this level with the corresponding sublevel in the excited state ^{3}E. For this purpose, a green laser was utilized.

Fig. 5.1(a) illustrates a simplified model for the cw ODMR on the NV center. Thus, the recorded fluorescence maintains a constant level for as long as the population distributions within the triplet ground state are not modified. This case corresponds to a microwave frequency off-resonance with the allowed ESR transition(s) within the triplet state. Upon turning the microwaves in resonance with these transitions, the populations will change; the system will undergo a change of populations from level Z to levels X or Y. As a result, this will induce a lower fluorescence outcome, as the optical readout is mainly coupled to Z level. The process is termed negative ODMR effect. Fig. 5.1(b) shows a simulation of the line at 2900 MHz, for the case of a symmetric NV defect. For non-symmetric centers, two lines will occur in the cw ODMR spectrum, corresponding to the two allowed transitions.

Fig. 5.2 shows an experimental cw ODMR spectrum obtained on a single NV center. The center lacks the characteristic three-fold symmetry and

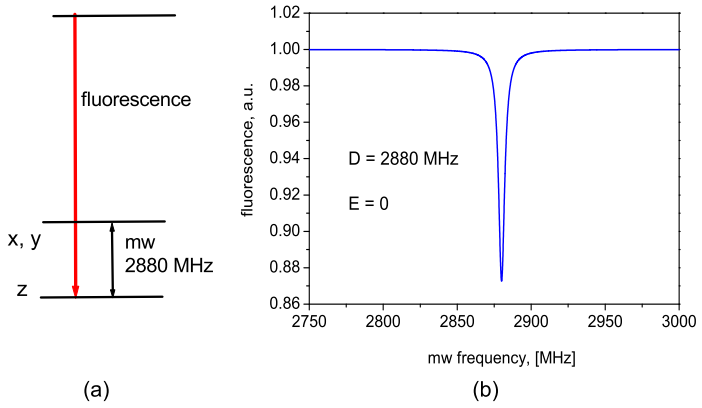

Figure 5.1: (a) cw ODMR simplified model for NV centers. The highest fluorescence yield corresponds to the radiative transition to level Z of the ground triplet; the microwaves change the population distributions between the sublevels of the ground state (b) simulation of a cw spectrum of a axially symmetric NV center.

therefore exhibits two allowed transitions. The separation between the two lines is, for this case, 10 MHz (E = 10 MHz, in the zero-field tensor). The spectrum was recorded at room temperature, in the absence of an external magnetic field. The ODMR line intensity is around 20% of the average fluorescence signal.

5.1.2 Dependency on the magnetic field

Upon applying an external magnetic field, levels X and Y are expected to part away proportionally to the magnitude of the magnetic field, due to electron Zeeman effect. Fig. 5.3 shows the cw ODMR spectrum of a single NV recorded in a low field (aprox. 20 G).

The Zeeman energy corresponding to this field magnitude is around 70

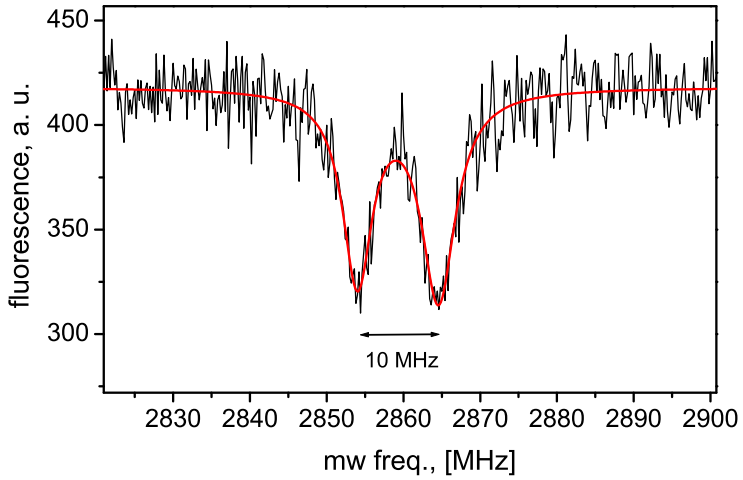

Figure 5.2: cw ODMR spectrum of a single NV center in B = 0 at room temperature. The center is not axially symmetric and the distance between the two lines corresponds to E = 10 MHz.

MHz. This is equal to the distance between the two lines in the figure. The ODMR contrast is similar to the one in the zero-field case.

The cw ODMR spectrum in Fig. 5.3 is typical for a single NV in a low magnetic field up to 500 G. The lower frequency line in the spectrum will present a smaller amplitude than the higher-frequency line due to mixing of the Z-level eigenstate into Y level ($m_S = -1$); the transition strength will decrease consequently, upon lowering the $m_S = -1$ eigenstate coefficient. This is also visible on the experimental spectrum, where the first line is weaker than the line at 2900 MHz.

The calculated variation of the triplet sublevels energies with the applied magnetic field is shown in Fig. 5.4. The Hamiltonian for this case is com-

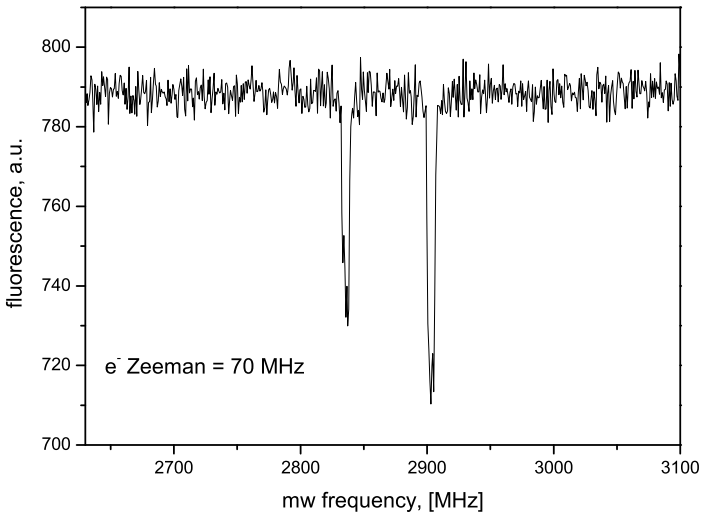

Figure 5.3: cw ODMR spectrum of a single NV in a low external magnetic field, B = 20 G; both lines present splittings due to hyperfine coupling to the nitrogen nucleus.

posed of the zero-field interaction and electron Zeeman energy for a center with axial symmetry. The magnetic field orientation was chosen along the molecular axis. Level Anti-Crossing occurs at 1020 G.

Fig. 5.5 shows the calculated angular dependency of the energy levels for a given magnetic field (B = 100 G). Thus for low angles of the magnetic field with the molecular axis, the electron Zeeman separation between the two lines is the highest. For higher values of the magnetic field orientation, the Zeeman energy decreases, with a minimum of the separation corresponding to a field perpendicular to the molecular axis. It is worth noting that for this value of the angle, the Z sublevel undergoes a change of its energy. The magnetic field applied with a non-zero orientation in respect with the molecular axis, leads to a change in the eigenstates composition of the Z level. As a consequence, the Z level will be described by (mostly) $m_S = 0$

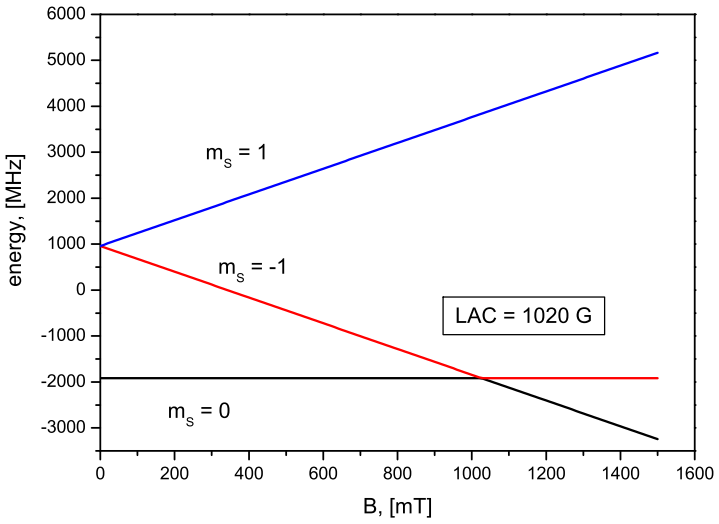

Figure 5.4: Calculated magnetic field dependency of the energy levels of the ground state triplet of an NV center. Level Anti-Crossing occurs at 1020 G.

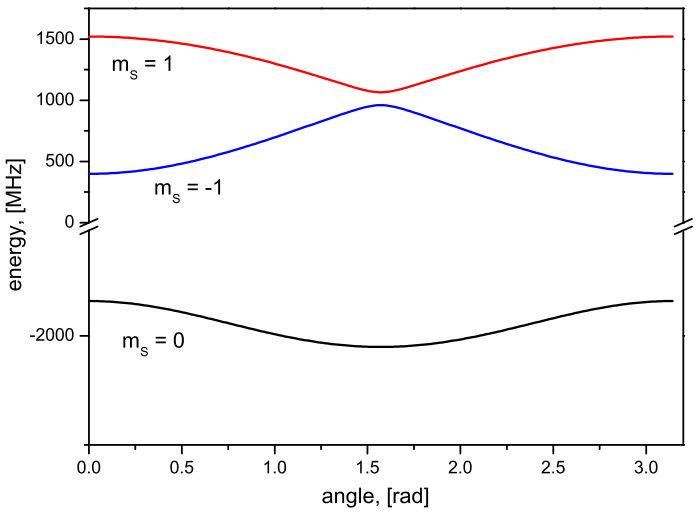

Figure 5.5: Calculated angular dependency of the energy levels for a given magnetic field amplitude.

eigenfunctions, as well as a $m_s = \pm 1$ component, which under the influence of the magnetic field will result in a Zeeman shift. The effect is maximum for a perpendicular field.

Well defined ESR lines can be observed in the experimental spectrum in a low-field low-angle regime. The Zeeman separation is maximum and the effects due to the orientation of the magnetic field are minimal. However, since finding the orientation of the magnetic field could be experimentally difficult, applying a high magnetic field would prevent orientation-related effects. For a high field, even applied perpendicular to the axis, the separation between the X and Y levels would be large enough to provide a good basis for pulsed experiments.

5.1.3 Hyperfine coupling to ^{14}N

The nitrogen nucleus in the NV center has a spin I = 1 leading to the presence of hyperfine and quadrupole terms in the Hamiltonian describing the system. The hyperfine and quadrupole interactions associated with the nitrogen nucleus in NV have been studied before for bulk NV centers [HMF93]. The hyperfine and quadrupole constants are: $A_{||}$ = 2.3 MHz, $A_{\perp}$ = 2.1 MHz for the hyperfine constants, and P = -5.01 MHz for the quadrupole [HMF93, LvW77, RMK87]. The hyperfine interaction constants are rather low in comparison with the ones corresponding, for instance, to ^{13}C nucleus (A = 130 MHz) [LLH04]. This is due to the value of the electron spin density associated with ^{14}N, 0.2%, significantly lower than 72%, corresponding to ^{13}C [HMF93].

The low coupling of the electron to the nitrogen nuclear spin leads to

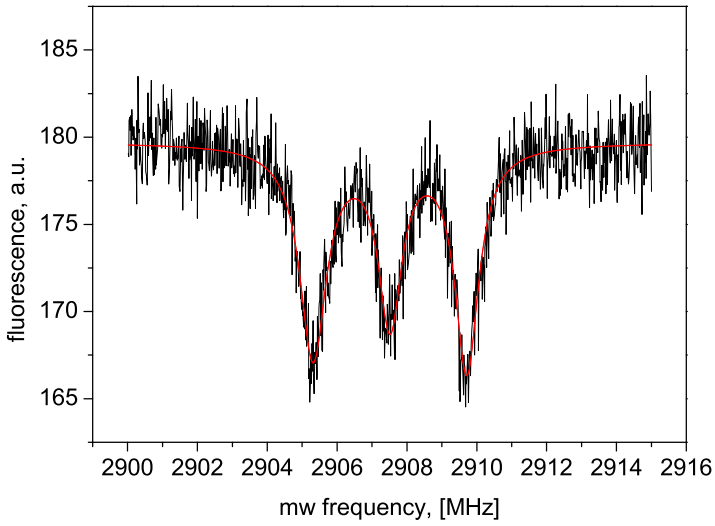

Figure 5.6: High-resolution experimental cw ODMR spectrum showing the lines resulting from the coupling to ^{14}N.

the absence of clearly visible additional splittings in the ODMR lines, for experiments performed with lower microwave frequency resolution. However, upon increasing the resolution of cw ODMR experiments, (this can be done by decreasing the range of microwaves, while keeping the number of frequency steps constant), the splittings resulting from the coupling to nitrogen nucleus become visible. A high-resolution cw ODMR spectrum is shown in Fig. 5.6. Three equally intense lines are visible in the spectrum, resulting from coupling the nitrogen nucleus. The spectrum was recorded in the absence of a magnetic field. Thus, each of the lines in the previously shown cw ODMR spectra will present such splitting.

Fig. 5.7 shows the the change in the original triplet state sublevels as a result of the hyperfine and quadrupole coupling to ^{14}N nucleus, using the parameters mentioned above. The Hamiltonian for this case included the

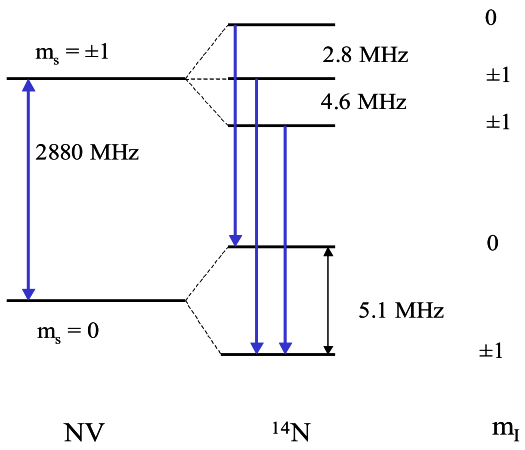

Figure 5.7: Calculated energy levels scheme for a single NV electron spin coupled to a single ^{14}N nuclear spin. The calculation parameters are given in the text.

zero-field term, and the hyperfine and quadrupole interactions. The center was consider symmetric, i.e., E = 0. The transitions frequencies present in Fig. 5.6 are reproduced and shown by arrows in the energy levels scheme of Fig. 5.7.

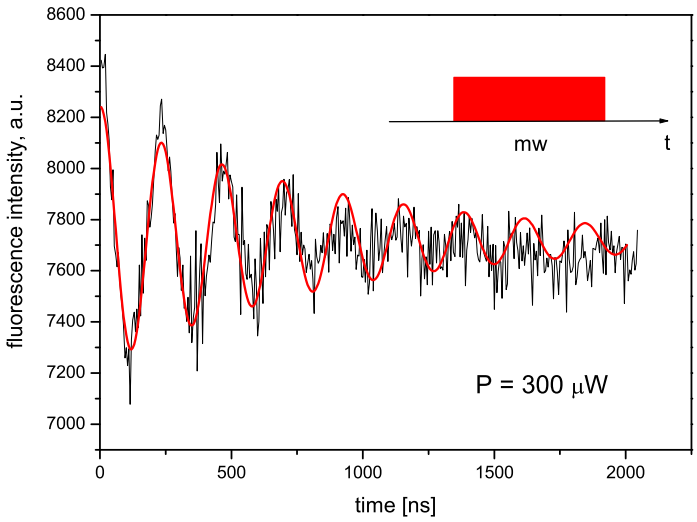

Figure 5.8: Optically detected transient nutations for a single NV defect

5.2 Pulsed ODMR on single NV centers

5.2.1 Transient nutations on single NVs

Recording the transient nutations of a spin system is the easiest way to probe its coherence properties. In the case of the NV center, nutations are generated by the microwave irradiation with a frequency corresponding to zero-field splitting in the ground state and detected optically. The interaction with microwaves leads the system into oscillation between absorption and emmission processes. As a result, the populations within the triplet ground level will change accordingly, inducing modulations in the population differences and, implicitely, in the fluorescence response of the system.

Transient nutations for single NVs have been recorded under continuous laser illumination (537 nm) by monitoring the fluorescence intensity for the time a microwave pulse is applied. Each point recorded is corresponding to a

time bin in the microwave pulse (10 ns). Fig. 5.8 shows the result of a transient nutation trial on a single NV center. The laser power used was 300 μW. The nutation curve shows a decay of the nutations within 1 μs. However, the nutations decay time alone does not provide the decoherence time of the system. Inhomogeneous line broadening occurs even in the case of a single system under study. In an ensemble of spins inhomogeneous line broadening is due to the different environments the spins packets experience throughout the sample in use. Thus, there is a distribution in the Larmour precession frequencies due to the interactions with different lattice environments, or hyperfine and quadrupole couplings with neighboring nuclei. In the case of a single NV center, the ensemble average is replaced by the time average, i.e., the center will experience different environments at different times, leading to a similar distribution in the Larmour frequencies as in the ensemble case. Since the measurement is done by accumulation, the time necessary for obtaining a nutation curve is long enough for a significant change in the Larmour frequencies. Furthermore, as will be seen in the next subsection, the decay time of the nutations is strongly influenced by the optical power of the laser. Thus, it is preferable to employ methods for manipulating the spins in the absence of the laser, i.e., keeping the laser only for the readout period, opposite to continuous illumination as in the present case.

5.2.2 Optical readout influence on the decoherence time

The fluorescence response of the system in ODMR experiments is given by the excitation laser intensity. Thus, a higher ODMR contrast can be obtained employing higher laser powers, up to saturation regime. As mentioned already, initial transient nutations were performed in a continuous laser illumination regime. However, upon increasing the laser power, it was observed

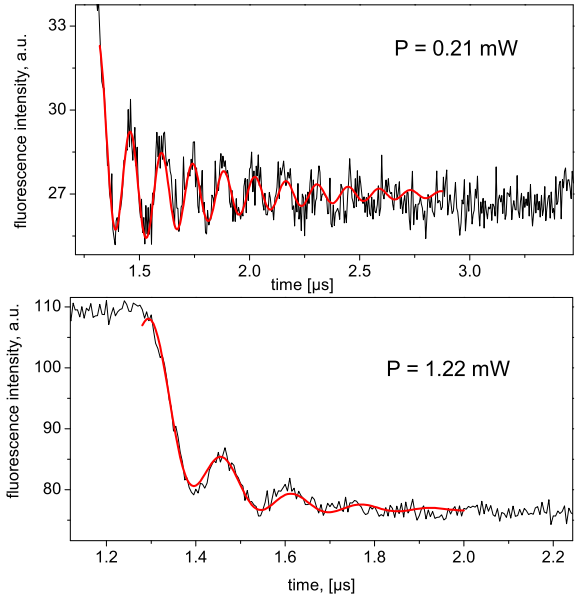

Figure 5.9: Transient nutations recorded with two different laser powers. The red curve indicates simulations of transient nutations.

a variation in the decoherence time of the single electron spin of the NV. Fig. 5.9 shows the transient nutations recorded for two different laser powers. It can be observed that the nutation decay time for higher laser powers is lower than in the case corresponding to the lower power. The red lines in Fig. 5.9 show a calculated nutation curve, accroding to the 5-level model presented in Chapter 3. The nutation decay time, i.e., the time in which the system can be coherently driven between the sublevels of the triplet state, should not normally be affected by the readout procedure, since it is an intrinsic property of the system.

The decoherence rate of the system was measured for several laser powers and it is shown in Fig. 5.10. The decay rate of the nutations increases linearly with the laser power. The continuous line represents a fit to the

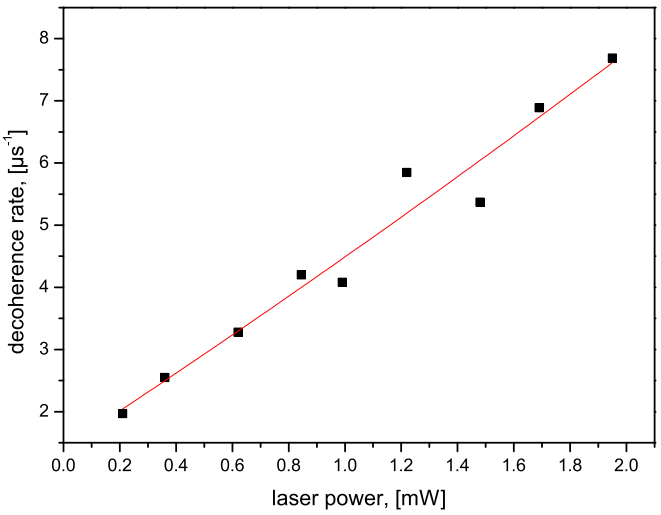

Figure 5.10: The decay rate of the transient nutations increases linearly with the laser power, showing the effect of the laser readout on the coherent evolution of the system. The continuous line represents decay rates, calculated using the model presented in Chapter 3.

calculated values for the corresponding powers used. Since the laser is used for readout only, it can be assumed that the variation of the nutations decay rate comes as an effect of the measurement upon the system. Further on, this issue is going to by analyzed.

5.2.3 Quantum Zeno effect

The common approach towards quantum measurement description is given by the von Neumann's reduction postulate. This states that, upon a mea-

surement performed on a quantum system, the wavefunction describing that system collapses or is reduced to one of its eigenstates. To illustrate this, the case of a system with two energy levels can be considered. The wavefunction of the system is given by a linear combination of the two associated eigenstates

$$\psi = a\,|\varphi_1\rangle + b\,|\varphi_2\rangle \tag{5.1}$$

where φ_1 and φ_1 are the eigenvectors and a and b their coefficients, respectively. The initial density matrix corresponding to this is given by

$$\rho_0 = \begin{pmatrix} |a|^2 & ab^* \\ a^*b & |b|^2 \end{pmatrix} \tag{5.2}$$

The diagonal elements of the density matrix are the populations of the levels, or the probability the levels are occupied, and the off-diagonal elements are coherences between them.

According to the von Neumann's reduction postulate, ρ_0 will undergo a change after the measurement. The wavefunction is converted from a superposition of eigenvectors to a mixture of the same states. In the density matrix formalism, this can be written as

$$\rho_0 \rightarrow \rho = \begin{pmatrix} |a|^2 & 0 \\ 0 & |b|^2 \end{pmatrix}. \tag{5.3}$$

This process is commonly known as decoherence, and it leads to null off-diagonal elements in the density matrix. Practically, decoherence follows as a consequence of the interaction of the system with the environment, a system with a large number of degrees of freedom, compared with the quantum system of interest. In the case of the NV center, the environment consists of the atoms in the diamond lattice. Their interactions with the center will

influence the decoherence time. This is an intrinsic property of the system, regardless of the state of the measurement. However, when measured, the measurement apparatus is added to the normal environment of the system. It is common to use the term environment for the measuring apparatus as well.

Due to the assumed projective nature of the quantum system, it is expected that significant effects will occur upon measurement. A significant effect is the so-called quantum Zeno effect: the inhibition of the quantum system dynamics upon a continuous measurement, i.e., the transition from one state to another is prevented by the high frequency of the measurement (infinite, if continuous). In the case of the two-level system, a measurement will be described in terms of probabilities of state occupation: $P_1 = |\varphi_1\rangle \langle\varphi_1|$ and $P_2 = |\varphi_2\rangle \langle\varphi_2|$, for levels 1 and 2 respectively, with the two eigenvectors orthogonal. If p is the probability that the system is located in state 2, then the probability of finding the system in state 1, after the measurement will be complementary, $q = 1 - p$.

For a continuous measurement, $N \to \infty$, the probability is equal to unity [MS77]. Thus, a continuous measurement will inhibit the transition between the two levels considered. As a consequence, the Rabi oscillations between two levels will be completely suppressed. The effect holds for as long as the probability of spontaneous decay is quadratic in time; for a linear dependence no inhibition occurs. Subsequently, the ideal system for checking on the Zeno effect will be one with a very low decay rate.

The three-level system in Fig. 5.11 was suggested by Cook [Coo88] for

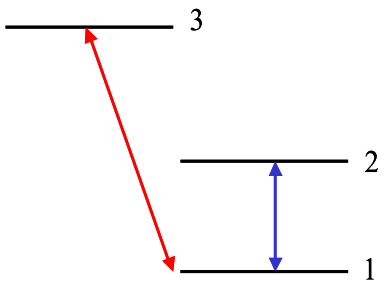

Figure 5.11: Proposed three level system for experimental tests of quantum Zeno effect. The transition between levels 1 and 2 is recorded. The level 3 is used for measurement only.

experimental verification of the quantum Zeno effect. The model was later realized experimentally by the group of Wineland [IHBW90]. The two states labeled 1 and 2 are the states where the Zeno effect occurs. The state 3 is used for measurement. Transitions between states 1 and 2 can be induced by microwave or rf radiation, while the transition from 3 to 1, e.g., fluorescence photons, can give information about the state of the system.

The system proposed by Cook is similar to the energy levels scheme of the NV defect. Thus states 1 and 2 can be identified within the ground triplet state, corresponding to states Z and X, provided the defect presents axial symmetry. State 3 corresponds to the excited level. In the case of ODMR on NVs, the fluorescence photons from transition 3 to 1 give information about the state of the system. The presence of the fluorescence photons indicates the system is in state 1 (or Z, respectively). The measurement is given by the fluorescence photons. The decay within the sublevels of the NV ground state

is negligible. By applying microwaves in resonance with the ground level splitting, Rabi oscillation are induced. As seen in the previous subsection, the nutation time decreases upon increasing the laser power, a proof of Zeno effect. The calculations using the model described in Chapter 3 agree with the experimental data. The Liouville equations describing the dynamics of the density matrix contain already the measurement process, i.e., the laser pumping, and the radiative decay to the ground level. The measurement can be considered continous; the duration between individual photons in the excitation light as well as in the fluorescence light is small enough (400 kcounts/s in the saturation regime for the fluorescence light from a single center in nanocrystals). Higher laser powers imply higher fluxes of photons and implicitly a higher frequency of measurement.

However, the Zeno effect can be verified only partially in the case of single NVs. The probability of populating the singlet metastable level increases with the laser power; furthermore in the actual model, the fine structure of the excited triplet was not considered. As mentioned in the previous chapter, the decay rate from the higher sublevels of the excited state to the singlet metastable level is considerably higher, in the order of kHz. For a nonselective excitation with high laser powers, it is expected that the population of the singlet state will play a significant role within the photokinetics of the system. The simple scheme shown in Fig. 5.11 will not hold valid anymore, since the singlet population cannot be neglected. Consequently, the system in the high laser power regime might not give an accurate test of the Zeno effect.

5.2.4 Hahn echo on single NVs

Due to the inhomogeneities associated with the system, the transient nutations experiments will not give a correct value for the spin dephasing time.

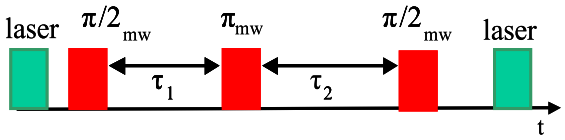

Figure 5.12: Schematic representation of the Hahn echo pulse sequence used

To determine the decoherence time for the single electron spin, a Hahn echo procedure was approached. The conventional spin echo method helps eliminate the inhomogeneities related to the system. However, for the actual purpose, the conventional pulse echo sequence has to be modified in order to provide optical readout.

The sequence applied to a single NV is pictured in Fig. 5.12. The first laser pulse is used to polarize the system in its $m_s = 0$ state. The next pulses follow according to the conventional scheme. The first microwave pulse excites the coherences, i.e., the populations are converted into coherences between sublevels of the triplet state. In classical terms, this corresponds to changing the direction of the magnetization vectors, from longitudinal to transversal. For a fixed time period τ_1, the system is left unperturbed and the coherences evolve in the transverse plane. For the ensemble case, this will correspond to a spread in the transverse magnetizations due to different Larmor frequencies of different spin packages. In the case of a single system however, the ensemble average is replaced by a time average, leading to a similar distribution of Larmor frequencies but in time. Since the experimental data are obtained by accumulation of the repeated pulse sequences, the

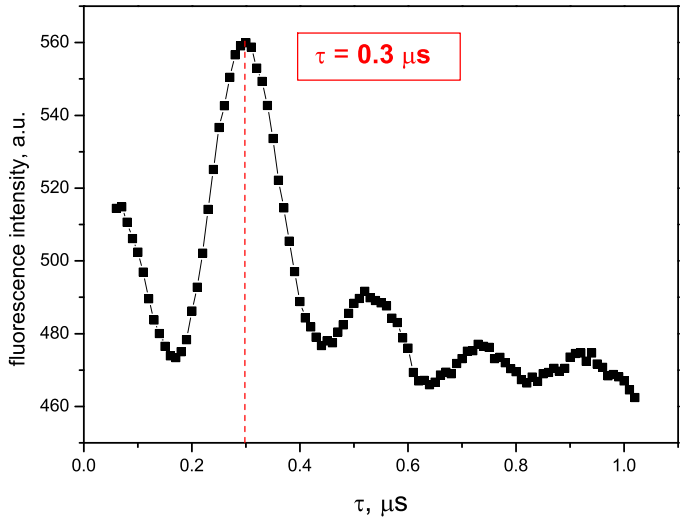

Figure 5.13: Hahn echo at 0.3 μs

electron spin will exhibit different rotation frequencies. Refocusing of the coherences is done by applying a microwave π-pulse. The next time interval the system is not acted upon, τ_2, is variable. For $\tau_1 = \tau_2$ the refocused signal is at maximum intensity. However, in order to extract the signal, the coherences must be converted back into populations, whose differences can by optically read out.

Fig. 5.13 shows the experimental results of a Hahn echo applied to a single NV, with a maximum echo amplitude for a time preset of 0.3 μs. Lower intensity echo replica can be observed for values corresponding to $2\tau_1$ and $2\tau_2$.

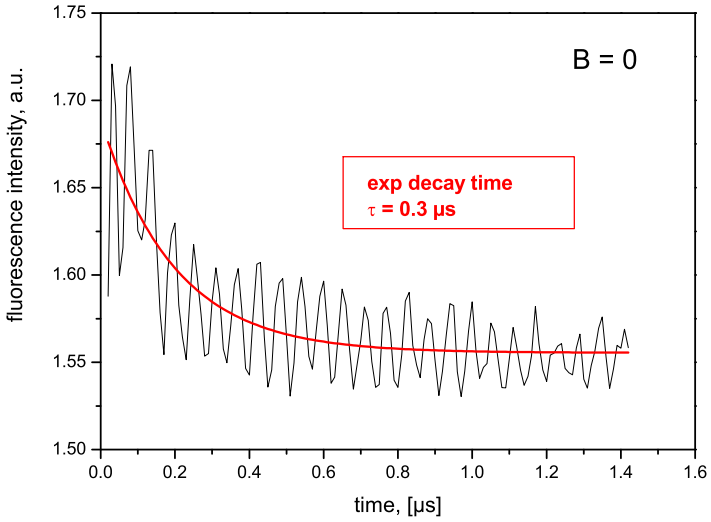

Figure 5.14: The Hahn echo decay exhibits a strong modulation due to the asymmetry of the defect investigated. For this center E = 17 MHz. The exponential decay fit (in red) shows a decoherence time of 0.3 μs, similar to the value obtained following a Hahn echo.

An alternative way of determining the decoherence time for the system is given by a modified Hahn echo procedure, know in conventional magnetic resonance as ESEEM (Electron Spin Echo Envelope Modulation)[Mim72]. The new sequence differs from the previous one by setting $\tau_1 = \tau_2$ =variable. By increasing the time set between the pulses, a decay of the primary echo can be observed. The exponential decay will give the decoherence time of the system. The eventual modulation of the decay provides information about the hyperfine structure of the system.

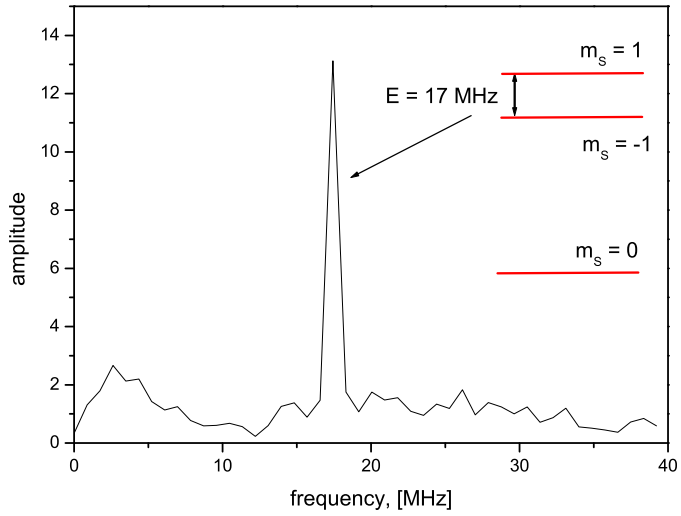

Figure 5.15: The Fourier tranform of the data shown in Fig. 5.14 proves the diference between the two ESR allowed transitions. The inset shows schematically the energy levels within the ground state.

Fig. 5.14 shows an echo decay on a single electron spin. The exponential decay fit results in a decoherence time of 0.3 μs, equal to the result obtained with a Hahn echo sequence. However, the decay patter presents a strong modulation superimposed on it. The Fourier transform in Fig. 5.15 gives a modulation frequency of around 17 MHz. The modulation comes as a result of an interference between ESR allowed transitions. For the present case, two ESR transitions can occur in a center without the three-folded axial symmetry. In this case, the X and Y levels will be separated by parameter E, usually in the range of 10-20 MHz. The Rabi frequency of the microwaves (40 MHz) exceeds the separation between the two levels, exciting thus both ESR transition, from Z to X and Y respectively.

If external magnetic field is applied, it will result in a Zeeman separation between the X and Y ground sublevels, additional to the one given by pa-

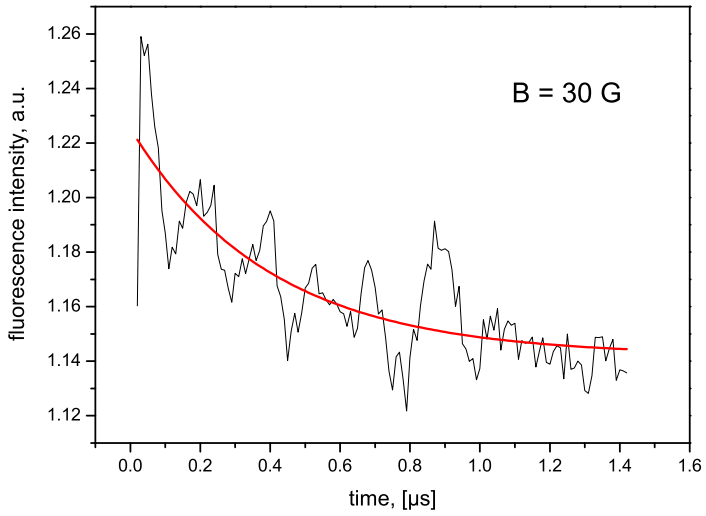

Figure 5.16: Upon applying an external magnetic field, the X and Y sublevels are parted by a separation higher than the Rabi frequency of the microwaves and the beating between the two main ESR transitions does not occur.

rameter E. Provided that the Zeeman energy is higher than the microwave Rabi frequency employed, i.e., a higher difference between the frequencies at which the two allowed ESR transitions occur, the interference between the two transitions will disappear.

Fig. 5.16 shows the modulation pattern obtained in the presence of a magnetic field of 30 G. The fast component of the modulation is not present anymore, as expected.

The Fourier transform shown in Fig. 5.17 reveals several lines, around 5 MHz. The slower component in the Hahn echo decay is given by the hyperfine coupling to ^{14}N nucleus. The hyperfine levels allow several ESR transitions, separated by a few MHz (refer to the calculated energy levels scheme shown previously in this chapter). The remaining modulation in the echo decay will be then given by the interference between these transitions.

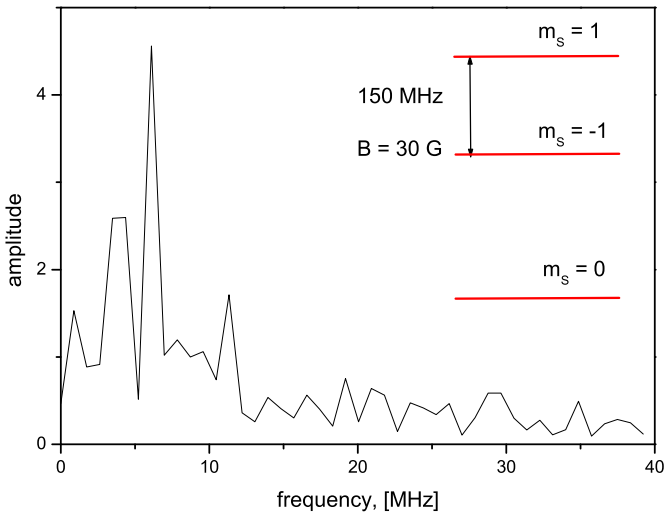

Figure 5.17: The Fourier transform of the data in Fig. 5.16 reveals the hyperfine coupling to ^{14}N.

Chapter 6

ODMR on single NV hyperfine coupled to ^{13}C

A first attempt to scale up the number of systems that can be used as qubits is given by the hyperfine coupling of the NV with neighboring nuclei. As seen from the previous chapter, the electron spin of the NV is hyperfine coupled to the nuclear spin of ^{14}N. The hyperfine coupling for this case is around 2 MHz, rather small for practical purposes. The resultant levels would be into a few MHz range of energy separation, lower than the Rabi frequency of the applied microwaves pulses. This would lead to a non-selective addressing of the hyperfine levels. A possible solution would consist of applying an external magnetic field, in order to increase the separation between levels. However, this would involve a strong coupling between different eigenstates, which would prevent addressing the system on the base of individual spin states. The most abundant carbon isotope in diamond is ^{12}C (natural atomic abundance 98.93 %). The spin of ^{12}C is $I = 0$, and therefore the hyperfine interaction with NV's electron spin is zero. The ^{13}C occurs with a 1.07 % natural abundance, and has a nuclear spin $I = 1/2$, resulting in a hyperfine

splitting of the electron levels of NV. The potential use of single ^{13}C nuclear spins had been proposed by Wrachtrup *et al.* [WKN01]. Based on the natural abundance of ^{13}C, one out of 30 NV defect experiences a hyperfine coupling with a nearest ^{13}C nucleus. However, it is possible to use ^{13}C enriched diamonds, up to the limit of 100 %. For this case, the NV electron spin could be coupled to three ^{13}C nuclear spins in the first coordination shell, and nine ^{13}C in the second coordination shell. The hyperfine coupling constant for the first coordination shell is 130 MHz, decreasing to 70 MHz for the second shell. It is estimated that for ^{13}C nuclei located in the third coordination shell, the hyperfine coupling is around 10 MHz. The ^{13}C nuclear spin cannot be readout out optically in a direct way. The nuclear states are readout via the electron states of the NV center.

Here, the hyperfine coupling of a single NV electron spin to a single ^{13}C nuclear spin is analyzed. The cw ODMR spectra of the system is presented and compared to calculated values for the transitions energies and probabilities. The state of the experimental setup did not allow the study of angular dependency of the hyperfine coupling. Therefore, an isotropic hyperfine constant A = 130 MHz will be assumed for calculations. Pulsed experiments on the nuclear spins are discussed together with possible cause leading to decoherence.

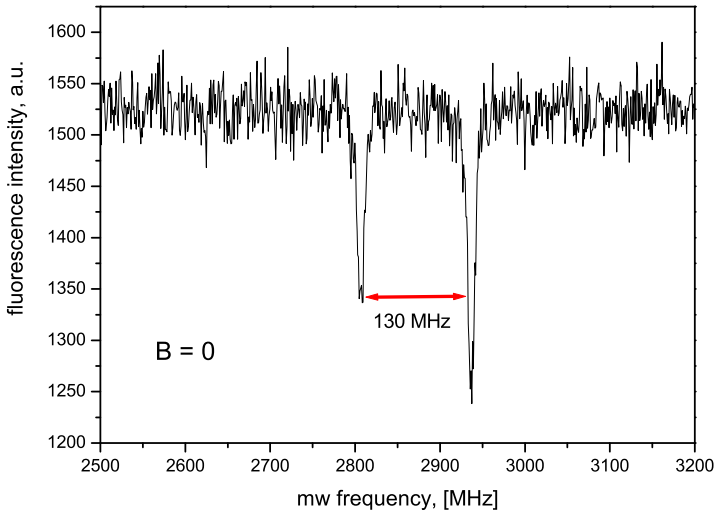

Figure 6.1: Zero-field cw ODMR spectrum of a single NV center hyperfine coupled to a single ^{13}C nucleus. The splitting between the two lines is the hyperfine coupling constant, A = 127 MHz.

6.1 Continuous wave ODMR results

6.1.1 ODMR spectra of (NV, ^{13}C) system

Continuous wave ODMR experiments have been performed on Type Ib synthetic diamond nanocrystals. Fig. 6.1 shows the spectrum obtained on a single NV coupled to ^{13}C in the absence of an external magnetic field. The spectrum was obtained by sweeping the microwaves over a range of frequencies under laser illumination. The NV center is axially symmetric. The fluorescence is recorded from $m_S = 0$ state coupled to the ^{3}E level. A green laser has been used for excitation. The ODMR effect is negative, similar to cw ODMR on single NV centers.

For B = 0, the cw ODMR spectrum exhibits two ESR transitions, while in

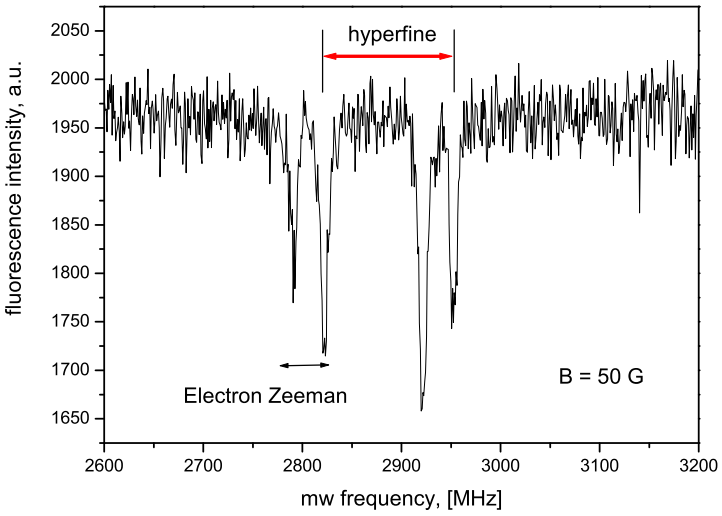

Figure 6.2: cw ODMR spectrum of a single NV center hyperfine coupled to a single ^{13}C nucleus in a small magnetic field (B = 10 G). The two lines in the zero-field spectrum split into two lines, with the separation given by the electron Zeeman energy.

the presence of a magnetic field the spectrum is composed of four lines. The lines in both spectra show slightly unequal ODMR contrast, most probable related to readout effects. On top of each line very small splittings (around 3 MHz) are visible. Besides the hyperfine coupling to ^{13}C, the electron spin of the NV is subjected to hyperfine coupling to ^{14}N. However, the hyperfine coupling constant to the nitrogen nucleus is 2 MHz, much smaller than the that corresponding to ^{13}C nucleus. Upon coupling an electron spin to two different species of nuclear spins, the nucleus with lower hyperfine coupling will constitute a perturbation to the interaction between the electron spin and the nuclear spin with higher hyperfine coupling constant.

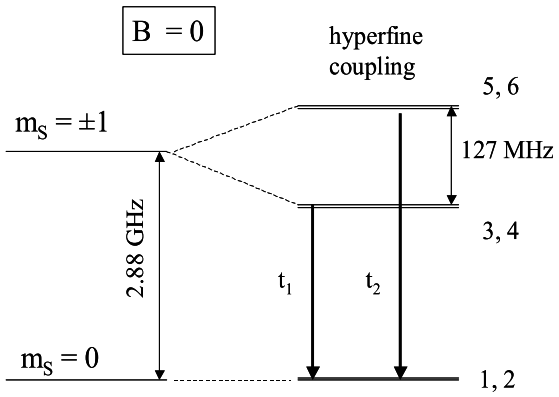

Figure 6.3: Calculated energy level scheme for a single NV coupled to a ^{13}C in zero-field. The resulting three levels are degenerated (refer to Table 6.1 for the eigenvectors corresponding to each energy level). The two ESR allowed transitions are shown here with t_1 and t_2.

6.1.2 ODMR spectra analysis

The energy levels scheme of the system has been calculated using the approach presented in Chapter 3. The following parameters have been used in the calculations: D = 2880 MHz, E = 0, $g_{||} = 2.0028$, $g_{\perp} = 2.0024$, $\beta_e = 1.44$ MHz/G, $\beta_n = 0.782 \times 10^{-3}$ MHz/G, $g_n = 1.4048$. The fit parameters are the hyperfine constant, the angle between the magnetic field and molecular axis, and the intensity of the magnetic field.

Fig. 6.3 illustrates the energy levels scheme in the zero-field case. The resulting eigenfunctions with their coefficients are in Table 6.1. In the absence of an external field, the energy level scheme consist of three double-degenerated levels. Each of the three levels has in its components both nuclear spin projections. Thus, the ground level corresponds to the electron

spin projection $m_S = 0$ and does not split under hyperfine interaction, due to the zero magnetic dipole. The hyperfine splitting is observed on top of the electron states X and Y, corresponding to $m_S = 1$ and $m_S = -1$, respectively. An isotropic hyperfine constant A = 127 MHz fits well the frequencies at which transitions shown in Fig. 6.1 occur.

Table 6.1: The eigenfunctions corresponding to energy levels of an NV center hyperfine coupled to a ^{13}C in zero-field. The eigenvectors are in the form $|m_S m_I\rangle$. The energy levels are denoted E_1 to E_8, with E_1 the lowest (see Fig. 7.6). Note that each level is double-degenerated.

	E_1	E_2	E_3	E_4	E_5	E_6
$\left\|1\frac{1}{2}\right\rangle$	0	0	0	0	1	0
$\left\|1-\frac{1}{2}\right\rangle$	0	0	1	0	0	0
$\left\|0\frac{1}{2}\right\rangle$	1	0	0	0	0	0
$\left\|0-\frac{1}{2}\right\rangle$	0	1	0	0	0	0
$\left\|-1\frac{1}{2}\right\rangle$	0	0	0	1	0	0
$\left\|-1-\frac{1}{2}\right\rangle$	0	0	0	0	0	1

Upon applying an external magnetic field, the upper levels in Fig. 6.3 are expected to split due to mainly the electron Zeeman interaction. The resulting energy levels scheme is shown in Fig. 6.4. The Zeeman energy separation is 30 MHz, corresponding to a low magnitude of the applied field, B = 10 G. The orientation of the field is along the molecular axis (see next section for the angular dependency of the energy levels). For the considered field, the nuclear Zeeman energy can be neglected. The ground state is still double-degenerate under these conditions.

Table 6.2 gives the eigenfunction identification for each of the levels for the general case of a NV coupled to ^{13}C in magnetic field, oriented at an angle

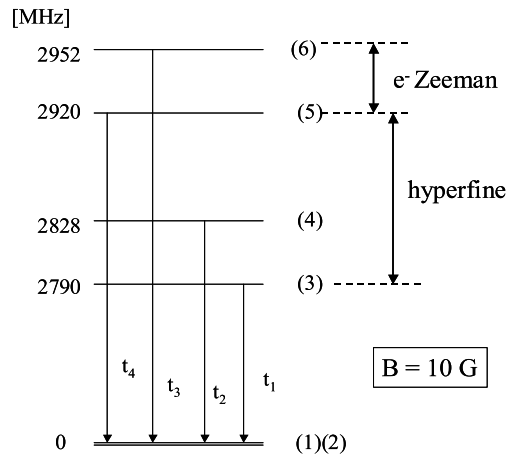

Figure 6.4: Energy levels scheme for a single NV coupled to a ^{13}C in a low magnetic field (B = 10 G), oriented along the molecular axis.

$\pi/3$ in respect with the molecular axis. The ground state consists of linear combinations of $\left|0-\frac{1}{2}\right\rangle$ and $\left|0\frac{1}{2}\right\rangle$, with eigenfunction in the form $|m_S m_I\rangle$. For low values of the magnetic field the ground level is still degenerated. However, upon increasing the magnetic field the splitting in the ground level becomes obvious. Levels 3 to 6 are non-degenerated.

6.1.3 Magnetic field dependency

The cw ODMR spectrum in Fig. 6.2 contains four lines given by the ESR allowed transitions within the energy level scheme at low fields, quasi-aligned to the molecular axis. For spectra recorded in different experimental conditions, i.e., higher magnetic fields and different single NV centers coupled to ^{13}C, the number of lines doubles. For instance, the spectrum in Fig. 6.5 exhibits eight lines in a four-doublet configuration.

Calculations done for low magnetic fields aligned with the molecular axis

Table 6.2: The eigenfunctions corresponding to energy levels of an NV center hyperfine coupled to a ^{13}C in the presence of an external field, B = 10 G oriented at an angle $\pi/3$ in respect to the molecular axis. The lowest two levels are degenerated.

	E_1	E_2	E_3	E_4	E_5	E_6
$\left\|1\frac{1}{2}\right\rangle$	0	0	0	0	0	1
$\left\|1\frac{-1}{2}\right\rangle$	0	0	0	0	-0.49 - 0.86i	0
$\left\|0\frac{1}{2}\right\rangle$	-0.35 - 0.60i	-0.35 - 0.61i	0	0	0	0
$\left\|0\frac{-1}{2}\right\rangle$	0.35 - 0.60i	-0.35 + 0.60i	0	0	0	0
$\left\|-1\frac{1}{2}\right\rangle$	0	0	-0.49 + 0.86i	0	0	0
$\left\|-1\frac{-1}{2}\right\rangle$	0	0	0	1	0	0

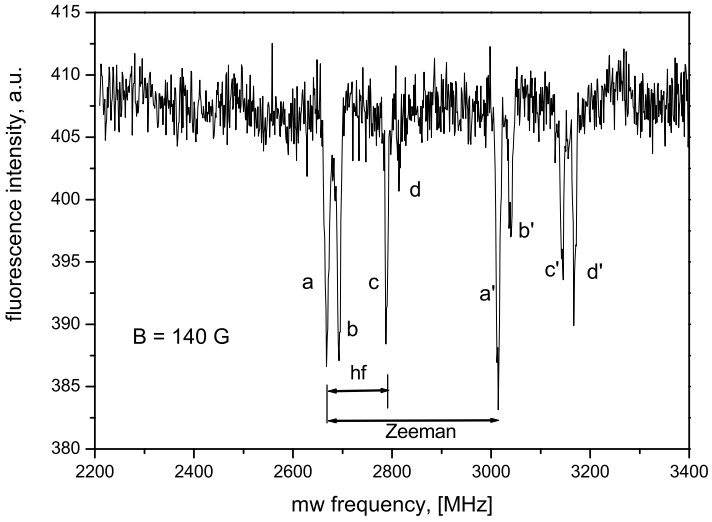

Figure 6.5: cw ODMR spectrum for NV coupled to ^{13}C in B = 140 G ($\theta = 26$ deg). The number of lines doubles from the precedent case, due to the splitting in the ground state caused by non-zero angle between the field and the molecular axis and the higher magnitude of the magnetic field. The transition in the spectrum are indicated for easier identification with the ones figured in the energy levels scheme (see Fig. 6.6)

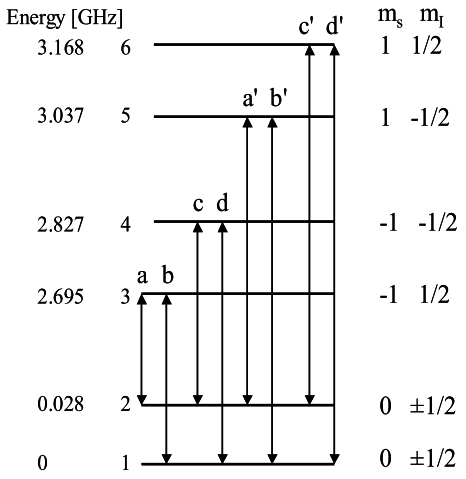

Figure 6.6: Calculated energy levels scheme for B = 140 G

resulting in the energy levels scheme in Fig. 6.4 show that the first two levels, 1 and 2 overlap, having the same energy in the case of low magnetic fields. Upon changing the relative orientation of the magnetic field to the symmetry axis, the configuration for these two levels changes. Fig. 6.6 illustrates the new scheme, assuming a field of 140 G oriented at an angle of 26 deg relative to the axis. Both magnitude and orientation of the magnetic field are used as fit parameters to the transition frequencies in Fig. 6.6. The levels 1 and 2 are in this case split, with a separation of 28 MHz. The electron Zeeman energy observable in the upper levels (difference between levels 3 and 5, for instance) is 340 MHz. The splitting between levels 3 and 4 corresponds entirely to the hyperfine coupling to ^{13}C. Based on $|\Delta m_S| = 1, |\Delta m_I| = 0$ rules for allowed ESR transitions, eight lines can be identified within the model.

Both levels 1 and 2 are given by linear combinations of $\left|0 -\frac{1}{2}\right\rangle$ and $\left|0\frac{1}{2}\right\rangle$ with equal coefficients. For the considered magnetic field strength, the separation between levels 1 and 2, given only by the nuclear Zeeman effect is

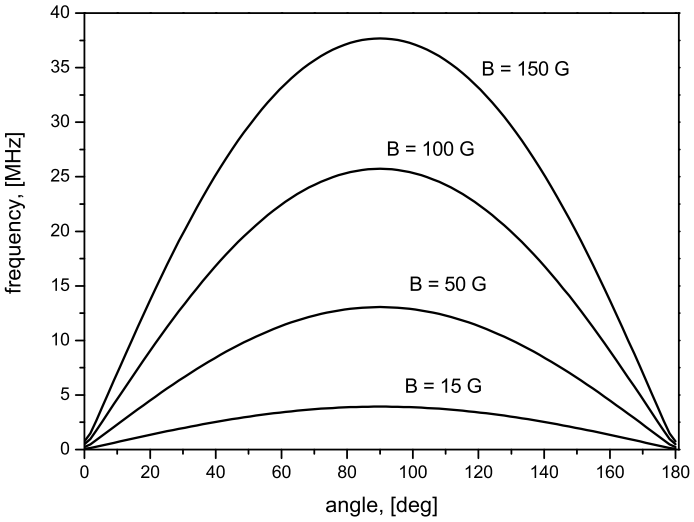

Figure 6.7: Angular dependency of the splitting in the ground state for different magnetic fields.

0.7 MHz, too small to be accounted for the actual value of 28 MHz. The splitting can be however explained by pseudo-nuclear Zeeman effect, consisting of cross terms between electronic Zeeman interaction and the magnetic hyperfine interaction [Ble67].

A pseudo-nuclear Zeeman effect has been reported in experiments on the triplet state of KCl:PO_2^- single crystals hyperfine coupled to spin-1/2 ^{31}P nuclei [SA80]. For this case unusually large splittings in the Z state ($m_S = 0$ state) resulted from pseudo-nuclear Zeeman interaction in low magnetic fields (up to 500 G). In the second-order perturbation theory, the splitting of level 1 is given by

$$\Delta E = \left(g_N \beta_N + g\beta \frac{A_\perp}{E_2 - E_1} \right) B_\perp \tag{6.1}$$

where the first term in the paranthesis represents the nuclear Zeeman

interaction, $A_\perp$ is the perpendicular component of the hyperfine tensor, and E_2 and E_1 are the energies of levels Z and X or Y in the triplet ground state of the NV, respectively. Assuming an isotropic value $A_\perp = A = 127$ MHz, and a separation energy between states X and Y of 2880 MHz, and a value of the magnetic field of 140 G, an estimate for the difference due to pseudo-nuclear Zeeman effect will be around 20 MHz which is in the range of experimental results. However, the splitting between levels 1 and 2 is strongly dependent on the orientation of the magnetic field. Fig. 6.7 shows the angular dependency of the separation for several magnetic field strengths. Thus, as expected, the separation increases upon increasing the magnetic field. For a field aligned with the molecular axis, the separation is zero. For a non-zero orientation angle, the overlaping effects between the electron and nuclear states become more intense, with a maximum at 90 deg.

6.1.4 Transitions

Transition probabilities have been calculated according to the procedure described in Chapter 3. The experimental cw spectra are obtained by accumulating a large number of microwave range sweeping, in order to improve the signal to noise ratio. Consequently, the variable component of the microwave magnetic field will be averaged out due to the random phase distribution of the field throughout the procedure. For this reason, the calculations of the transition strengths will take into account a constant microwave magnetic field.

Fig. 6.8 shows a stick plot representation of the transition amplitudes for the two cases simulated in Figs. 6.3 and 6.4, i.e., B = 0 and B = 10 G. In the absence of an external magnetic field, there are two lines, separated by the hyperfine coupling energy whose transition probabilities are equal (Fig.

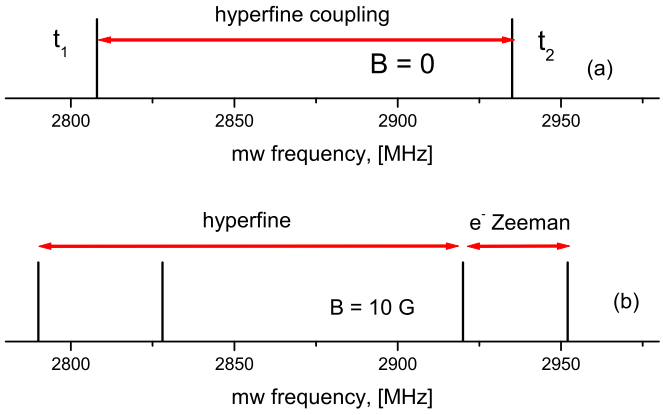

Figure 6.8: Transition probabilities for (a) B = 0, corresponding to Fig. 6.3 and (b) B = 10 G, corresponding to Fig. 6.4

6.8(a)). The same holds for the case of a very small magnetic field, B = 10 G. In Fig. 6.8(b), four lines are visible due to the electron Zeeman effect on the X and Y states of the NV triplet ground state. As seen in the previous section, for a very low magnetic field quasi-aligned to the molecular axis, the separation due to the pseudo-nuclear Zeeman effect is around 1 MHz, under the frequency resolution, and the nuclear Zeeman effect is completely neglectable. Due to the low magnitude of the magnetic field, the transition probabilities are expected to have equal values, confirmed by the calculations.

For a higher external field, B = 140 G, the transition probabilities have significantly higher values than in the zero-field case. For this case, the splitting in the lowest energy state is visible, leading to the eight lines in the spectrum. The calculated lines shown in Fig. 6.9 display slight differences in their amplitude. However, the differences are within 10% relative to each

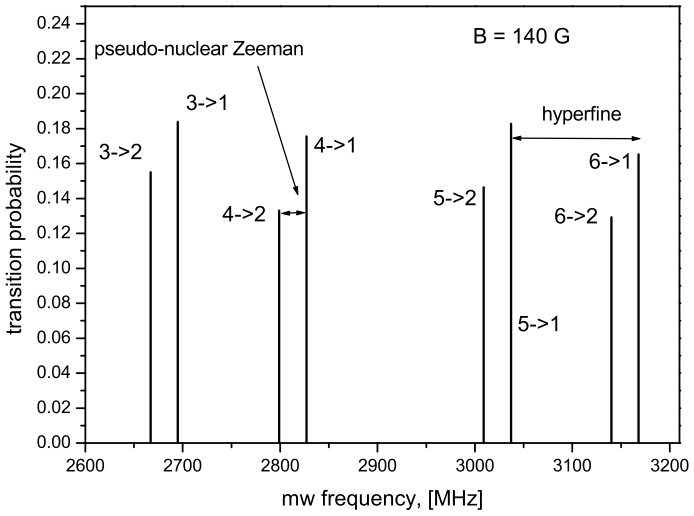

Figure 6.9: The calculated transition probabilties for B = 140 G

other and cannot account for the differences in the ODMR contrast for the lines shown in the experimental cw spectrum in Fig. 6.5. As mentioned previously, the optical readout effects as well as relaxation processes between hyperfine sublevels are not considered.

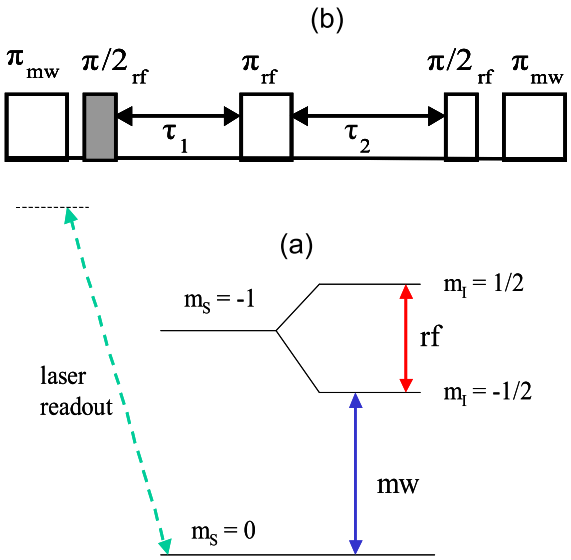

Figure 6.10: (a) Levels used for applying the Hahn echo sequence; the nuclear spin is readout out via the electron spin.(b) The Hahn echo pulse sequence

6.2 Spin dynamics

6.2.1 Decoherence time for single ^{13}C nuclear spins

In order to obtain information about the decoherence time of the single nuclear spin, a Hahn echo sequence was applied. The sequence was adapted for detection of single nuclear spins. As mentioned in the introduction to this chapter, the nuclear spins cannot be directly probed by the actual detection configuration, since the optical readout applies only to the electron states. Therefore, the electron spin is used to intermediate the detection and manipulation of single nuclear spin states.

Fig. 6.10(a) shows the levels of the NV+^{13}C system used for observing the spin echoes. For nuclear states, the hyperfine splitting of the triplet Y

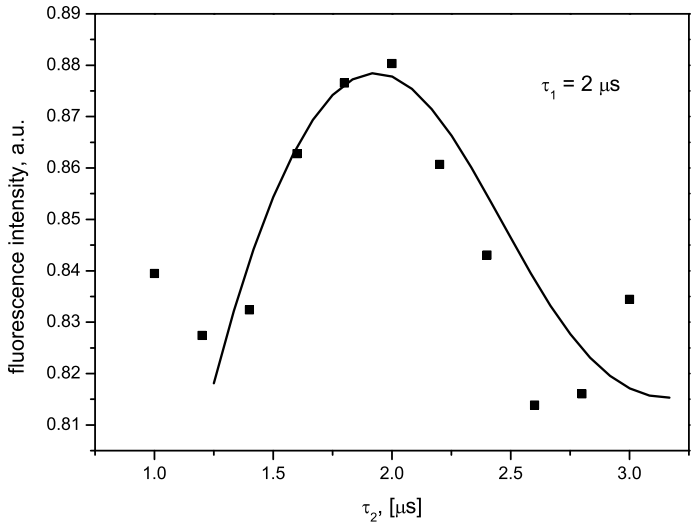

Figure 6.11: Hahn echo on a single nuclear spin at 2 μs. The symbols represent the experimental data, while the continuous line shows the result of a simulation.

state had been used. The two states correspond to $m_I = 1/2$ and $m_I = -1/2$. The lowest triplet level, Z ($m_S = 0$) is coupled to the hyperfine levels via microwaves, and provides the optical readout by transition to ^{3}E state. The applied pulse sequence was $\pi_{mw} - (\pi/2)_{rf} - \tau_1 - \pi_{rf} - \tau_2 - (\pi/2)_{rf} - \pi_{mw}$, with rf and mw representing the nature of the respective pulses. The first microwave π-pulse is used to excite the system to state Y. The microwave pulse is selective, in resonance with level 3. From here, a conventional rf Hahn sequence can be applied. The first rf π-half pulse excites the nuclear spin coherences and is followed after a delay τ_1 by an rf π-pulse for refocusing. The last rf π-pulse is used for converting coherences back to populations. In order to complete the optical readout, another mw pulse is needed to bring the system to the initial Z state. The experiment is averaged out over a large number of trials (50000).

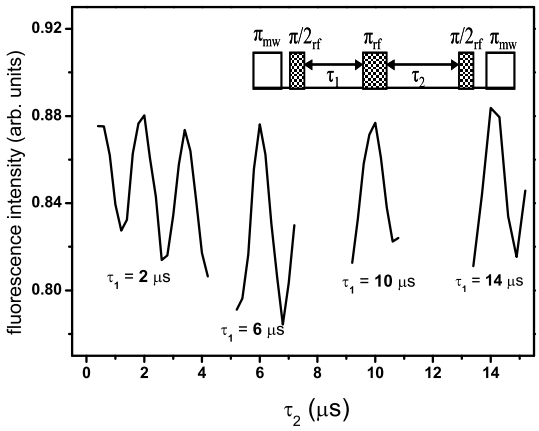

Figure 6.12: Series of Hahn echoes. The relative amplitudes of the echoes show no decay on the time scale shown.

A spin echo obtained for $\tau_1 = 2\mu$s is shown in Fig. 6.11. The solid line shows a simulation for the spin echo, performed with a modified model similar to the one presented in Chapter 3. The Liouville equations have been adapted to the new system accordingly, i.e., the levels resulted from hyperfine coupling have been included, resulting in a three-level system coupled to microwaves and radiofrequency fields. The optical readout occurs between the lowest energy level and the ^{3}E state (see Fig. 6.10a). The fit parameters are the dephasing $\Gamma_{rf} = 0.4$ MHz, the Rabi frequency of the rf, $\Omega_{rf} = 2.4$ MHz, the rf π-pulse, 162 ns, and the rf detuning $\delta = 9$ MHz.

Fig. 6.12 shows a series of Hahn echoes, recorded for different values of τ_1. The relative amplitude of the echoes shows no decay for a time range of up to 30 μs for single nuclear spins. Previously, it was reported a decoherence time of up to 100 μs for bulk ^{13}C nuclei [SSSA94]. Compared to the value obtained for single nuclear spins, it can be concluded that the hyperfine coupling to the electron spin of the NV center does not contribute as an additional source

of decoherence to the single nuclear spins.

Chapter 7

ODMR on two coupled NVs

So far, the NV defect and the system formed by the hyperfine coupling of the NV to a neighboring ^{13}C nucleus have been shown as suitable systems for qubit implementations. The single electron spin of the NV center has a long decoherence time, not significantly affected by the strong hyperfine coupling to surrounding nuclear spins. However, to meet the fundamental criteria for a quantum computer, the system must be scalable. The coupling to the ^{13}C nuclei in the first and second coordination shells can give the possibility of scaling up the system.

A significant increase in the number of qubits can be achieved by magnetic dipolar coupling of several NV centers. An advantage of this approach over scaling by using the neighboring nuclei is given by the fact that patterns of defects can be created within the range of interaction of magnetic dipoles, thus controlling the interaction between centers. A possibility to achieve this is by performing nitrogen high precision ion implantation into diamond, in order to generate NV centers. This would allow to create regular patterns of NV centers in the diamond lattice. The distance between defects in such patterns should not exceed the distance for which the dipolar coupling strength

is lower than the optical linewidth. Within a pattern of defects, the strongest interaction is between adjacent centers, due to the rapid decrease of the magnetic dipolar interaction energy with the distance between centers. Thus, it is important to understand the structure and dynamics of two coupled defects, in order to proceed further with higher order couplings. In this chapter, the magnetic dipolar interaction between two NV centers is investigated and the possibility to manipulate the spin states of the resulting system is analyzed. The energy level scheme for two coupled NVs was calculated using two approaches: a detailed Hamiltonian approach and a perturbational approach. The former takes into account all the possible interactions between the four electrons involved in the coupling between the two centers. In the perturbational approach, the inter-center dipolar interaction is considered a perturbation to the Hamiltonian of separated NV centers. This is justified by the fact that, for instance, for a separating distance of 1 nm, the dipolar interaction energy is around 15 MHz, much smaller in comparison with the zero-field energies of individual NVs (2.9 GHz). Further on, the decoherence time of the electron spin of the system is measured.

The experiments on two coupled NVs were carried out using the same experimental setup previously described in this work. The continuous wave experiments have been performed under similar conditions to those used in the case of a single NV defect: the microwaves were swept over a range of frequencies under laser illumination providing the optical readout. Fig. 7.1 shows the cw spectrum of two coupled NVs. The spectrum was taken in a magnetic field of around 70 G, and consists of two doublets, separated by

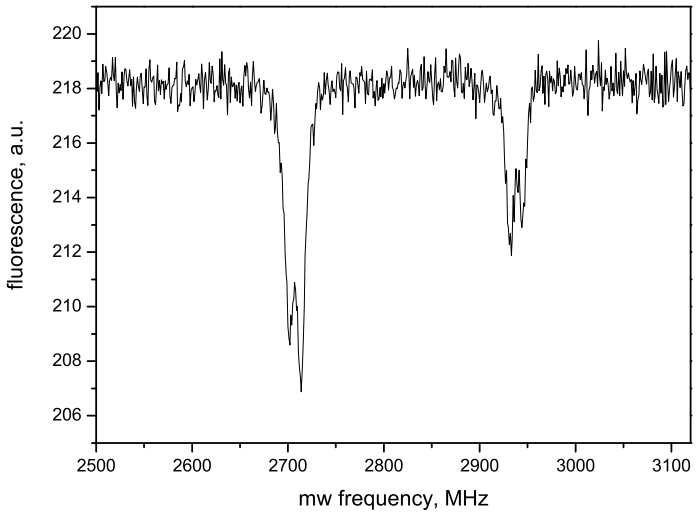

Figure 7.1: cw spectrum of two coupled NVs. The spectrum consists of a set of two doublets. The separating energy within each doublet is given by the dipolar coupling between the centers.

the Zeeman energy corresponding to the two NVs. The separation energies between the two lines within each doublet are equal. Upon increasing the applied magnetic field, the separation energies between the lines within each doublet does not change. Thus, it can be assumed that this is given strictly by the dipolar interaction between the two centers. This is going to be confirmed by the calculations in the next sections.

7.1 Detailed Hamiltonian approach

The detailed Hamiltonian approach is based on the paper by Benk and Sixl [BS81], where it was developed in order to calculate the spectrum and transitions for two coupled triplet states of bicarbene structures. Fig. 7.2 shows the geometrical representation of a pair of coupled NV centers, separated by the distance $\mathbf{R_{12}}$. The two defects are considered in the actual approach as being magnetically equivalent; thus they have the same zero-field splitting, $D_0 = 2880$ MHz and $E = 0$. z, z', and z" are principal axis of the fine structure tensors associated with different spin multiplets. The general Hamiltonian of the system is

$$\hat{H} = \hat{H}_S + \hat{H}_0 + \hat{H}_{Zeeman} \tag{7.1}$$

where the spin Hamiltonian $\hat{H}_S$ describes the magnetic dipolar interaction between the four electrons of the two defect centers, $\hat{H}_0$ is the electrostatic interaction Hamiltonian, and $\hat{H}_{Zeeman}$ is the electron Zeeman Hamiltonian. The spin-orbit interaction is neglected for this case. The spin Hamiltonian is the sum between the dipolar magnetic contributions of the electrons and is given by

$$H_S = \frac{1}{2} g^2 \mu_B^2 \sum_{k,k'} \left(\frac{s_k s_{k'}}{r_{kk'}^3} - 3 \frac{(s_k r_{kk'})(s_{k'} r_{kk'})}{r_{kk'}^5} \right) \tag{7.2}$$

where g is the electron $g-$factor and μ_b is the Bohr magneton. The sum is done over all electrons. Therefore, the spin Hamiltonian will contain six terms: two terms describing the intramolecular interactions, i.e., dipolar interactions between the two electrons within a single defect center, and four intermolecular dipolar interactions, between individual electrons of the two defects. The total wavefunction of the system can be decomposed into an

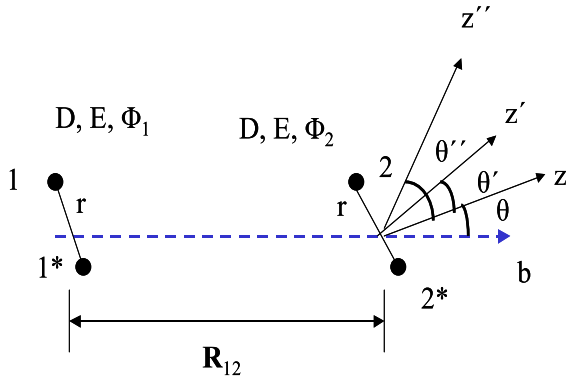

Figure 7.2: Geometrical model for two coupled NVs, according to the approach by Benk and Sixl. Each of triplet states is given by two coupled electrons and has the wavefunctions ϕ_1 and ϕ_2. The defects are considered magnetically equivalent, i.e., with the same individual zero-field parameters, D = 2880 MHz and E = 0. z, z', and z" are principal axes of the fine structure tensors of the individual defects, the pair triplet states and pair quintet states, respectively, making the angles θ, θ' and θ'' with the intermolecular axis.

orbital part and a spin part

$$|\psi\rangle = |\psi_{orbital}\rangle\,|\psi_{spin}\rangle \tag{7.3}$$

due to the fact that the spin orbit interaction is neglected and that the spin Hamiltonian commutes with the electrostatic Hamiltonian.

Calculations are performed assuming that the average intramolecular distances between the two electrons of one defect, r_{11} and r_{22} are equal and much lower than the distance between the two centers, R_{12}

$$\langle r_{11^*}\rangle = \langle r_{22^*}\rangle = \langle r\rangle\,, \tag{7.4}$$

$$\langle r_{12} \rangle = \langle r_{12^*} \rangle = \langle r_{21^*} \rangle = \langle r_{1^*2^*} \rangle = R_{12} >> \langle r \rangle \,. \tag{7.5}$$

Upon averaging the Hamiltonian over the orbital wave functions, a pure spin Hamiltonian is obtained

$$\begin{aligned} &\left\langle \hat{H} \right\rangle = \left\langle \psi_{orb} \left| \hat{H}_0 \right| \psi_{orb} \right\rangle = \left\langle \psi_{orb} \left| \hat{H}_0 \right| \psi_{orb} \right\rangle + \left\langle \psi_{orb} \left| \hat{H}_S \right| \psi_{orb} \right\rangle = \\ &= \varepsilon + \hat{H}_{spin} \end{aligned} \tag{7.6}$$

.

where ϵ is the electrostatic energy separating the spin multiplets. Due to the high separation between the defects in comparison to the intramolecular distance between the electrons, the overlap between the electron wavefunctions of different centers is very small, and therefore the exchange energy can be neglected. Finding the energy levels within the spin multiplets is reduced thus to diagonalizing the spin Hamiltonian. In the coordinate system depicted in the 7.2, the distance vector joining the two centers can be expressed as

$$\vec{R} = \begin{pmatrix} 0 \\ R\sin\varphi \\ -R\cos\varphi \end{pmatrix}. \tag{7.7}$$

The intermolecular dipolar term are therefore given by

$$\hat{H}_{12^*} = \hat{H}_{21^*} = \hat{H}_{12} = \hat{H}_{1^*2^*} = \frac{1}{2} g^2 \frac{\mu_B^2}{R^3} \begin{pmatrix} 1 & 0 & 0 \\ 0 & 1 - 3\sin^2\varphi & 3\sin\varphi\cos\varphi \\ 0 & 3\sin\varphi\cos\varphi & 1 - 3\cos^2\varphi \end{pmatrix}. \tag{7.8}$$

The total spin Hamiltonian is then given by

$$\begin{aligned}
&\hat{H}_{spin} = D_0\left(\hat{S}_{1z}^2 - \tfrac{1}{3}\hat{S}_1^2\right) + E_0\left(\hat{S}_{1x}^2 - \hat{S}_{1y}^2\right) + D_0\left(\hat{S}_{2z}^2 - \tfrac{1}{3}\hat{S}_2^2\right) + \\
&E_0\left(\hat{S}_{2x}^2 - \hat{S}_{2y}^2\right) + X\hat{S}_{1x}\hat{S}_{2x} + XA\hat{S}_{1y}\hat{S}_{2y} - X\left(1+A\right)\hat{S}_{1z}\hat{S}_{2z} \\
&+X\alpha\left(\hat{S}_{1z}\hat{S}_{2y} + \hat{S}_{1y}\hat{S}_{2z}\right)
\end{aligned} \tag{7.9}$$

where D_0 and E_0 are related to the individual fine structure tensors, the factors A and α describe the geometry of the system, and X the strength of the dipolar interaction between the centers

$$\begin{aligned}
A &= 1 - 3\sin^2\varphi \\
\alpha &= \sqrt{\left(1-A\right)\left(2+A\right)}
\end{aligned} \tag{7.10}$$

and

$$X = \frac{g^2\mu_B^2}{R}. \tag{7.11}$$

The spin coupling between the four electrons, $\mathbf{S} = \mathbf{S_1} + \mathbf{S_2}$, with $S_1 = S_2 = 1$ will result in three pure spin multiplets: a singlet (S), a triplet (T) and a quintet (Q), whose spin functions are given by linear combinations of individual triplet spin functions of the defects

$$|S_0\rangle = \sqrt{\frac{1}{3}}\left(|\tau_{1x}\tau_{2x}\rangle + |\tau_{1y}\tau_{2y}\rangle + |\tau_{1z}\tau_{2z}\rangle\right) \tag{7.12}$$

$$\begin{aligned}
|T_x\rangle &= \sqrt{1\!/_2}\left(|\tau_{1z}\tau_{2y}\rangle - |\tau_{1y}\tau_{2z}\rangle\right), \\
|T_y\rangle &= \sqrt{1\!/_2}\left(|\tau_{1x}\tau_{2z}\rangle - |\tau_{1z}\tau_{2x}\rangle\right), \\
|T_z\rangle &= \sqrt{1\!/_2}\left(|\tau_{1y}\tau_{2x}\rangle - |\tau_{1x}\tau_{2y}\rangle\right)
\end{aligned} \tag{7.13}$$

$$\begin{aligned}
|Q_{1z}\rangle &= \sqrt{1\!/_2}\left(|\tau_{1x}\tau_{2x}\rangle - |\tau_{1y}\tau_{2y}\rangle\right), \\
|Q_{2z}\rangle &= \sqrt{1\!/_2}\left(|\tau_{1x}\tau_{2y}\rangle + |\tau_{1y}\tau_{2x}\rangle\right), \\
|Q_x\rangle &= \sqrt{1\!/_2}\left(|\tau_{1y}\tau_{2z}\rangle - |\tau_{1z}\tau_{2y}\rangle\right), \\
|Q_y\rangle &= \sqrt{1\!/_2}\left(|\tau_{1x}\tau_{2z}\rangle + |\tau_{1z}\tau_{2x}\rangle\right), \\
|Q_{xy}\rangle &= \sqrt{1\!/_6}\left(|\tau_{1x}\tau_{2x}\rangle + |\tau_{1y}\tau_{2y}\rangle - 2\,|\tau_{1z}\tau_{2z}\rangle\right),
\end{aligned} \tag{7.14}$$

with τ_x, τ_y, and τ_z individual triplet spin functions [CM67]. The Hamiltonian can be diagonalized numerically or otherwise, analytical solutions can be found by using

$$\hat{S}_u \left|T_u\right\rangle = 0$$
$$\hat{S}_u \left|T_v\right\rangle = i \left|T_w\right\rangle \tag{7.15}$$

where $u, v, w = x, y, z$, analogue to the original triplet functions.

The present results are valid within the limit of large electrostatic energy, i.e., when the electrostatic energy separation $\Delta\epsilon$ between spin multiplets is much larger than the spin energy arising from the magnetic dipolar interaction. The resulting ESR transitions are identified subsequently within the pair states of different spin multiplicity only. The triplet and quintet energy levels are obtained by diagonalizing the Hamiltonian in the triplet eigenfunction and quintet eigenfunctions, respectively

$$E_{ij} = \left\langle T_i \left| \hat{H}_{spin} + \hat{H}_{Zeeman} \right| T_j \right\rangle \tag{7.16}$$

$$E_{ij} = \left\langle Q_i \left| \hat{H}_{spin} + \hat{H}_{Zeeman} \right| Q_j \right\rangle \tag{7.17}$$

with H_{Zeeman}, the Zeeman spin Hamiltonian. Considering the external magnetic field oriented along the fine structure axis of the triplet centers, the Zeeman term is

$$\hat{H}_{Zeeman} = g\mu_B B_o \hat{S}_z \tag{7.18}$$

Fig. 7.3 shows the obtained energy level scheme for the pair triplet state, in the absence of the magnetic field as well as in the presence of a small magnetic field, $B = 100$ G, oriented along the fine structure axis of the triplet centers. The levels in the figure are associated with high-field quantum numbers, i.e., m_S, where $S = S_1 + S_2$. It can be observed that the levels arrangement is inverted by the coupling of two defects. In the case of a single

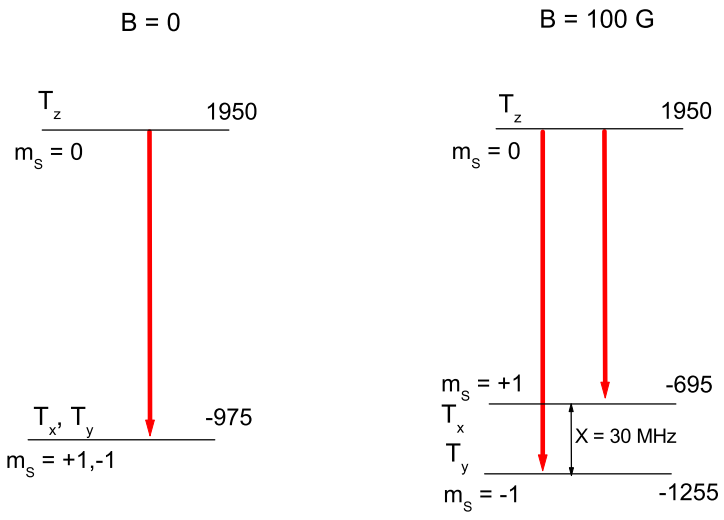

Figure 7.3: Energy levels of the pair triplet state of two coupled NVs. The levels energies are given in MHz, and states are identified by high-field quantum numbers. The coupling between the two centers inverts the order of the levels, i.e., τ_z is the higher energy state, as opposed to the individual spin triplets, where it was the lower state. For the fine structure parameter E = 0, symmetric centers, the lower energy level is degenerated. Upon applying a small external magnetic field, B = 100 G, the two lower levels split, resulting in two ESR allowed transitions.

defect center, the $m_S = 0$ level is the lowest energy level within the triplet, while in the case of the pair triplet state is the highest. In the absence of an external magnetic field, the main contributions to the level arrangement are given by the intermolecular dipolar interaction, X and the geometry of the system, provided that the fine structure parameter E is zero. Upon applying an external magnetic field along R, the T_z level remains unchanged, whereas T_x and T_y are Zeeman shifted. The ESR allowed transitions can be thus identified in the actual level scheme, based upon the $|\Delta m_S| = 1$ rule for the allowed transitions.

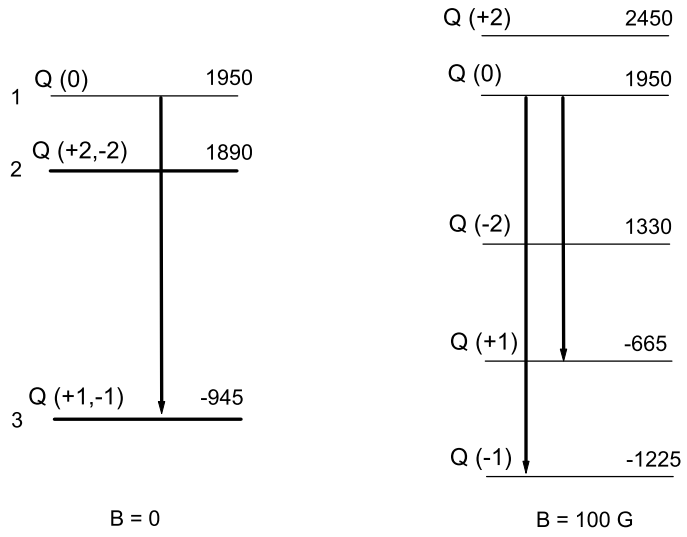

Figure 7.4: The energy levels for the pair quintet state in zero field and in a low field (100 G). The energy units are MHz. The allowed transitions are indicated by arrrows.

The quintet state energy level scheme is represented in Fig. 7.4, considering the same two situations for the external magnetic field. In the absence of the magnetic field, the quintet state presents an $m_S = 0$ level, and two degenerate levels corresponding to $m_S = \pm 1$ and $m_S = \pm 2$, respectively. In the presence of the magnetic field, the two degenerate levels, $Q(\pm 1)$ and $Q(\pm 2)$ are split into corresponding Zeeman levels. The resulting allowed transitions are shown in the figure. Transitions connecting $Q(\pm 2)$ with $Q(0)$ are not allowed in a first approximation due to the double spin flip processes.

The detailed Hamiltonian approach can offer a model for the cw spectrum in Fig. 7.1. In this approach the lines in the spectrum can be identified as transitions within the pair triplet and the pair quintet states. Each doublet in the actual representation consists of one ESR allowed transition within the

triplet and one ESR transition within the quintet, separated by the parameter X, the dipolar coupling between two centers. However, the model fails to provide a clear identification of energy levels in terms of individual centers, which would be beneficial for implementing quantum computing on this system. A simpler approach, perturbational, where the interaction between the centers is considered a perturbation in regard to the main Hamiltonian of two separate NVs can provide such a description.

7.2 Perturbational approach for two coupled defect centers

The previous section gave a detailed description of the magnetic dipolar interaction between two defect centers, where all the magnetic interactions were taken into account, i.e., both intermolecular and intramolecular. This approach gives a good description of the spectral lines present in experimental cw spectra, however it fails to identify the energy levels based on individual high field quantum numbers for individual defect centers. The levels in the previous approach were identified based on their m_S, corresponding to the sum between individual quantum numbers. A perturbational approach would provide a level identification based on pair of quantum numbers, (m_{S_1}, m_{S_2}), rather than the sum of them.

The perturbation theory can be applied in the present case, considering the amplitude of the magnetic dipolar interaction between two centers in comparison with the fine structure energy. Fig. 7.5 shows the dependency of the calculated magnetic dipolar interaction energy on the distance separating the two defects. The interaction energy corresponding to a distance r = 1 nm is around 15 MHz, much lower than the zero field splitting energy of the NV center, D = 2880 MHz.

Thus, the intermolecular interaction can be considered a pertubation to the fine structure energy of a system of two point dipoles. The resulting Hamiltonian reads

$$\hat{H}_{spin} = \hat{H}_0 + \hat{H}_1 \tag{7.19}$$

where

$$\hat{H}_0 = D_0 \left(\hat{S}_{1z}^2 - \frac{1}{3}\hat{S}_1^2 \right) + E_0 \left(\hat{S}_{1x}^2 - \hat{S}_{1y}^2 \right) + D_0 \left(\hat{S}_{2z}^2 - \frac{1}{3}\hat{S}_2^2 \right) + E_0 \left(\hat{S}_{2x}^2 - \hat{S}_{2y}^2 \right) \tag{7.20}$$

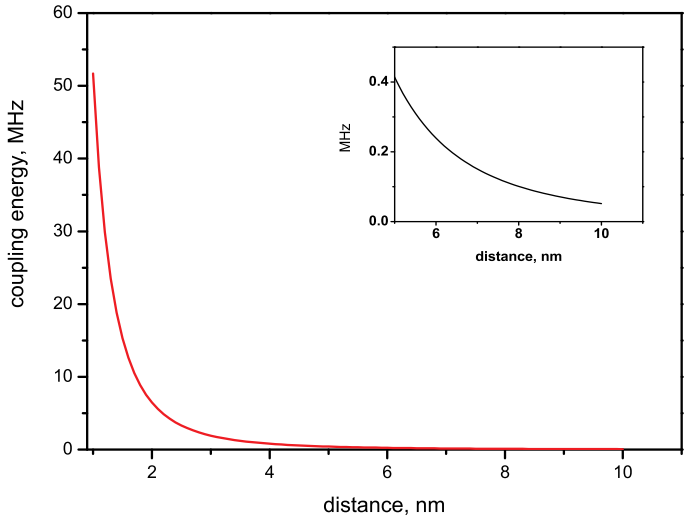

Figure 7.5: The separating distance dependency of the magnetic dipolar interaction energy between two centers. The calculation assumes two magnetically ecquivalent centers, with principal axis of the spin triplet tensors aligned. The inset to the figure shows a zoom for high separating distances. For a separating distance of $1 \div 2$ nm, the interaction energy is $5 \div 15$ MHz.

and

$$\hat{H}_1 = \hat{S}_1 \bar{T} \hat{S}_2 \tag{7.21}$$

with $\bar{T}$, the magnetic dipolar interaction tensor, whose elements are given by

$$T_{\alpha\beta} = \frac{1}{2}\frac{\mu_0}{4\pi} g^2 \mu_B^2 \left\langle \frac{r^2\delta_{\alpha\beta} - 3\alpha\beta}{r^5} \right\rangle . \tag{7.22}$$

Therefore, the energy matrix due to the perturbation is given by

$$E_1 = \left\langle \psi \left| \hat{H}_1 \right| \psi \right\rangle \tag{7.23}$$

where ψ is the spin functions basis in which the main Hamiltonian, i.e., zero-field and Zeeman, if existent, are diagonalized.

The transition probabilities have been calculated according to

$$P_{if} = \frac{2\pi}{\hbar^2} \left|\langle f \left| V \right| i \rangle\right|^2 \delta(\omega_{if} - \omega) \tag{7.24}$$

where V is the microwave perturbation which induces the ESR transitions

$$V = -\beta \vec{M} \cdot \vec{H}_1. \tag{7.25}$$

The calculations have been done for a distance between the two centers of 1.5 nm, with an external magnetic field of aprox. 60 G, oriented along the intermolecular axis. The resulting energy level scheme is shown in Fig. 7.6(b). The ground state is $|00\rangle$, while the next four energy levels are linear combinations of $|0-1\rangle$ and $|-10\rangle$ (levels 2 and 3) and $|01\rangle$ and $|10\rangle$ for levels 4 and 5, respectively. Table 7.1 shows the calculated coefficients corresponding to each eigenfunction in all the nine levels.

Table 7.1: The eigenfunctions corresponding to energy levels according to the perturbational approach. The eigenvectors are in the form $|m_{S_1} m_{S_2}\rangle$. The energy levels are denoted E_1 to E_9, with E_1 the lowest (see Fig. 7.6).

	E_1	E_2	E_3	E_4	E_5	E_6	E_7	E_8	E_9
$\|11\rangle$	0	0	0	0	0	0	0	0	1.00
$\|10\rangle$	0	0	0	0.707	-0.707	0	0	0	0
$\|1-1\rangle$	0	0	0	0	0	0	-0.707	0.707	0
$\|01\rangle$	0	0	0	0.707	-0.707	0	0	0	0
$\|00\rangle$	1.00	0	0	0	0	0	0	0	0
$\|0-1\rangle$	0	-0.707	0.707	0	0	0	0	0	0
$\|-11\rangle$	0	0	0	0	0	0	-0.707	0.707	0
$\|-10\rangle$	0	0.707	-0.707	0	0	0	0	0	0
$\|-1-1\rangle$	0	0	0	0	0	1.00	0	0	0

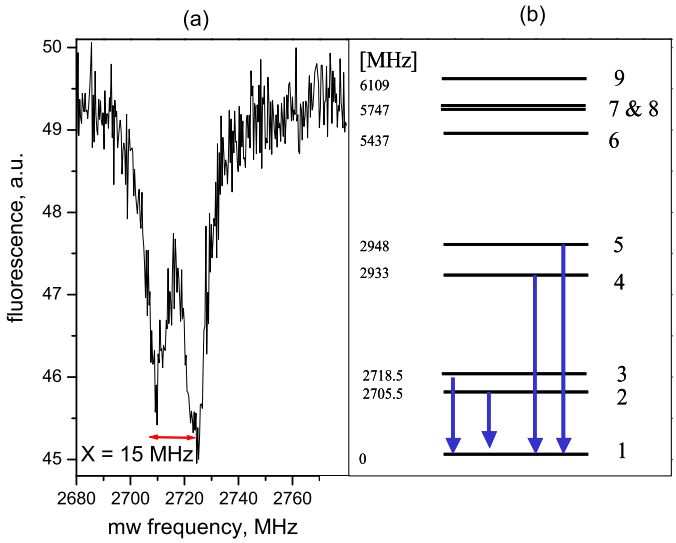

Figure 7.6: Calculated energy level scheme obtained within perturbational approach.

The allowed ESR transitions occur between each of the levels 2 to 5 and level 1. Levels 6 to 9 consist of linear combinations of $|1-1\rangle$ and $|-11\rangle$ (levels 7 and 8, degenerate) or $|-1-1\rangle$ (level 6) and $|11\rangle$ (level 9). Transitions originating from any of these levels to level 1 would involve double spin-flip processes. The experimental cw spectrum shown in Fig. 7.7(a) presents a set of two doublets. The energy separation within each of the two doublets is given by the inter-center magnetic dipolar interaction, and it is 15 MHz for this case (Fig.7.6(a)) . This is corresponding to the distance between the energy levels 2 and 3, and 4 and 5, respectively.

The stick plot in Fig. 7.7(b) shows the calculated transition probabilities, for the two doublets. Due to the identical coefficients of the eigenfunctions within each linear combination describing the levels 2 to 5, transition probabilities are equal. However, the calculations do not include the influence of

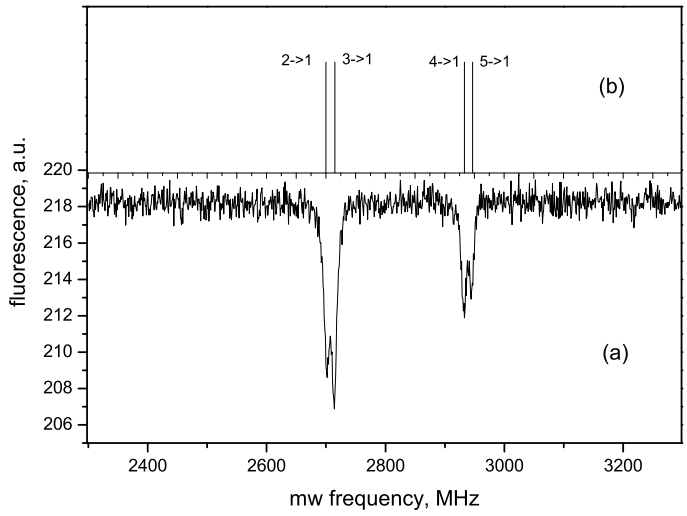

Figure 7.7: (a) cw spectrum of two coupled NVs showing two doublets (b) The calculated transition strengths. Optical readout influence was not taken into account.

the optical readout upon population distributions for each level, therefore, a deviation from experimental values of the transition strength is expected.

The perturbational approach in describing the coupling between two NVs offers a good model for explaining the cw spectrum in Fig.7.1. The lines in the spectrum can be positively identified within the energy levels scheme resulting from the model. Furthermore, the model allows to describe the levels in terms of individual centers, with eigenfunctions in the form $|m_{S_1} m_{S_2}\rangle$. This is beneficial for approaching quantum computing aspects.

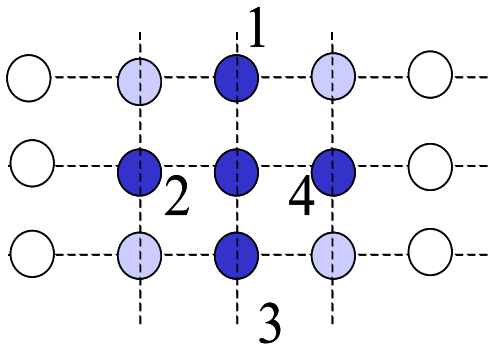

Figure 7.8: Geometrical representation of a sample pattern of implanted single NVs. The dipolar coupling to the closest neighbors, dark filled circles in the figure, will be the strongest; the interaction decreases as the separating distance between the centers increases.

7.3 Spin dynamics of two coupled NVs

The coupling between NV centers gives the opportunity of scaling up the number of spin qubits and implementing multiple qubit operations. Fig. 7.8 shows a rectangular pattern of implanted NVs. Thus, the central defect interacts strongly with the closest neighbours in the pattern, namely 1 to 4 in the figure. The interactions with the other defects decreases as the separating distance between the centers increases. However, for inter-center distances ranging from 5 nm up, the dipolar interaction is under 300 kHz, lower than the detectable linewidth.

After identifying the energy levels of the system in terms of quantum numbers associated with individual defects, the decoherence properties of two coupled NVs have to be analyzed. In order to determine the decoherence

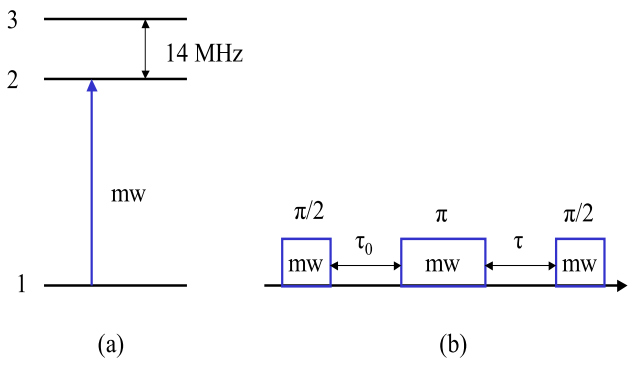

Figure 7.9: The Hahn echo pulse sequence applied to two coupled NVs. (a) The energy levels where the Hahn echo was applied. Levels 2 and 3 are separated by the dipolar interaction energy between two centers. The sequence was performed in the presence of a small magnetic field (B = 100 G). b) The pulses employed - the last $\pi/2$ mw pulse was used in order to facilitate the optical readout.

time of the system, a Hahn echo modulation pulse sequence similar to the one employed in the previous cases had been applied (7.9(a)). This will allow for the determination of the decoherence time of the system and the eventual influence of the coupling of the two centers on the decoherence. Fig. 7.9(a) shows the three energy levels, where the pulse sequence was performed. These are the first three levels in the perturbational approach energy levels scheme. The microwaves have been coupled to levels 1 and 2. The Rabi frequency of the microwaves (around 30 MHz), is higher than the dipolar coupling between the two centers, i.e., the splitting between levels 2 and 3, in the figure, which will result in a beating pattern of the Hahn echo amplitude.

Fig. 7.10 shows the experimental data of the Hahn echo decay. The echo

does not decay completely within the experimental time range considered. The decoherence time for a pair of coupled NVs is thus similar to that correspoding to a electron spin of a single NV center. The magnetic dipolar coupling of the two centers appears not to be a major source of decoherence for the electron spin. In the previous data, it was shown that in the case of an electron spin of the NV hyperfine coupled to a ^{13}C nucleus, the decoherence time of the electron spin was not affected significantly by the relatively strong hyperfine coupling (A = 130 MHz). In the case of two coupled centers the dipolar coupling is one order of magnitude lower and is expected to be a neglectible factor for the decoherence of the system. Furthermore, in the considered case, the levels 2 and 3 are linear combinations of $|0-1\rangle$ and $|-10\rangle$, with equal coefficients. Thus upon changing the value of the spin of one center, the total spin function of the system will remain unchanged, contributing to a long decoherence time.

A possible source of decoherence is the hyperfine coupling to the ^{14}N nucleus. The advantage of performing a Hahn echo modulation experiment over a simple Hahn echo is that the former unravells particularly small hyperfine couplings of the electron spin. Fig. 7.10 shows a pattern of fast and slow modulations of the Hahn echo decay. The Fourier transform of the echo in Fig. 7.11 shows several lines corresponding to the modulations of the echo, reflecting all the couplings of the electron spin. The line marked 'dipolar' in the figure is due to the beating between levels 2 and 3, coming directly from the magnetic dipolar coupling between the two centers. Additionally, it presents two satelite lines, corresponding to the substraction and addition, respectively of the hyperfine coupling (2.5 MHz for ^{14}N) from and to the dipolar line. The lowest frequency component comes from modulations within the hyperfine levels of ^{14}N (see inset to Fig.7.11).

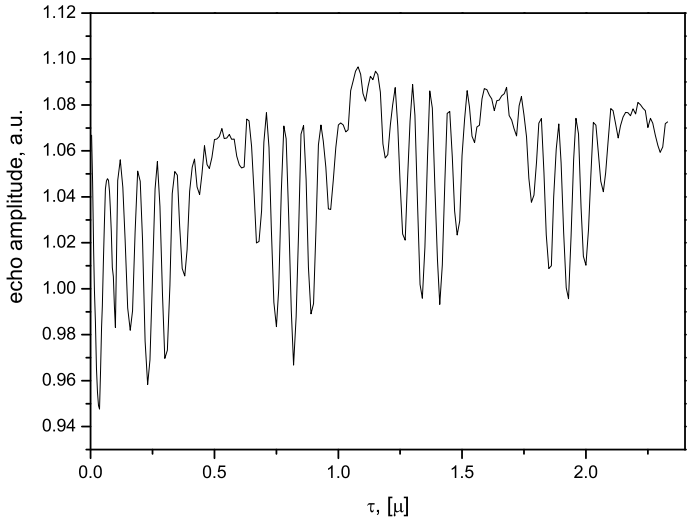

Figure 7.10: The Hahn echo amplitude as a function of the delay time, τ. From the exponential decay of the echo, a decoherence time of μseconds can be inferred.

The analysis shown in this chapter demonstrates that a system formed by two coupled NV centers is suitable for qubit implementations. The system presents a clear energy structure with a set of two doublets in a magnetic field. The coherence time for the system is similar to that of a single electron in a defect center, high enough for applying quantum gates. By creating patterns of NV centers in diamond the dipolar interaction can be extended to several centers. Furthermore, the system might be suitable for creating Bell states. As it can be observed in the pertubational approach, levels 2 and 3 are given by linear combinations of $|0-1\rangle$ and $|-10\rangle$, while 4 and 5 by $|01\rangle$ and $|10\rangle$. These states are irreducible to direct product individual states.

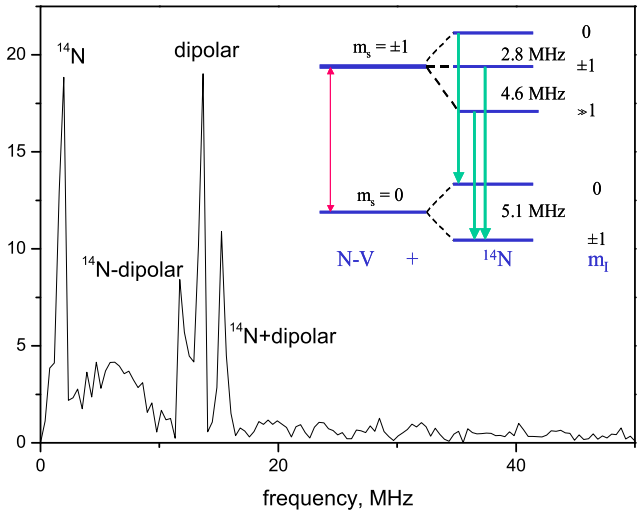

Figure 7.11: Fourier tranform of the Hahn echo modulation data. The line marked 'dipolar' is corresponding to the dipolar coupling between the two NVs. The satellite lines are are given by the beating in the Hahn echo to the addition and substraction of the hyperfine coupling to the ^{14}N nucleus. The lowest energy line is given by the modulations within the hyperfine coupling to nitrogen only. The inset to the figure shows a calculated energy levels of the hyperfine coupled electron spin to the ^{14}N nucleus

Summary

The primary purpose of this work was the study of single NV centers structure and dynamics for proving their use in quantum computing. The investigations combined the detection of single centers based on fluorescence emission with magnetic resonance methods. The state of single NV centers can be optically readout at room temperature using confocal microscopy. The energy structure of the triplet ground level was probed via cw ODMR. For a single NV defect in the absence of an external magnetic field, a zero field splitting of 2.88 GHz was found, in accordance with previous experimental work on ensembles. The coherent behaviour upon application of microwave pulses was probed initially by performing transient nutation experiments. The decoherence time in transient nutations experiments was found to vary significantly with the laser power. At high laser powers, the decoherence time decreases. The effect was related to the frequency of measurement. The suppression of Rabi oscillations upon increasing the frequency of measurement,i.e., the number of photons incident to the center, is a characteristic sign for the quantum Zeno effect. A linear dependency of the decoherence rate versus laser power was observed and confirmed by calculations. However, for higher laser powers in the saturation regime, the metastable state is increasingly populated, making the system unsuitable for testing the quantum Zeno effect. The decoherence time for electrons was found by applying a Hahn echo

sequence, adapted to optical readout.

The hyperfine coupling between the single electron spin and the ^{13}C nuclear spin ($I = \frac{1}{2}$) was investigated. The isotropic hyperfine constant is around 130 MHz for a ^{13}C nucleus located in the first coordination shell. Detection and coherent manipulation of the nuclear states were done via the electronic states. Rabi nutations for the nuclear spins have been recorded. In order to determine the dephasing time for the nuclear spins, a Hahn echo decay sequence was applied. This exhibits no decay in the echo amplitude for up to 30 μs. The result implies that the strong coupling of the single electron spin to the single ^{13}C nucleus does not result in a source of decoherence for the nuclear spins, and hence, these can be used as well for quantum computing.

The magnetic dipolar coupling between two defects was observed and analyzed. The cw ODMR spectrum of two coupled centers reveals an interaction energy of around 15 MHz, corresponding to a separation distance between the two centers of 1 nm. Two theoretical models have been applied to interpret the cw ODMR spectrum. The first takes into account all dipolar interactions between the four electron spins, i.e., inter- and intra-molecular dipolar interactions. The approach confirms experimental results. However, the level description is not in terms of individual spin functions, but in terms of total projection quantum numbers. For the later case, an approach based on perturbation theory gives the correct answer.

Zusammenfassung

Das Hauptziel dieser Arbeit war die Untersuchung einzelner NV-Zentren hinsichtlich ihrer Struktur und Dynamik, um ihren Einsatz auf dem Gebiet des Quantencomputing zu prüfen. Einer der gegenwärtig verwendeten Ansätze für das Quantencomputing beruht auf den Spins. Das Verhalten der Spins und ihre Eigenschaften bezüglich Manipulation und Auslesen der in Frage kommenden Systeme sind daher von großem Interesse. Nach der konventionellen NMR kann ein Ensemble von Spins als Qubit-Implementierung benutzt werden. Diese Methode hat jedoch Einschränkungen bezüglich der Anzahl an Qubits, die erzielt werden kann. Hauptsächlich liegt dies daran, dass mit großen Spinensembles gerabeitet werden muß. Konventionelle magnetische Resonanzmethoden können wegen ihrer geringen Empfindlichkeit nämlich nicht zur Detektion einzelner Spins verwendet werden. Stattdessen hat sich als Alternativmethode zur Detektion der magnetischen Resonanz die optische Detektion der magnetischen Resonanz (ODMR) zur Untersuchung einzelner Spins als geeignet erwiesen. Die Methode der Wahl, um einzelne NV-Defekte zu untersuchen, vereint Methoden der Einzelmoleküldetektion mit denen der magnetischen Resonanz. Ein Verfahren, welches auf einzelnen Spins beruhen würde, wäre eine gute Alternative zu den auf Spinensemble basierenden Implementierungen auf dem Gebiet des Quantencomputing. Auf diese Weise würde eine Mittelung durch das Ensemble eliminiert werden und

reine Zustände wären zugänglich. Eine gute Spin-Implementierung würde einen einzelnen Spin benötigen, welcher leicht manipuliert und ausgelesen werden kann. Das Stickstoff-Fehlstellen (NV) - Zentrum im Diamant besitzt gerade diese Merkmale. Das NV-Zentrum ist eine Störstelle im Diamant, die optisch auf der Einzelmolekülebene ausgelesen werden kann. Das Zentrum bleibt auch nach optischer Anregung photostabil. Aufgrund seiner paramagnetischen Natur, sind solche Zentren für ESR-Messungen zugänglich. Die logischen Gatter würden aus ESR-Pulsen bestehen. Um jedoch ein Qubit aus einem NV-Zentrum zu erhalten, müssen sowohl seine Eigenschaften als auch sein dynamisches Verhalten vollständig verstanden werden.

Die Stickstoff-Fehlstelle besteht aus einem einzigen Stickstoffatom, welches direkt neben einer angrenzenden Fehlstelle im Gitter liegt. Zusätzlich fängt das Zentrum ein Elektron aus dem Diamantgitter ein. Der Elektronenspin der Fehlstelle entsteht durch die Kopplung zwischen dem eingefangenen Elektron und dem ungepaarten Elektron des Stickstoffatoms, was einen Spin von S = 1 ergibt. Das NV-Zentrum ist somit eine paramagnetische Störstelle. Diese Störstelle kann im natürlichen Diamant mit Stickstoff - Verunreinigungen auftreten, wobei eine besonders hohe Konzentration im Typ Ia Diamant zu finden ist. Im Fall von Typ Ib Diamanten können NV-Defektzentren durch Bestrahlung und nachfolgendem Tempern bei Temperaturen über 800 K erhalten werden. Durch Bestrahlung mit Elektronen werden Leerstellen im Diamantgitter erzeugt. Durch das Aufheizen wandern die Fehlstellen durch das Diamantgitter und können auf die vorhandenen Stickstoffatome treffen. Dadurch steigt die Wahrscheinlichkeit an, dass man höhere Konzentrationen an NV-Defektzentren erhält. Durch N^+-Implantation können NV-Defektzentren auch in Typ IIa Diamanten erzeugt werden. Basierend auf Versuchen mit Neutronenstrahlen konnte gezeigt wer-

den, dass die NV-Defektzentren negativ geladen sind.

Das Energieniveauschema besteht aus einem Triplettgrundzustand, einem angeregten Triplettzustand und aus einem metastabilen Singulettzustand. Das Zentrum kann aufgrund des fluoreszierenden Übergangs zwischen dem angeregten Triplettzustand und dem Triplettgrundzustand optisch detektiert werden. Im magnetischen Nullfeld spaltet sich der Grundzustand in drei Bestandteile auf: X und Y ($m_s = \pm 1$) und Z ($m_s = 0$), die sich um 2,88 GHz unterscheiden. Der Grundzustand kann als Spin-Qubit-Implementierung verwendet werden.

Die Aufspaltung zwischen den Niveaus X und Y ist für eine Fehlstelle mit axialer Symmetrie null. In diesem Fall besteht der Grundzustand aus zwei Niveaus, welche für die Realisierung eines Qubits geeignet sind.

Eine Detektion von einzelnen Fehlstellen konnte mit Fluoreszenzanregungsspektroskopie durch ein konfokales Mikroskop erreicht werden. Der Spinzustand des Zentrums wurde optisch ausgelesen, so dass die magnetische Resonanzhardware ausschließlich zur Manipulation der Spins gebraucht wurde. Für ESR-Experimente wurden Mikrowellen über einen Mikroresonator (bereitgestellt von D.Suter, Universität Dortmund) auf die Probe übertragen. Der sehr kleine Durchmesser des Resonators ermöglicht Rabifrequenzen von bis zu 50 MHz im Zentrum der Schleife.

Der allgemeine Spin-Hamilton-Operator, der die NV-Fehlstellen beschreibt, lautet:

$$\begin{aligned} H &= H_{ZF} + H_{eZeeman} + H_{hf} + H_Q + H_{nZeeman} \\ &= \hat{S}\bar{D}\hat{S} + \beta_e \vec{B}_0 \bar{g} \hat{S} + \sum_{i=1}^{N} \hat{S}\bar{A}_k\hat{I}_k + \sum_{I_k>1} \hat{I}_k\bar{P}_k\hat{I}_k - \beta_N \sum_{k=1}^{N} g_{n,k}\vec{B}_0\hat{I}_k \end{aligned} \tag{7.26}$$

in dem g_e und g_n die g-Faktoren für das Elektron beziehungsweise für den Kern sind, β_e das Bohrsche Magneton, β_n das Kernmagneton, A der Hyperfeinkopplungstensor, P der Quadrupolkopplungstensor und B_0 das externe

Magnetfeld. Die Energieniveauverteilung kann durch Diagonalisierung des Hamilton-Operators erhalten werden. Daraus können dann die Eigenwerte und die Eigenfunktionen numerisch mit Hilfe jeder linearen Algebra-Software berechnet werden (Matlab, NAG).

Um die Spindynamiken des Zentrums zu beschreiben, müssen die Bevölkerungszahlen der Niveaus berechnet werden. Die emittierte Fluoreszenz ist durch den Unterschied in den Besetzungen der Niveaus gegeben. Die Zeitentwicklung der Dichtematrix ist durch die Liouville Gleichung gegeben.

$$i\hbar\frac{d\rho}{dt} = [H, \rho] \tag{7.27}$$

Für die Berechnungen wurde ein 5-Niveau-Modell mit einem axial symmetrischen NV Zentrum angenommen. Abbildung 3.1 zeigt ein NV-Niveauschema, welches man durch die Berechnungen erhalten hat. Der Anregungslaser koppelt das $m_s = 0$ Subniveau des Grundzustands mit einem vibronischen Niveau des angeregten Zustands ^{3}E. Die strahlungsfreie Relaxation der vibronischen Niveaus befindet sich in der Größenordnung von 10^{15} Hz. Die Mikrowellen werden zwischen den Subniveaus des Grundzustands eingestrahlt, die durch die Nullfeld-Aufspaltung aufgetrennt sind. In der Annahme, dass ein NV-Zentrum einem optischen und magnetischen Feld unterliegt, kann das NV-Zentrum durch folgenden Hamilton-Operator beschrieben werden:

$$\begin{aligned} H = &\sum_i \hbar\omega_i \left|i\right\rangle \left\langle i\right| - \hbar\Omega\cos\left(\omega_M t\right)\left(\left|1\right\rangle\left\langle 2\right| + \left|2\right\rangle\left\langle 1\right|\right) - \\ &\hbar\Lambda\cos\left(\omega_L t\right)\left(\left|1\right\rangle\left\langle 4\right| + \left|4\right\rangle\left\langle 1\right|\right) \end{aligned} \tag{7.28}$$

in welchem ω_i die Energie des Zustandes i ist, ω_L die Laserfrequenz, ω_M die Mikrowellenfrequenz, Ω die Laser Rabifrequenz und Λ die Mikrowellen-Rabifrequenz. Die Dichtematrix kann numerisch aus der Liouville Gleichung berechnet werden.

Innerhalb des Triplett-Grundniveaus ist ein ESR-erlaubter Übergang für ein symmetrisches Zentrum vorhanden (zwei Übergänge für den Fall $E \neq 0$), wobei dieser bei 2,88 GHz liegt. Dies kann mittels cw (continuus wave)-ODMR an einem einzelnen Zentrum nachgewiesen werden. Die cw-ODMR Experimente wurden mittels Durchstimmen der Mikrowellen entlang eines bestimmten Frequenzbereichs durchgeführt. Der Mittelpunkt des Frequenzbereichs lag dabei im Aufspaltungsbereich der Niveaus Z und X oder Y. Das System ist hauptsächlich im Niveau Z polarisiert. Durch das optische Auslesen wird dieses Niveau mit dem entsprechenden Unterniveau im angeregten Zustand ^{3}E gekoppelt. Für diesen Zweck wurde ein grüner Laser (532nm) verwendet. Die gemessene Fluoreszenz behält ein konstantes Niveau bei solange sich die Bevölkerungsverteilung innerhalb des Triplett-Grundzustands nicht verändert. Wenn die eingestrahlten Mikrowellen in Resonanz mit den erlaubten ESR-Übergängen sind, ändert sich die Bevölkerungsverteilung. Das System wird eine Veränderung der Bevölkerung vom Niveau Z zu den Niveaus X oder Y hin erfahren. Als Ergebnis wird eine geringere Fluoreszenzemission resultieren, da das optische Auslesen hauptsächlich mit dem Z-Niveau gekoppelt ist. Abbildung 5.2 zeigt ein experimentelles cw-ODMR Spektrum von einem einzelnen NV-Zentrum. Dem Zentrum fehlt die charakteristische C_{3v} Symmetrie und zeigt deshalb zwei zulässige Übergänge. Die Aufspaltung zwischen den zwei Linien beträgt in diesem Fall 10 MHz (E = 10 MHz, im Nullfeldtensor). Das Spektrum wurde bei Raumtemperatur in Abwesenheit eines externen Magnetfeldes aufgenommen. Der ODMR Linienkontrast beträgt ungefähr 20% des Fluoreszenzsignals.

Eine der Bedingungen, die ein Qubit zu erfüllen hat, ist eine lange Dekohärenzzeit. Innerhalb dieser Dekohärenzzeit können Quantengatter Anwendung finden. Die erste experimentelle Untersuchung zum kohärenten Verhalten

einzelner Elektronenspins war ein transientes Nutationsexperiment. Für den Fall des NV-Zentrums können Nutationen durch Anlegen eines Mikrowellenfeldes mit einer Frequenz entsprechend der Aufspaltung innerhalb des Triplett-Grundzustandes erzeugt werden. Nach Anlegen des Mikrowellenfeldes wird davon ausgegangen, dass das System zwischen den zwei Niveaus (E = 0) in Phase oszilliert.

Für einzelne NV-Zentren wurden transiente Nutationen unter kontinuierlicher Laserbestrahlung (537 nm) durch Beobachtung der Fluoreszenzintensität während eines Mikrowellenpulses aufgenommen. Abbildung 5.8 zeigt das Ergebnis eines transienten Nutationsversuchs an einem einzelnen NV-Zentrum. Die eingesetzte Laserleistung betrug 300 μW. Die Nutationskurve zeigt einen Zerfall der Nutationen in einem Bereich von 1 μs. Die Nutationszerfallszeit allein liefert jedoch nicht die Dekohärenzzeit für das System. Sogar im Fall einzelner Systeme tritt während der Messung eine inhomogene Linienverbreiterung auf. Um die Dekohärenzzeit zu erhalten, muss deshalb ein Hahn-Echo Experiment durchgeführt werden. Es wurde beobachtet, dass die Nutationszerfallszeit für größere Laserleistungen kleiner ist als bei niedrigeren Laserleistungen. Abbildung 5.10 zeigt die gemessene Abhängigkeit der Dekohärenzrate von der Laserleistung und die berechneten Dekohärenzraten, die mit dem 5-Niveaumodell berechnet wurden. Eine Unterdrückung der Rabi-Oszillationen in den transienten Nutationsexperimenten hängt mit dem Zenoeffekt zusammen. Der Zenoeffekt besagt, dass eine fortlaufende Messung an einem Quantensystem dessen Zustandsentwicklung hemmt. Für den Fall des NV-Zentrums wird eine Messung durch Fluoreszenzphotonen ermöglicht. Eine erhöhte Laserleistung entspricht deshalb einer höheren Messfrequenz. Dadurch wird der Übergang aus dem Grundzustand in den angeregten Zustand verhindert, was eine kleinere Dekohärenzzeit

zur Folge hat und die Unterdrückung der Rabi-Oszillationen bedeutet. Für höhere Laserleistungen im Sättigungsbereich folgt die Nutationszerfallszeit aufgrund des metastabilen Singulettzustands einer Sättigungskurve. Die Wahrscheinlichkeit der Besetzung des metastabilen Singulettniveaus steigt mit der Laserleistung. Im gegenwärtigen Modell wurde die Feinstruktur des angeregten Triplett nicht berücksichtigt. Folglich dürfte das System bei hohen Laserleistungen keine extakte Prüfmethode für den Zenoeffekt sein.

Aufgrund der Inhomogenitäten, die das System besitzt, kann mittels transienter Nutationsversuche die Spin-Dephasierungszeit nicht ermittelt werden. Durch ESEEM (Electron-Spin-Echo-Envelope-Modulation)-Experimente kann sowohl die Dekohärenzzeit eines Spins als auch die Hyperfein-Kopplung zu benachbarten Kernen untersucht werden. Die eingesetzte Pulssequenz, die entsprechend dem optischen Auslesen verändert wurde, besteht aus einem $\pi/2$-Puls, um die Kohärenz anzuregen, und einem π-Puls zur anschließenden Refokusierung. Ein weiterer $\pi/2$-Puls ist notwendig, um die Kohärenzen in unterscheidbare Bevölkerungszustände umzuwandeln. Die Zeitintervalle zwischen den einzelnen Mikrowellenpulsen sind entweder konstant oder variabel. Abbildung 5.16 zeigt ein ESEEM-Spektrum eines einzelnen NV-Zentrums in Anwesenheit eines schwachen Magnetfeldes (30 G). Aus dem exponentiellen Zerfall des Echos konnte eine Dekohärenzzeit von 0,3 μs ermittelt werden. Die Zerfallskurve wird aufgrund der Hyperfein-Kopplung zum ^{14}N-Atom noch mit einer Modulation überlagert. Aufgrund der Tatsache, dass die Rabifrequenz der Mikrowellen (ca. 30 MHz) größer als die Hyperfein-Kopplung zu ^{14}N-Atomen (2,3 MHz) ist, werden mehrere ESR-Übergänge angeregt. Ihre Wechselwirkung liefert die Modulation im Hahn-Echo-Zerfall. Dies wurde durch eine Fourier-Transformation des Hahn-Echo-Zerfalls in Abbildung 5.17 gezeigt. Das magnetische Feld spaltet die Niveaus X und Y auf,

so dass es keine Interaktion zwischen den beiden erlaubten ESR-Übergängen gibt. Diese beiden erlaubten ESR-Übergänge entsprechen gerade denen zu den Niveaus X und Y. Die berechnete Hyperfein-Struktur ist in Abbildung 5.7 gezeigt; folgende Parameter wurde verwendet: $A_\perp$ = 2,3 MHz, $A_\parallel$ = 2,1 MHz und für die Quadrupol-Kopplungskonstante P wurde ein Wert von -5,01 MHz eingesetzt. Die Linien der Fourier-Transformation konnten im berechneten Modell identifiziert werden.

Eine andere wichtige Bedingung für ein Qubit ist die Skalierbarkeit. Um Quanten-Algorithmen durchführen zu können, werden mehrere Qubits benötigt. Eine erste Möglichkeit ist durch die Hyperfein-Kopplung zum ^{13}C-Kern gegeben. ^{13}C-Atome treten mit einer natürlichen Häufigkeit von 1,07% auf und besitzen einen Kernspin von I = 1/2, dies führt zu einer Hyperfein-Aufspaltung der Elektronenniveaus des NV-Zentrums. Basierend auf dem natürlichen Vorkommen von ^{13}C-Atomen erfährt eines von 30 NV-Zentren eine Hyperfein-Kopplung mit dem nächsten ^{13}C-Kern. Die Hyperfein-Kopplungskonstante beträgt für die erste Koordinationsschale 130 MHz und geht für die zweite Koordinationsschale auf 70 MHz zurück. Für einen ^{13}C-Kern, der sich in der dritten Koordinationsschale befindet, wird eine Hyperfein-Kopplung von ungefähr 10 MHz geschätzt. Der Spin des ^{13}C-Kerns kann nicht auf direktem Weg optisch ausgelesen werden. Die Kernzustände werden über die Elektronenzustände des NV-Zentrums ausgelesen, und die Hyperfeinstruktur kann experimentell über cw-ODMR Experimente ermittelt werden. Abbildung 6.1 zeigt ein cw-Spektrum für einen einzelnen Elektronenspin eines NV-Zentrums, der mit einem einzigen ^{13}C-Kern in einem externen Magnetfeld von 10 G durch Hyperfeinwechselwirkung gekoppelt ist. Das Spektrum zeigt vier Linien, die den erlaubten ESR-Übergängen entsprechen. Diese Linien werden durch das berechnete Energieniveauschema bestätigt. Für höhere Magnet-

felder jedoch verdoppelt sich die Anzahl an Übergängen, weil eine zusätzliche Aufspaltung des untersten Niveaus aufgrund des pseudo-nuklearen Zeeman-Effekts auftritt. Das Magnetfeld induziert eine Wechselwirkung zwischen $m_s = 0$ und $m_s = -1$, was zu viel größeren Werten der nuklearen Zeeman-Aufspaltung führt. Das entsprechende Energieniveauschema ist in Abbildung 6.6 gezeigt.

Um Informationen über die Dekohärenzzeit einzelner Kernspins zu erhalten, wurde eine Hahn-Echo-Sequenz angelegt. Die Sequenz wurde entsprechend der Detektion einzelner Kernspins ausgewählt. Die Kernspins können nicht direkt mit dem aktuellen Versuchsaufbau untersucht werden, da nur Elektronenzustände optisch ausgelesen werden können. Deshalb wird der Elektronenspin dazu gebraucht, zwischen der Detektion und der Manipulation einzelner Kernspin-Zustände zu vermitteln. Abbildung 6.13 zeigt eine Serie von Hahn-Echos, die für verschiedene Werte von τ_1 aufgenommen wurden. Für ein Zeitintervall von bis zu 30 μs zeigt die relative Amplitude der Echos einzelner Kernspins keinen Zerfall. Verglichen mit dem Wert, den man bei Messungen im Ensemble von ^{13}C-Kernen erhält (100 μs), kann gesagt werden, dass die Hyperfein-Kopplung zum Elektronenspin des NV-Zentrums nicht zu einer zusätzlichen Dekohärenzquelle einzelner Kernspins beiträgt.

Ein wesentlicher Anstieg der Anzahl an Qubits kann durch magnetische Dipolkopplung mehrerer NV-Zentren erreicht werden. Ein Vorteil dieser Herangehensweise gegenüber der Einbeziehung benachbarter Kerne, ist dadurch gegeben, dass eine Vielzahl von Defektzentren innerhalb des Kopplungsbereichs magnetischer Dipole miteinander wechselwirken können. Die Interaktion zwischen den NV-Zentren ist durch eine Nanopositionierung kontrollierbar. Das Energieniveauschema zweier koppelnder NV-Zentren wurde mit zwei verschiedenen Ansätzen berechnet: einem detaillierten Hamilton-Ansatz

und einer Störungstheorie. Der erste Ansatz berücksichtigt alle möglichen Wechselwirkungen zwischen den vier Elektronen, die zu der Kopplung zwischen zwei Zentren führen. In der Störungstheorie wird die dipolare Wechselwirkung zwischen den Zentren als Störung des Hamilton-Operators der getrennten NV-Zentren betrachtet. Diese Aussage ist dadurch gerechtfertigt, dass beispielsweise für einen Abstand der Zentren von 1,5 nm, die dipolare Wechselwirkungsenergie ca. 15 MHz beträgt. Im Vergleich zu den Nullfeld-Energien einzelner NV-Zentren, deren dipolare Wechselwirkungsenergie bei 2,9 GHz liegt, ist der Wert für die dipolare Wechselwirkungsenergie mit 15 MHz sehr viel kleiner. Die Experimente an zwei gekoppelten NV-Zentren wurden an demselben Aufbau durchgeführt, der bereits in dieser Arbeit beschrieben wurde. Das cw-ODMR Spektrum ist in Abbildung 7.1 gezeigt. Das Spektrum wurde in einem Magnetfeld mit einer Stärke von ca. 70 G aufgenommen und besteht aus zwei Dubletts, die entsprechend der Zeeman-Energie der zwei NV-Zentren aufgespalten sind. Die Aufspaltungsenergien zwischen den zwei Linien innerhalb eines jeden Dubletts sind gleich.

Der präzise Hamilton-Ansatz stellt eine gute Möglichkeit dar, die spektralen Linien in den experimentell aufgenommenen cw-Spektren zu berechnen. Mit diesem Ansatz können jedoch nicht die Energieniveaus identifiziert werden, die auf individuellen Hochfeld-Qantenzahlen einzelner Defektzentren beruhen. Die Niveaus in diesem Ansatz wurden mittels ihrer (m_S, m_S) bestimmt, was der Summe der individuellen Quantenzahlen entspricht. Mit Hilfe der Störungstheorie würden die Energieniveaus in der Art und Weise ermittelt werden, dass ein Paar an Quantenzahlen (m_{S_1}, m_{S_2}) in Betracht gezogen wird und nicht die Summe dieses Paares. Die zwischenmolekulare Wechselwirkung kann als Störung der Feinstrukturenergie eines Systems aus zwei Punktdipolen gesehen werden. Der resultierende Hamilton-Operator

lautet wie folgt:

$$\hat{H}_{spin} = \hat{H}_0 + \hat{H}_1 \tag{7.29}$$

wobei

$$\hat{H}_0 = D_0 \left(\hat{S}_{1z}^2 - \frac{1}{3}\hat{S}_1^2 \right) + E_0 \left(\hat{S}_{1x}^2 - \hat{S}_{1y}^2 \right) + D_0 \left(\hat{S}_{2z}^2 - \frac{1}{3}\hat{S}_2^2 \right) + E_0 \left(\hat{S}_{2x}^2 - \hat{S}_{2y}^2 \right) \tag{7.30}$$

und

$$\hat{H}_1 = \hat{S}\bar{T}\hat{S} \tag{7.31}$$

mit $\bar{T}$

$$T_{\alpha\beta} = \frac{1}{2}\frac{\mu_0}{4\pi} g^2 \mu_B^2 \left\langle \frac{r^2\delta_{\alpha\beta} - 3\alpha\beta}{r^5} \right\rangle . \tag{7.32}$$

Die Berechnungen wurden für einen Abstand von 1,5 nm zwischen den Zentren und einem externen Magnetfeld von ca. 60 G, welches entlang der intermolekularen Achse orientiert war, durchgeführt. Das dadurch erhaltene Energieniveauschema ist in Abbildung 7.6 gezeigt. Mit der Störungstheorie kann die Kopplung zwischen zwei NV-Zentren beschrieben werden. Anhand dieses Modells, kann das cw-Spektrum in Abbildung 7.7 erklärt werden. Die Linien in diesem Spektrum können eindeutig im Energieniveauschema, welches mit Hilfe der Störungstheorie berechnet wurde, identifiziert werden. Desweiteren erlaubt dieses Modell die Niveaus hinsichtlich der Eigenfunktionen individueller Zentren zu beschreiben. Dies ist vorteilhaft zur Behandlung von Fragestellungen auf dem Gebiet des Quantencomputing.

Nach der Identifizierung der Energieniveaus des Systems hinsichtlich der Quantenzahlen der einzelnen Defekte, wurden die Dekohärenzeigenschaften von zwei koppelnden NV-Zentren näher untersucht. Um die Dekohärenzzeit des Systems zu bestimmen, wurde eine Hahn-Echo Modulations-Pulssequenz, ähnlich der in vorherigen Experimenten eingesetzten, verwendet. Dadurch können die Dekohärenzzeit des Systems und schließlich der Einfluss der Kop-

plung der zwei Zentren auf die Dekohärenz bestimmt werden. Abbildung 7.9(a) zeigt die drei Energieniveaus, die man aus dem Pulssequenzexperiment erhalten hat. Diese Energieniveaus entsprechen den ersten drei Niveaus des Energieniveauschemas, das mit der Störungstheorie berechnet wurde. Die Mikrowellen koppelten mit den Niveaus 1 und 2. Die Rabifrequenz der Mikrowellen (ungefähr 30 MHz) ist größer als die dipolare Kopplung zwischen den zwei Zentren. Das zeigt die Aufspaltung zwischen den Niveaus 2 und 3 in der Abbildung 7.9(a). Diese Aufspaltung führt zu einer Modulation der Hahn-Echo Amplitude. Abbildung 7.10 zeigt die Messdaten des Hahn-Echo-Zerfalls. Das Echo zerfällt nicht vollständig in dem betrachteten Zeitbereich. Die Dekohärenzzeit für ein Paar koppelnder NV-Zentren ist daher ähnlich zu der entsprechenden Dekohärenzzeit eines Elektronenspins eines einzelnen NV-Zentrums. Die magnetische Dipolkopplung der zwei Zentren scheint nicht die Hauptquelle für die Dekohärenz eines Elektronenspins zu sein. Das Modulationsmuster im Echo entsteht durch die Wechselwirkung zwischen den ESR-Übergängen und der Auswirkung der Hyperfein-Kopplung zum ^{14}N-Atom.

Die Auswertung zeigt, dass ein System aus zwei koppelnden NV-Zentren für eine Qubit-Implementierung geeignet ist. Das System zeigt in einem Magnetfeld eine klare Energiestruktur mit einer Gruppe von zwei Dubletts. Die Kohärenzzeit des Systems ist ähnlich zu der Zeit, die für ein einzelnes Elektron in einem Defekt-Zentrum ermittelt werden kann. Sie ist groß genug, um Quantengatter wirksam einzusetzen.

Bibliography

[AB70] A. Abragam and B. Bleaney. *Electron paramagnetic resonance of transition ions*. Oxford:Clarendon Press, 1970.

[BBG+01] Alexios Beveratos, Rosa Brouri, Thierry Gacoin, Jean-Philippe Poizat, and Philippe Grangier. *Phys. Rev A*, 64:061802, 2001.

[Ble67] B. Bleaney. *Hyperfine Interactions*. Academic Press, New York, 1967.

[BQG86] G. Binnig, C. F. Quate, and C. Gerber. Atomic force microscope. *Phys. Rev. Lett.*, 56:930, 1986.

[BR87] G. Binnig and H. Rohrer. Scanning tunneling microscopy - from birth to adolescence. *Rev. Mod. Phys.*, 59:615, 1987.

[BS81] H. Benk and H. Sixl. Theory of two coupled triplet states. application to bicarbene structures. *Molecular Physics*, 42:779, 1981.

[BW99] M. Born and E. Wolf. *Priciples of Optics*. Campbridge University Press, Cambridge, 1999.

[BWO+94] R. Brown, J. Wrachtrup, M. Orrit, J. Bernard, and C. von Borczyskowski. *J. Chem Phys.*, 100:7182, 1994.

[CDKW88] A. T. Collins, G. Davies, H. Kanda, and G. S. Woods. *J. Phys. C: Solid State Phys.*, 21:1363, 1988.

[CM67] Alan Carrington and Andrew D. McLachlan. *Introduction to magnetic resonance*. Harper International, 1967.

[Coo88] R. J. Cook. *Phys. Scr.*, T21:49, 1988.

[CTJ83] A. T. Collins, M. F. Tomasz, and M. I. B. Jorge. *J. Phys. C: Solid State Phys.*, 16:2177, 1983.

[CZ95] J. I. Cirac and P. Zoller. Quantum computations with cold trapped ions. *Phys. Rev. Lett.*, 74:4091, 1995.

[Dav84] Gordon Davies. *Diamond*. Hilger, Bristol, 1984.

[Dav94] G. Davies. *Properties and growth of diamond*. INSPEC, London, 1994.

[DFT+99] A. Dräbenstedt, L. Fleury, C. Tietz, F. Jelezko, S. Kilin, A. Nizovtzev, and J. Wrachtrup. *Phys. Rev. B*, 60:11503, 1999.

[DH76] G. Davies and M. F. Hamer. *Proc. R. Soc. A*, 384:285, 1976.

[DiV95] D. P. DiVincenzo. Quantum computation. *Science*, 270:255, 1995.

[DLC+92] G. Davies, S. C. Lawson, A. T. Collins, A. Mainwood, and S. L. Sharp. *Phys. Rev. B*, 46:13157, 1992.

[ea93a] J. Köhler et al. Magnetic resonance of a single molecular spin. *Nature*, 363:242, 1993.

[ea93b] J. Wrachtrup et al. Optical detection of magnetic resonance in a single molecule. *Nature*, 363:244, 1993.

[EKM01] R. Laflamme E. Knill and G. J. Milburn. *Nature*, 46:409, 2001.

[Fre88] Ray Freeman. *A handbook of nuclear magnetic resonance*. Harlow:Longman, 1988.

[GC97] N. A. Gershenfeld and I. L. Chuang. *Science*, 275:350, 1997.

[GC98] N. A. Gershenfeld and I. L. Chuang. *Sci. Am.*, 278:66, 1998.

[GDT+97] A. Gruber, A. Dräbenstedt, C. Tietz, L. Fleury, J. Wrachtrup, and C. von Borczyskowski. *Science*, 276:2012, 1997.

[Gro95] J. Grover. In *Proc. 28th Annual ACM Symposium on the Theory of Computation*, page 212, New York, 1995. ACM Press.

[HMF93] Xing-Fei He, Neil B. Manson, and Peter T. H. Fisk. *Phys. Rev. B*, 47:8816, 1993.

[IBW87] W. M. Itano, J. C. Bergquist, and D. J. Wineland. Laser spectroscopy of trapped atomic ions. *Science*, 237:612, 1987.

[IHBW90] W. M. Itano, D. J. Heinzen, J.J. Bollinger, and D.J. Wineland. Quantum zeno effect. *Phys. Rev. A*, 41:2295, 1990.

[JF72] Charles P. Poole Jr. and Horacio A. Farach. *The Theory of Magnetic Resonance*. Wiley-Interscience, 1972.

[KAO+00] B. Kozankiewicz, M. Aloshyna, M. Orrit, Ph. Tamarat, A.D. Gudmundsdottir, and M.S. Platz. *J. Phys. Chem A*, 104:7464, 2000.

[KMZW00] C. Kurtsiefer, S. Mayer, P. Zarda, and H. Weinfurter. *Phys. Rev. Lett.*, 85:290, 2000.

[LL01] M.N. Leuenberger and D. Loss. *Physica E*, 10:452, 2001.

[LLH04] M. Luszczek, R. Laskowski, and P. Horodecki. *Physica B*, 348:292, 2004.

[Lou83] R. Loudon. *The quantum theory of light*. Oxford University Press, Oxford, 1983.

[LvW77] J.H.N. Loubser and J.A. van Wyk. *Diamond Res.*, 11, 1977.

[Mar99] J. P. D. Martin. *J. Lumin.*, 81:237, 1999.

[Mim72] W. B. Mims. *Phys. Rev. B*, 5:2409, 1972.

[Mit96] Y. Mita. *Phys. Rev. B*, 53:11360, 1996.

[MK89] W. E. Moerner and L. Kador. Optical detection and spectroscopy of single molecules in a solid. *Phys. Rev. Lett.*, 62:2535, 1989.

[MOL+99] J.E. Mooij, T.P. Orlando, L. Levitov, L. Tian, C. H. van der Wal, and S. Lloyd. Josephson persistent-current qubit. *Science*, 285:1036, 1999.

[MS77] B. Misra and E. C. G. Sudarshan. The zeno's paradox in quantum theory. *J. Math. Phys.*, 18:756, 1977.

[NKJ+03] A.P. Nizovtsev, S. Ya. Kilin, F. Jelezko, I. Popa, A. Gruber, C. Tietz, and J. Wrachtrup. *Optics and Spectroscopy*, 94:910, 2003.

[NPT99] Y. Nakamura, Yu.A. Pashkin, and J.S. Tsai. Coherent control of macroscopic quantum states in a single-cooper-pair box. *Nature*, 398:786, 1999.

[OB90] M. Orrit and J. Bernard. Single pentacene molecules detected by fluorescence excitation in a p-terphenyl crystal. *Phys. Rev. Lett.*, 65:2716, 1990.

[Orr02] M. Orrit. Single-molecule spectroscopy: The road ahead. *J. Chem. Phys.*, 117:10938, 2002.

[PW01] P. Palinginis and H. Wang. *Applied Physics Letters*, 78:1541, 2001.

[Ran94] S. C. Rand. *Properties and Growth of Diamond*. INSPEC, London, 1994.

[RMK87] N. R. S. Reddy, N. B. Manson, and E. R. Krausz. *J. Lumin.*, 38:46, 1987.

[SA80] A. Suisalu and R. Avarmaa. Level anticrossing and pseudonuclear zeeman effect in the triplet state of kcl:po_2^-. *Phys. Stat. Sol. (b)*, 97:69, 1980.

[Sho94] P. W. Shor. In Shafi Goldwasser, editor, *Proceedings of the 35th Annual Symposium on Foundations of Computer Science*, page 1484. IEEE Computer Society Press, 1994.

[SJ01] Arthur Schweiger and Gunnar Jaschke. *Priciples of pulse electron resonance*. Oxford University Press, Oxford, 2001.

[SSSA94] K. Schaumburg, E. Shabanova, J.P.F. Sellschop, and T. Anthony. Longitudinal and rotating frame spin-lattice relaxation in ^{13}c-enriched diamonds. *Solid State Commun.*, 91:735, 1994.

[vO90] E. van Oort. PhD thesis, Amsterdam, 1990.

[VSB+01] L.M.K. Vandersypen, M. Steffen, G. Breyta, C.S. Yannoni, M.H. Sherwood, and I.L. Chuang. *Nature*, 414:883, 2001.

[WBW94] John A. Weil, James R. Bolton, and John E. Wertz. *Electron Paramagnetic Resonance: Elementary Theory and Practical Applications*. Wiley-Interscience, 1994.

[WC97] N. Gershenfeld W.S.Warren; and I. Chuang. *Science*, 277:1688, 1997.

[WKN01] J. Wrachtrup, S. Ya. Kilin, and A.P. Nizovtsev. Quantum computation using the ^{13}c nuclear spins near the single nv defect center in diamond. *Optics and Spectroscopy*, 91:429, 2001.

[Zai01] A. Zaitsev. *Optical Properties of Diamond - a Data Handbook*. Springer, Berlin, 2001.

Acknowledgments

The author would like to thank the many people who have helped with this project during the past three years. This project would not have been possible without their support.

I would first like to thank my adviser, Prof. Jörg Wrachtrup, who gave me the opportunity to complete my PhD studies in his research group, and who provided continuous assistance and support during this time and helped me make some sense of the confusion. I would like to thank as well to Prof. Gert Denninger for co-supervising the dissertation. Special thanks go to Dr. Fedor Jelezko for the valuable support with the experimental part of this work and for his patience in answering questions time and again. Prof. S. Kilin and Dr. A. Nizovtsev are kindly aknowledged for their support and advice on the theory side with developing the simulation models. Many thanks as well to Torsten Gaebel, for helping with the experimental part and for providing valuable comments at several points during writing this dissertation.

This work benefited also from several other people involved in single defect centers research. My thanks go to Achim Gruber as well as Michael Domhan and Cristopher Wittman. Thanks to the Graduate College for the financial means to complete this project. Special thanks to Alexandra Elli,

who contributed her time and effort to complete the German version of the dissertation outline and to Andrew Aird and Sebastian Schuler, for their support at various stages of completing this dissertation.